Electronic and structural properties of LaNiO3-based heterostructures

Fowlie, Jennifer

UNIVERSITÉ DE GENÈVE
Department of Quantum
Matter Physics

FACULTÉ DES SCIENCES
Professeur J.-M. Triscone

Electronic and structural properties of $LaNiO_3$-based heterostructures

THÈSE

présentée à la Faculté des Sciences de l'Université de Genève
pour obtenir le grade de docteur ès Sciences, mention Physique

par

Jennifer FOWLIE
de
New Deer (Écosse)

Thèse n° 3241

GENÈVE
Nom de l'imprimerie
2018

UNIVERSITÉ
DE GENÈVE
FACULTÉ DES SCIENCES

DOCTORAT ÈS SCIENCES, MENTION PHYSIQUE

Thèse de Madame Jennifer FOWLIE

intitulée :

«Electronic and Structural Properties of $LaNiO_3$-based Heterostructures»

La Faculté des sciences, sur le préavis de Monsieur J.-M. TRISCONE, professeur ordinaire et directeur de thèse (Département de physique de la matière quantique), Monsieur A. GEORGES, professeur (Département de physique de la matière quantique), Monsieur C. AHN, professeur (Yale University, New Haven, Connecticut, U.S.A.), Monsieur P. WILLMOTT (Institut de Physique Expérimentale, Université de Zürich et Paul Scherrer Institut, Villigen, Suisse), professeur, autorise l'impression de la présente thèse, sans exprimer d'opinion sur les propositions qui y sont énoncées.

Genève, le 30 juillet 2018

Thèse - 3241 -

Le Doyen

N.B. - La thèse doit porter la déclaration précédente et remplir les conditions énumérées dans les "Informations relatives aux thèses de doctorat à l'Université de Genève".

Dedicated to Sandy Caldwell.

Résumé

La physique des oxydes de métaux de transition est contrôlée par les orbitales d du métal de transition. La nature de ces orbitales est telle que plusieurs degrés de liberté – charge, orbital, spin et réseau – coexistent à des énergies très similaires. Cette proximité en énergie engendre une interaction entre plusieurs phases électroniques en compétition les unes avec les autres. L'implémentation d'oxydes de métaux de transition dans des hétérostructures permet de manipuler ces phases corrélées grâce aux effets de contrainte et à divers autres effets dus aux interfaces. La famille des perovskites de nickelates avec la formule chimique $R\mathrm{NiO}_3$, une série de composés connus pour leur transition métal-isolant marquée et contrôlable, est le sujet de nombreuses études. Le LaNiO_3, en particulier, est un métal corrélé typique qui a un vaste potentiel d'applications. Afin d'étudier l'effet de la combinaison de ce type de matériaux en hétérostructures, des couches minces de LaNiO_3, ont été réalisées par pulvérisation cathodique et caractérisées en grands détails. Une des méthodes de caractérisation utilisée dans cette étude, la mesure de pics de Bragg demi-entiers déterminés par diffraction aux rayons-x a révélé la nature et l'amplitude des distorsions de la structure atomique de ce matériau. Une étude basée sur cette technique a mis en lumière l'importance des discontinuités aux interfaces dans la détermination de la structure de ces couches minces. Cependant, lorsque l'épaisseur de LaNiO_3 est réduite à une valeur proche de la limite atomique, le matériau extrêmement fin entre dans un état électronique isolant qui n'est pas encore bien compris. Une étude sondant cette dépendance en épaisseur révèle une augmentation de la conductivité pour une gamme réduite d'épaisseurs. L'étude détaillée de la structure de ces couches minces démontre que cette augmentation de conductivité est due à une compétition entre plusieurs structures locales présentes à différentes « profondeurs » dans les couches de LaNiO_3. Le comportement électronique fascinant du LaNiO_3 à très faibles épaisseurs peut potentiellement avoir d'importantes implications pour la réalisation d'hétérostuctures basées sur des couches minces d'une épaisseur de une seule cellule unité de LaNiO_3 qui ont été proposées théoriquement comme pouvant potentiellement révéler un état fondamental supraconducteur. La dernière partie de cette étude décrit le concept de supraconductivité utilisant le concept de « negative U » - l'idée que deux électrons ont tendance à se

« grouper » sur un site - et comment ce concept pourrait amener à l'existence de supraconducteurs basés sur les nickelates. Dans le but d'étudier cette possibilité, la solution solide de $Nd_{1-x}La_xNiO_3$ a été caractérisée afin de déterminer la composition pour laquelle ce matériau pourrait développer un état isolant – disproportionné – un état pour lequel le $NdNiO_3$ est bien connu – à une température de 0 K.

Contents

Chapter 1

Summary

One of the biggest dreams in the physics of electronic materials is to be able to engineer any property by design; a goal that is being approached from the side of theory and from the side of experiment. Historically, the two approaches have been fairly independent but, with continuing technological development on both sides, there may eventually be a convergence. More advanced growth and characterisation of samples in the laboratory is matched by more sophisticated calculations and, as a result, feedback times between theory and experiment are ever-shortening. Optimistically, a future where the workflow goes from *request a property* $\rightarrow$ *design a material to give that property* $\rightarrow$ *fabricate the material to meet the specifications* is possible. In the domain of metallurgy, for instance, offering a specific set of material properties as a deliverable is nothing new.

The transition metal oxides make up a family of materials that offers a huge range of engineerable properties, perhaps none so famous as high temperature superconductivity. The underlying mechanism for high temperature superconductivity has, so far, been difficult to pin down. This makes it challenging to know how to tune the critical temperature higher or engineer other properties to coexist with the superconducting state. The best efforts so far have been made by studying similar or analogous compounds and empirical observation.

The search for a synthetic superconductor serves as one of the motivations in this work, which focusses on heterostructures of $LaNiO_3$. Particular attention is paid to highlighting the challenges associated with working on complex oxide heterostructures and the ramifications these can have for future tailor-made oxides.

This thesis begins, in **Chapter 2**, by introducing transition metal oxide perovskites through describing their structure and properties and by establishing the intimate link between the two. It then goes on to a discussion of the field of thin film physics, in particular the challenges associated with such research. The final section of **Chapter 3** brings together the key points of the previous

chapter on perovskite oxides and the ideas of thin film physics just introduced to describe the fascinating area of research that is thin film perovskite oxides. **Chapter 4** brings to the forefront a particular family of these materials; the rare earth nickelates, $R\mathrm{NiO}_3$. First, the physics of nickelates is summarised and the phase diagram is introduced with a discussion on the various transitions therein; metal-insulator, Néel and structural. Secondly, some physics specific to LaNiO_3 is discussed; namely the possibility of magnetic ordering and the idea of engineering superconductivity into nickelate-based heterostructures. **Chapter 5** contains descriptions of all the experimental techniques carried out as part of this thesis work. One of the techniques in particular warrants a chapter of its own so **Chapter 6** is dedicated to the study of oxygen octahedral distortions in perovskites by x-ray diffraction and is rounded up by the results of this analysis on two different oxide heterostructure systems. **Chapter 7** begins with a curious trend seen in electronic transport on ultrathin films of LaNiO_3 and the rest of the chapter is devoted to unveiling the origin. Then, the challenges in heterostructuring in a predictable way are discussed in the context of property-by-design materials science. The penultimate chapter, **Chapter 8** introduces the concept of valence skipping elements and negative U insulators and the possible implications for designing a nickelate-based superconductor in a novel way. To this end, the solid solution system $\mathrm{Nd}_{1-x}\mathrm{La}_x\mathrm{NiO}_3$ is characterised and the results are shown in the second part of that chapter. The thesis is brought to a close by **Chapter 9** where the work discussed in the preceding chapters is summarised and some conclusions drawn. The final word will be perspectives and some outlook for potentially exciting future projects.

Chapter 2

Introduction to Perovskite Oxides

2.1 Structure

Perovskite, with the chemical formula $CaTiO_3$, was discovered in 1839 in the Urals. It has a structure consisting of a cage of six oxygen anions surrounding the titanium cation in an octahedron. In the spaces between the octahedra, the calcium cations are found. There are many other compounds that share the same basic structure, sometimes referred to as "perovskite-like" to distinguish from the mineral itself but usually just called "perovskites" [1]. Generalising from $CaTiO_3$, the calcium can be replaced by almost any alkali metal, alkali earth metal or rare earth lanthanoid and this atomic site is denoted the A-site. The titanium, on the B-site, can be exchanged for some post-transition metals but usually it has its place taken by another transition metal, making up the transition metal oxide (TMO) perovskite series [2]. The A-cation primarily determines the valence of the B-cation and plays a structural role while the B-cation itself typically defines the physics.

The perovskite structure can be simplified to a network of corner-sharing oxygen octahedra, where a single octahedron constitutes the *pseudocubic* unit cell. The use of the pseudocubic unit cell is for convenience only as it is seldom the primitive unit cell, not even for the original perovskite mineral itself: Due to the mismatch between the ionic radii of the A- and B-site cations, the oxygen octahedra are, in almost all cases distorted, leading to a reduced symmetry and, therefore, larger primitive unit cell. This symmetry-lowering distortion is sometimes related to the position of the cations, as in ferroelectric compounds, and sometimes to a distortion of the octahedral shape itself, for instance a Jahn-Teller distortion or a breathing mode distortion. More often in the perovskite oxides, however, the distortion takes the form of octahedral tilts or rotations,

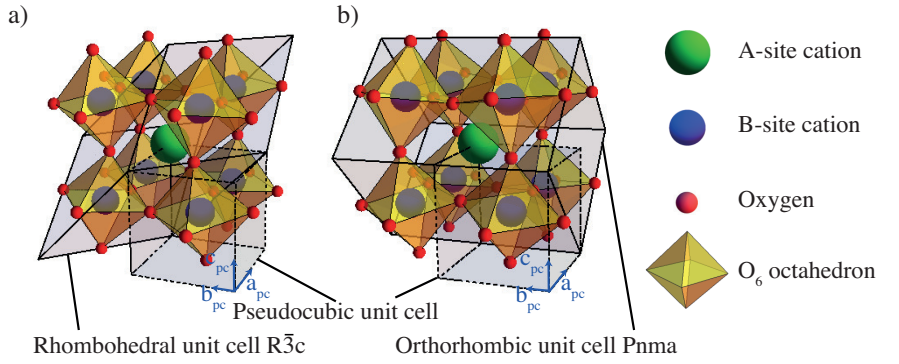

Figure 2.1: Two common structures of the perovskite oxides highlighting the fact that they can be visualised as a network of corner-sharing oxygen octahedra. In a) the rhombohedral unit cell and b) the orthorhombic unit cell.

which can be described by a shorthand notation introduced by A. M. Glazer in 1975 [3].

Fig. 2.1 shows two of the most common ABO_3 perovskite structures, their primitive unit cells as well as their pseudocubic (pc) unit cells.

Glazer notation consists of three labels that describe how the octahedra rotate along each of the three crystallographic axes. Each label consists of a letter and a superscript symbol. The letter can be a, b or c, corresponding to the crystallographic direction in question but if the rotations are equal in magnitude around more than one axis then the letter is repeated for the other labels starting alphabetically. The magnitude itself is represented by the greek letter α, β or γ for rotations around the a, b and c axes respectively. The superscript attached to each letter refers to the manner in which the octahedra rotate. If all the octahedra along the given axis rotate in the same direction then they are said to be *in phase* and the superscript is a $+$. In the other scenario, where an octahedron will rotate in the opposite direction to the ones either side of it along the given axis, the distortion is called *out of phase* and this is denoted by a superscript -. For consistency, even if there are no distortions at all, the superscript is set to 0 and the full Glazer notation is therefore $a^0a^0a^0$ where, of course, $\alpha = \beta = \gamma = 0^o$. Fig. 2.2 attempts to clarify Glazer notation pictorially. In panel d), for instance, is the common orthorhombic structure $Pbnm$ (a $Pnma$ unit cell rotated by 90 °). Here, there is an out-of-phase rotation around the c-axis, which ends up being the long axis in the orthorhombic unit cell, and out-of-phase rotations of equivalent magnitude around the a and b axes. This gives a Glazer notation of $a^-a^-c^+$.

As schematised in Fig. 2.2b)-d), it is possible to move between certain perovskite structures smoothly by slowly *turning on* the octahedral rotations. This is not the case for all combinations of structures, however, and Fig. 2.3 sum-

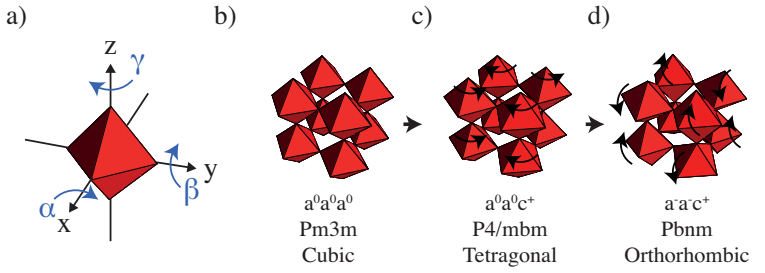

Figure 2.2: a) Diagram to show how the Glazer rotations of magnitude α, β and γ relate to the crystallographic axes of the octahedron. Then an example of how the gradual onset of octahedral rotations can lead from a cubic structure (panel b)) to a tetragonal one (panel c)) to an orthorhombic one (panel d)). For each step the associated Glazer notation and space group are provided.

marises all the possible space groups belonging to the perovskites that undergo pure octahedral rotations as well as the subgroup relations between them.

The basic perovskite structure is demonstrably flexible, being able to adapt to the different combinations of A- and B-site cations through numerous types of distortions. Simply by changing one, or both, of the cations, a whole range of structures can be accessed with varying symmetries and lattice parameters, in other words, the lattice has a large degree of freedom. As we will now see, this is not the only degree of freedom in the perovskite TMOs and the richness of the crystal structure is reflected, and even multiplied, in the physical properties [5].

2.2 Properties

Predicting the properties of a material can be done from a quantum mechanical approach by analysing the energy scales of the various microscopic interactions. If most of the interactions can be neglected due to their relative weakness, the Hamiltonian of the system can be written with very few terms, making calculation of the total energy rather straightforward. In this case, the material properties are simple to determine by looking for the electronic configuration that minimises the total energy. Transition metals and their oxides are not so readily understood, however. They very often have several active degrees of freedom and a correspondingly rich energy landscape. The fundamental reason for this lies in the feature that defines the transition metal block; d-orbital physics, some key attributes of which will now be described.

Transition metals make up a block of elements consisting of ten groups and four rows of the periodic table, those to the left are described as “early” and those to the right are described as “late”, and are defined as having their va-

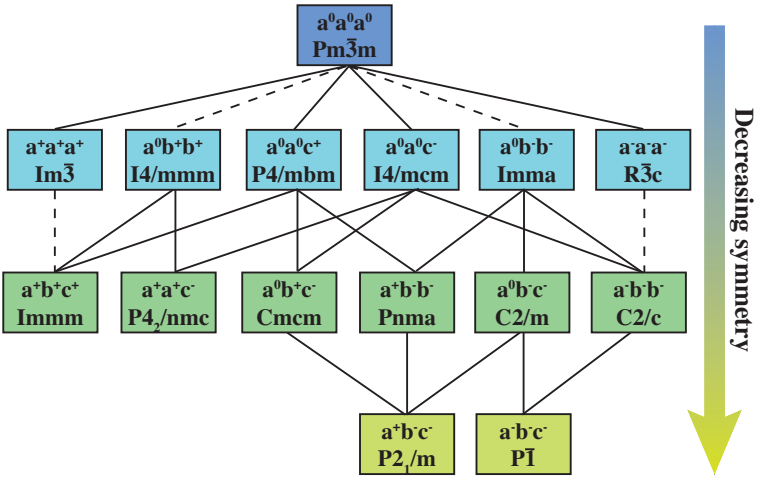

Figure 2.3: All the possible space groups, along with the corresponding Glazer description, arising from pure rotations of oxygen octahedra within the perovskite structure. The solid lines indicate a smooth, second order-like transition between the two space groups whereas the dashed lines signify a requirement that the phase transition is first order. Where there are no adjoining lines means that the two symmetries have no group-subgroup relation and no direct transition is allowed. Adapted from Ref. [4]

lence electrons in the d-shell [2]. The d-orbitals can host up to ten electrons between the five suborbitals, as illustrated in Fig. 2.4, which are degenerate in free space. Upon the introduction of a transition metal into a solid, the interaction with the surrounding lattice produces a crystal field that breaks the d-orbital degeneracy. Inside the O_6 cage of a perovskite, for instance, the orbitals split into three of lower energy that are directed between oxygen anions (t_{2g}) and two of higher energy that point towards the oxygens (e_g). The crystal field splitting energy is denoted $10Dq$, the notation of which comes from the quantum mechanical treatment of the electrostatics of crystal fields, see Fig. 2.4.

The d-orbitals are particularly flexible when it comes to the valence state. While alkali metals with their s-orbitals have only one or two oxidation ions, transition metals can often be oxidised into four, five, six, or even more, unique states. Furthermore, the energies of transition metal valences are typically close to the energy of the oxygen charge state. The transfer of electrons between the transition metal and oxygen is, therefore, energetically feasible and so is the transfer of electrons between different transition metal ions via the oxygen. The charge degree of freedom is thus rather accessible in TMOs but even when the valences are fixed, usually by the valence of the A-cation, there

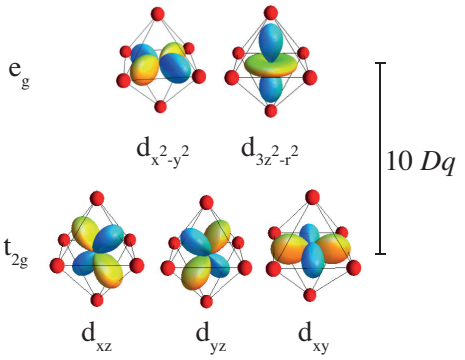

Figure 2.4: The shape of the d-orbitals relative to the O_6 perovskite cage grouped according to the reduced symmetry caused by the crystal field (t_{2g} and e_g). The colours correspond to the two signs of the wavefunction.

remain the spin and orbital degrees of freedom.

The degeneracy-breaking brought about by the solid state environment means that the t_{2g} states will usually be filled preferentially over the e_g ones, as established by the aufbau principle. The ion should also follow Hund's rule of maximum multiplicity; that all states should be filled with electrons of the same spin before being spin paired. This could potentially lead to occupation of the higher energy e_g states before the lower energy t_{2g} states are full, if the crystal field splitting is not too high. We now see one of the first interesting features of the TMOs: The crystal field splitting energy, $10Dq$, is often around the same magnitude as the Hund exchange energy, J. This means that the spin configuration is often very sensitive to external parameters such as pressure, representing a coupling between the spin and lattice degrees of freedom, for instance in $LaCoO_3$ [6].

Sometimes, the orbital degree of freedom plays an important role in the physics of transition metal oxides through the requirement of Hund's rule of maximising the orbital angular momentum [7]. This can induce a preferential occupation of a subset of the d-orbitals, leading to a situation described as "orbital ordering". With the ordering often comes an anisotropy in the macroscopic behaviour, for example, in electronic transport. Orbital ordering can prompt a structural distortion, usually Jahn-Teller-like, to occur concomitantly, indicating an orbital-lattice coupling [8].

As already shown in Fig. 2.4, the d-orbitals are highly directional and, in an octahedral crystal field, point either towards (e_g) or between (t_{2g}) the oxygens. The oxygens themselves have orbitals, however, that hybridise with the transition metal. This ligand hybridisation between the transition metal d-orbitals and oxygen p-orbitals is covalent in nature and occurs more strongly

between the e_g-p than between t_{2g}-p due to the geometry of the relevant nodes (sketched in Fig. 2.5a)). This overlap is directly related to the bandwidth, W and can be modified by structural distortions such as those described in Section 2.1 or, in thin films, by heterostructuring (see the following chapter). In fact, the bandwidth is roughly proportional to $cos^2(\theta)$ where θ is the bond angle between the B-cations through the oxygen (see Fig. 2.5b) and c)), a parameter of great importance for the nickelate family [9, 10].

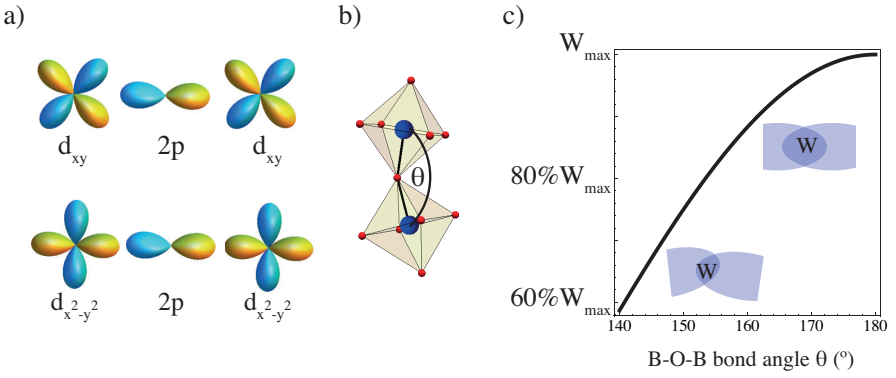

Figure 2.5: a) Comparison of the hybridisation configurations between the transition metal d and oxygen 2p states when the t_{2g} manifold is valent (top) and when the e_g manifold is valent (bottom). b) Schematic of the B-O-B bond angle θ and c) how the bond angle changes the bandwidth, W, by varying the orbital overlap through structural distortions.

By their very nature, the wavefunctions for the d-orbitals are rather spatially confined, so the electrons within are highly localised. This means that the energy required to force two electrons to occupy the same site is much higher for transition metals than for most other elements of the periodic table. Those two electrons repel each other due to the Coulomb interaction by the on-site repulsion energy, the Hubbard U. The fact that electron-electron interactions are non-negligible in many TMOs leads them to be classed as "correlated" materials. The study of electronic correlations and the effect of U on the physical properties has been extensive with much of this effort focussed on TMOs. The "simplest" Hamiltonian to describe a single band correlated material is the Hubbard Hamiltonian:

$$\mathcal{H} = -t \sum_{(i,j),\sigma} c^{\dagger}_{i,\sigma} c_{j,\sigma} + U \sum_{i} n_{i,\uparrow} n_{i,\downarrow} \tag{2.1}$$

where the first term represents the hopping of an electron from a site j to a site i, in other words the kinetic energy of the system, and the second term

describes the onsite Coulomb repulsion, U. When the ratio $\frac{U}{t}$ is increased, the original single band is split into two separate bands, denoted the upper Hubbard (UH) band and the lower Hubbard (LH) band. If the system has exactly one electron per site then the LH band is completely filled while the UH band is totally empty. This prevents any transfer of electrons and results in an insulator that would not be predicted by conventional band theory. The description of *Mott-Hubbard* insulators was the first of several successes of the Hubbard model and, since then, it has been extended to explain the properties of many oxides of early transition metals, such as Cr_2O_3 and $LaTiO_3$ [11].

Towards the late transition metals, however, the physics is not dominated only by d-d excitations (both inter and intra-atomic) but the ligand oxygen begins to play a role due to the alignment of the 2p lobes with the e_g orbitals in space as well as in energy, as shown in Fig. 2.5a). For oxides of late transition metals, then, the Hubbard model is often found to be insufficient and a model that takes into account the ligand oxygen was proposed instead [12]. Within this model, there can be an electron transferred from the oxygen p- to the transition metal d-shell, opening a gap termed the *charge transfer gap* and denoted Δ. Many insulating materials, such as CuO, can be understood within this picture, rendering them *charge transfer insulators* where the relevant insulating gap is not the Mott gap itself but rather the energy between the p-band of oxygen and the UH band.

There remain, however, some insulating ground states that still cannot be explained in the context of either Mott or charge transfer physics. Some high valence TMOs are, in fact, calculated to have a *negative* charge transfer energy, -Δ, despite their measured insulating properties. This was eventually explained by considering that the strong hybridisation between the transition metal d- and oxygen p- states can open a gap of purely p character between states that have two holes on the oxygen and states that have none [13]. This will be discussed further in Section 4 when we delve into the family of oxides of nickel, a late transition metal.

Fig. 2.6 shows the energy diagrams for the purely d-character Mott-Hubbard insulator, the mixed p-d-character charge transfer insulator and the purely p-character negative charge transfer insulator.

We have seen here that the orbital, charge, spin and lattice degrees of freedom of correlated transition metal oxides have associated energy scales (usually on the order of eV) that are very close to one another, leading to an inter-competition and strong coupling between them. This complex interplay gives rise to a plethora of fascinating phenomena such as metal-insulator transitions, exotic magnetism, orbital ordering, ferroelectricity, colossal magnetoresistance and high temperature superconductivity. Many compounds can exhibit several of these phenomena depending upon the external conditions, giving them a rich phase diagram. The scope of applications of TMOs is correspondingly wide-ranging. From bolometers, resistive switches and “smart windows” to water-splitters, batteries and memristors; the potential for commercial use is

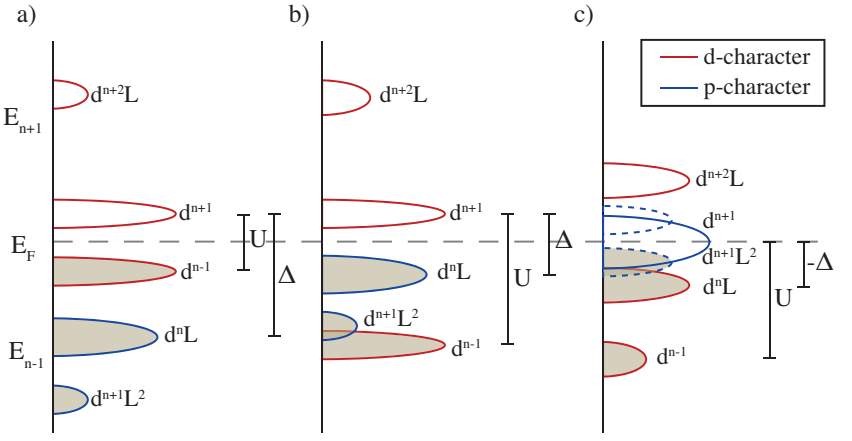

Figure 2.6: Energy diagrams of a) a Mott-Hubbard insulator, b) a charge transfer insulator and c) a negative charge transfer insulator. In each, the red and blue lines represent the d-character and p-character densities of states respectively and the onsite Coulomb repulsion, U and charge transfer energy Δ are marked. Adapted from [13]

great. All this could be possible with further study of TMOs and their available degrees of freedom.

An interesting approach to studying TMOs is by taking the lattice degree of freedom as a control knob to manipulate the other degrees of freedom. Tuning the lattice can be done by chemical substitution, isotope substitution, dynamical excitation with light or application of pressure, either hydrostatic, uniaxial or biaxial. It is the latter in which we are most interested, the application of biaxial pressure, or strain, through heteroepitaxy in addition to surface and interface effects that are unique to thin films. The following chapter begins with a general discussion on this.

Chapter 3

Introduction to Thin Film Physics

3.1 What is a Thin Film?

A thin film is simply a solid material but with the third (out-of-plane) dimension greatly reduced with respect to the first two (in-plane) dimensions. Perhaps an important question to address is; how thin is a thin film? In the fundamental research of perovskite oxides, a thin film could be defined as one where the film thickness starts to be on the same order of magnitude as the relevant length scales for the physics, leading to a definition of the dimensionality that depends upon the phenomena in question and can vary. An example would be a "3-D" conductor that becomes a "2-D" superconductor because the elastic scattering length is shorter than the superconducting coherence length. For heteroepitaxially-grown films, another definition could be that a thin film becomes a thick film when the structure begins to relax to its bulk-like parameters, losing the effect of the epitaxial strain. In this work, however, thin films are on the order of tens of nanometers. In Chapter 7 we also make reference to "ultrathin" films, which can be thought of as films where a large portion of the depth is taken up by boundary layers, generally less than 2 nm in thickness. As will be discussed, the ultrathin regime still holds many mysteries.

Films take several forms such as exfoliated lamellae from single crystals or free-standing films [14]. A common method of obtaining a thin film is to grow it from scratch onto a *substrate*, as described in Section 5.1.1. A film could, in principle, be deposited onto any substrate but in most cases this would result in an amorphous or polycrystalline film with potentially poor properties. Far more interesting are films grown *epitaxially*. This means that the structures of the film and the substrate are sufficiently similar as to allow the film to grow with its atoms in registry with the substrate atoms and the crystalline planes

parallel to those of the substrate. Epitaxial growth can be done in the situation where the film is the same material as the substrate or where the two materials are different; homo- and hetero- epitaxy respectively.

In Fig. 3.1 is illustrated how the unit cell lattice parameters of the film match those of the substrate *in-plane* while *out-of-plane* the c-axis parameter of the film, c_{film}, adapts to conserve as much of the bulk volume as possible by expanding (compressive) or contracting (tensile).

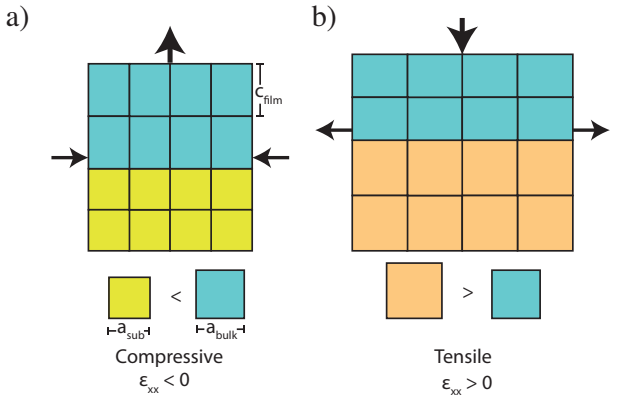

Figure 3.1: A simplified schematic of epitaxial strain when a) the lattice parameter of the substrate is smaller than the lattice parameter of the bulk material to be grown as a film (compressive strain) and b) when the lattice parameter of the substrate is larger than that of the bulk material to be grown as a film (tensile strain).

Biaxial strain can be defined as:

$$\epsilon_{xx} = \frac{a_{sub} - a_{bulk}}{a_{bulk}} \tag{3.1}$$

where a_{sub} and a_{bulk} are the in-plane pseudocubic lattice parameters of the substrate and the bulk material to be grown as a film respectively. As a response to the in-plane biaxial strain, there is a uniaxial out-of-plane strain, ϵ_z. By elasticity theory, the uniaxial out-of-plane strain is of opposite sign to and lower in magnitude than the biaxial in-plane strain. Since almost all materials obey conventional elasticity theory, unit cell volume is typically not conserved in the heterostructuring process and this is captured by the Poisson ratio, ν. The connection between the in-plane and out-of-plane strains is given by eq. 3.2.

$$\epsilon_{zz} = \frac{2\nu}{\nu - 1}\epsilon_{xx} \tag{3.2}$$

Strain, imposed by heterostructuring, is therefore an effective tool to modify the structure of the thin film. In materials with highly directional orbitals,

such as the transition metal oxides, strain can have a profound effect on the properties of the film.

In addition to strain, and perhaps more difficult to describe, are *interfacial* effects, inevitable in growing a thin film on a substrate. These can involve, for instance, structural texturing, magnetic coupling or charge transfer [15, 16]. The boundary between two materials is a strange place indeed, usually featuring chemical, structural or charge discontinuities and it is often here that the strangest phenomena are uncovered. What is difficult is to predict how an interface will develop and the subject is of great importance because sometimes interfacial effects are desired. All electronic devices, for example, are built up from transistors and a transistor is nothing more than a stack of interfaces. Further discussion of interfaces in the context of transition metal oxides can be found in Section 3.3.

To summarise, heterostructuring opens up a whole new parameter space of materials engineering, allowing access to materials sometimes very distinct from their bulk counterparts and often without a bulk counterpart entirely. The possible configurations of substrate, thin film layers, doping, reduced dimensionalities and symmetry make the potential "new" materials almost infinite.

3.2 Challenges

As the potential for thin film applications is seemingly endless, so too is the potential for complications. Thin film physics can be a challenging area to work in, both for theoreticians and experimentalists. With these challenges come solutions and here we address some of these.

Already, growing a material as a thin film can be challenging. Due to the growth conditions, see Section 5.1, some compounds may not stabilise easily and finding the correct parameters to obtain a stoichiometric, epitaxial film can be challenging but can often be achieved through a systematic optimisation.

Then, possibly the first challenge in characterising a new thin film sample is to select the appropriate measurement technique. As the samples are thin by design, the volume is also small. For scattering-based techniques where the signal amplitude is proportional to the scattering volume, thin film scientists must try to salvage intensity in whatever way they can. Tactics have ranged from seeking out high intensity light sources in order to perform sophisticated x-ray diffraction (XRD) to arranging multiple thin film samples together in an attempt to record neutron scattering. The approaches are varied but there is often the need for long integration times, which can really throttle the experimental throughput.

A somewhat related issue is the influence of the substrate, which has a scattering volume orders of magnitude greater than the film. The chemical similarity among perovskite oxides means that often the substrate will produce a signal in similar conditions to that of the film, sometimes completely obscur-

ing the feature of interest. Even if the film signal is visible it can be difficult to extract information when it appears as nothing more than a broad shoulder on a sharp and high intensity substrate peak. In Chapter 7, we discuss the Raman spectroscopy measurements on thin films of only 1nm thickness, results that were obtained using a depth-profile measurement coupled with sophisticated numerical analyses to isolate the film signal from the substrate.

Even aside from the difficulties of deconvoluting the substrate effect from the film, the fact that there *is* a substrate is enough of a problem already as it means the film can only be accessed from one side. Experiments in transmission geometry can be performed but, in general, only with a careful polishing of the back side of the substrate, which itself, of course, must be transparent and insulating. Moreover, if there are structural defects in the substrate, these can be easily carried over to the film so usually a film is only as good, structurally, as the substrate upon which it is grown.

It is clear that thin film experiments come with a whole host of obstacles but it is, nevertheless, possible to obtain high quality substrates, grow a high quality film and go on to measure. This leads to the next challenge; how to understand what is observed.

Often, the film will have a response to the biaxial strain that was not foreseen. It can, for instance, form defects or structural distortions instead of pure changes in bond length. This is summarised for perovskite thin films, which will be introduced in the following section, in Fig. 3.2.

The coupling of the film to the substrate structure is also non-trivial. Substrate termination (in (001)-oriented perovskites, this means A-site or B-site terminated) can drastically change the properties of the film. Chemical and polar discontinuities as well as symmetry mismatches can all play a role in determining the physics of the film. This means that reliably predicting the measurable properties of a thin film is not as simple as calculating the effect of a stretching or compressing of the unit cell.

Multi-component heterostructures are often desired and this adds more heterointerfaces to the situation, bringing more complexity. One challenge can be that the heterointerface is not inversion symmetric, meaning that if material X is grown on material Y the heterointerface will be different than if material Y were grown on material X. For instance, a system where the sequence of growth can change the magnetisation by an order of magnitude [18].

On top, quite literally, of the complications related to the heterointerfaces, is the difficulty in understanding what is happening at the other interface; the one with the vacuum on the surface of the film. It is rather a dramatic thing to do to a material, to suddenly have a surface. There can be uncompensated charges and unbonded atoms, which can produce reconstructions, either electronically, chemically or structurally and even all three together.

It may seem that, by contrast, theoreticians working on thin films have it easy. This could not be further from the truth. In order to produce useful calculations, a theoretician must first choose the unit cell that they will use to

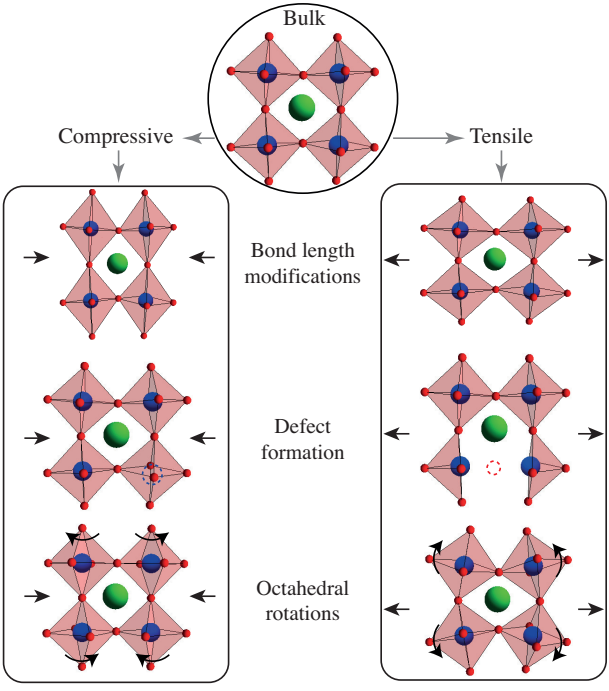

Figure 3.2: How a perovskite structure may accommodate strain by inducing bond length distortions, point defects or octahedral rotations. Adapted from [17].

represent the material they would like to simulate. The lower the symmetry of the material, the larger must be the unit cell and the more computationally intensive the calculation becomes. To accurately represent an ultrathin film, for instance, the unit cell should be taken as a column through the depth of the film to allow for the fact that the lattice structure most likely evolves from interface to surface. The need to account for the reduced symmetry, plus the discontinuities at the boundaries, means that very quickly the limit of computational power is reached. In Chapter 7, we report the results of density functional theory calculations that take into account the full reduced symmetry of the film as well as a coupling with the substrate and the effect of the open surface. In those calculations, the maximum film thickness it is possible to calculate is ten unit cells.

The challenges associated with simulating, measuring and understanding thin films are daunting. There is, however, hope. On both the experimental and theoretical sides, advances are continually being made, conceptual as well as technical. It is only with further development along both these avenues

that the feedback between theory and experiment can be on the order of hours rather than years and the ultimate goal of tailor-made functional materials can finally be realised.

3.3 Thin Film Perovskite Oxides

As discussed in Chapter 2.1, the highly adaptable unit cell of perovskite oxides means that there are hundreds of isostructural crystals all with very similar lattice parameters. The modular nature of the pseudocubic cell means that the structures, and therefore the properties, are highly engineerable as heterostructures. The first step when growing a heterostructure is to select a substrate either to apply the desired biaxial strain level, impose a specific symmetry at the interface or, if the substrate-induced effects are not critical to the study in mind, as simply a means to an end. Fig. 3.3 shows some of the most common single crystal substrates used for oxide heterostructures as well as the bulk structures of $LaNiO_3$ and $NdNiO_3$ used in this work. Prompted by the discovery of high temperature superconductivity in perovskite-like cuprates in the 1980s, many perovskite oxides are commercially available as high quality single crystals, marketed and sold as substrates for thin film growth with a polished surface and known crystallographic orientation. In fact, the substrate LSAT, used in this work frequently, was specifically designed to have a matching lattice parameter to $YBa_2Cu_3O_{7-x}$, the first superconductor found with a critical temperature above the boiling point of nitrogen.

Upon integration in a thin film heterostructure, a TMO may take on rather different properties with respect to the bulk due to the sensitivity of the orbitals to the lattice, as described in the previous section. The primary mechanism by which this is achieved is through the epitaxial in-plane strain. This can be viewed as a tetragonal distortion imposed upon the pseudocubic unit cell of the material. If the oxygen octahedra do not rotate and there are no defects induced in the lattice then all of this tetragonality is accommodated by the bond lengths in a Jahn-Teller-type distortion. The application of compressive strain would decrease the length of the in-plane B-O-B bond while the out-of-plane B-O-B bond is stretched. The increased proximity of the in-plane d-orbitals to the negative oxygen ions serves to push the energy of these orbitals up while, at the same time, stabilising the out-of-plane orbitals that now find themselves with more space to occupy. If the compressive strain is large enough it is reasonable to assume that we may achieve the situation where there is a strong preferential occupation of the out-of-plane orbitals compared to those in-plane, whereas the opposite would occur upon application of tensile strain. This concept of breaking the *orbital degeneracy* is schematised in Fig. 3.4.

Manipulating the orbital occupations by heterostructuring, sometimes called *orbital engineering*, has been suggested as a potential route towards achieving superconductivity in oxides that are not superconducting in bulk.

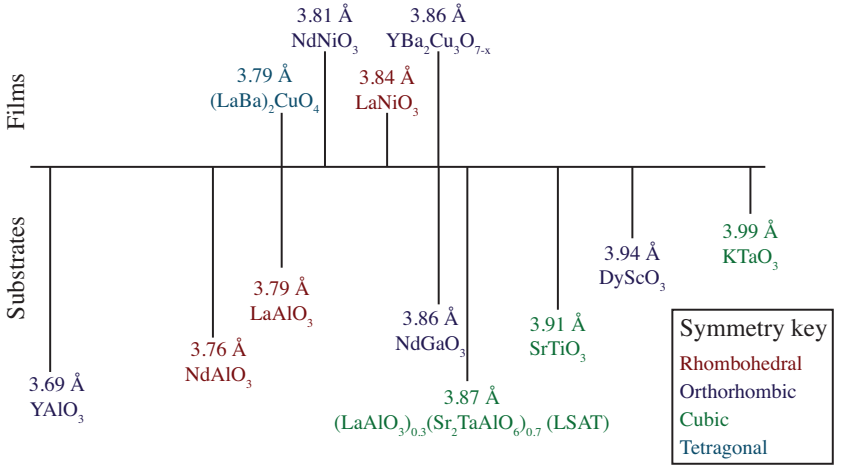

Figure 3.3: A selection of single crystal substrates for thin film oxide growth arranged according to their pseudocubic lattice parameter and compared to the bulk structures of some materials commonly grown as thin films, including those of this work, $LaNiO_3$ and $NdNiO_3$. The colours indicate the symmetry.

See Section 4.6 for a discussion on how this is relevant for studies on $LaNiO_3$-based heterostructures.

Thin films of perovskite oxides are particularly susceptible to depth-dependent variations of structure due to the rather liberal matching conditions from each epitaxial layer to the next: In the (001) crystallographic orientation this consists of just one oxygen atom per octahedron, leaving a great deal of freedom to distort. The propagation of structural distortions has been observed in, for example, transmission electron microscopy measurements and x-ray diffraction but is a computationally intensive effect to capture in theory owing to the large unit cells that would be required [19, 20].

It is not only the structure that can exhibit a depth-dependent profile but the charge as well. O^{2-} is a highly polarisable ion meaning that it can help accommodate significant local modulations of charge in the TM lattice by Coulomb screening the field on a short length scale. Distributions of charge that would otherwise be energetically unstable can build up. Particularly essential in thin films of TMOs, short range modulations are often found at the interface and at the surface [21].

These depth-dependent modulations of the charge and lattice degrees of freedom, which are themselves often coupled to the orbital and spin degrees of freedom, add another layer of complication to the design of functional oxide heterostructures. On the other hand, they are part of the reason for the rich and fascinating physics of this class of materials. For example, the inter-

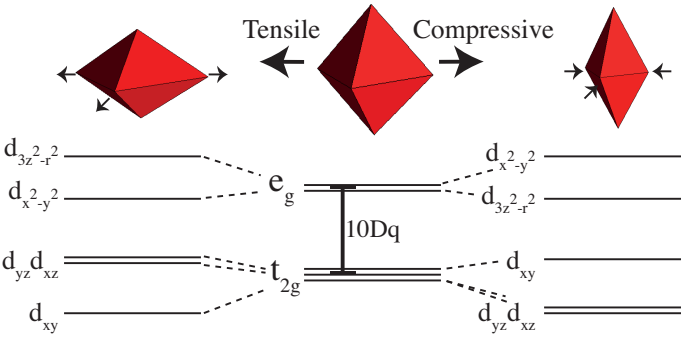

Figure 3.4: How the degeneracy of the e_g and t_{2g} manifolds should be lifted from the non-strained (central) to the strained (on either side) octahedra. Depending on the sign of the strain, either the in-plane or out-of-plane orbitals will be favoured.

face between the band insulators $LaAlO_3$ and $SrTiO_3$ is not only conducting but superconducting [22, 23]. As another example, $LaMnO_3$, an antiferromagnet, becomes ferromagnetic when grown as a thin film on $SrTiO_3$ [24]. These are emergent phenomena, which may only manifest because of the d-orbital physics of transition metals coupled with the interface physics of heterostructures.

Fig. 3.5 summarises, in a simplified manner, the various mechanisms by which heterostructuring allows the degrees of freedom of a complex transition metal oxide to be manipulated.

We now see that we are working at the intersection of two intricate areas of physics. This means we must consider strain effects, interfacial coupling and surface distortions, among many other subtleties of heterostructure physics, convoluted with the immense field of complex oxides and the multiple interplaying parameters and emergent phenomena therein. Many review articles have been published on the subject of heterostructures of complex oxides [15, 16, 25–29] and although in the following sections we will report only on heterostructures of perovskite rare earth nickelates, many of the discussions remain relevant for TMOs as a whole.

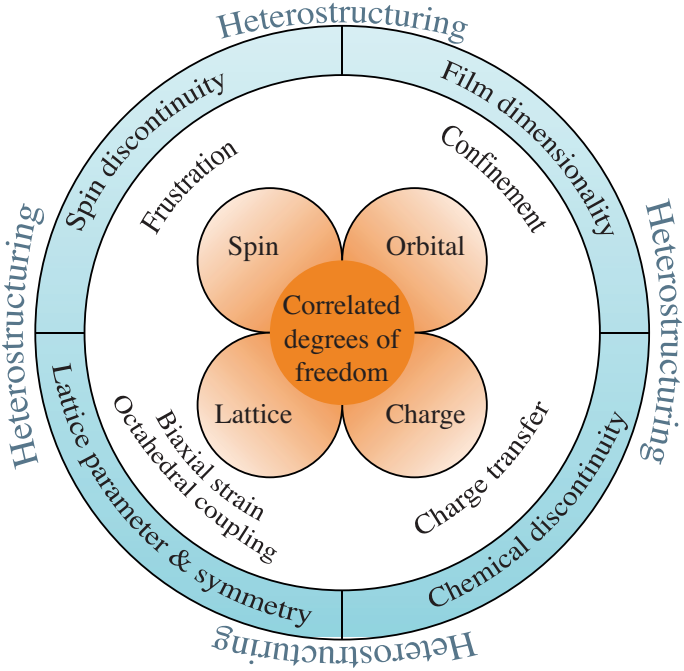

Figure 3.5: A simplified, non-exhaustive schematic of the interplay between heterostructuring and complex oxide physics. The blue ring on the outside represents some parameters controllable by heterostructuring while the orange lobes in the centre represent the correlated phases of transition metal oxide perovskites. Between the two are the primary mechanisms responsible for the manipulation of a given degree of freedom by heterostructuring. Adapted from [15].

Chapter 4

Introduction to the Nickelates

4.1 The Rare Earth Nickelates

Nickelates are one of the central families of the transition metal oxides, serving as a canonical example of the rich physics of TMOs. As perovskites, their chemical formula is $R\mathrm{NiO}_3$ where the R represents a rare earth cation, mostly from the lanthanide series, lanthanum to lutetium, with only cerium, praseodymium and terbium unable to be substituted onto the A-site, probably due to their preferential oxidation state of 4+. As the R substitution progresses along the rare earths, the ionic radius decreases, which enhances the distortion of the lattice structure, bringing the Ni-O-Ni bond angle away from 180 °. The most fascinating aspect of the nickelate family is their rich phase diagram, characterised by the crystal structure, that features several phase transitions, which are described in detail in the following sections (Fig. 4.1) [30–32].

4.2 Electronic Configuration

There have been some challenges in capturing the physics of the nickelates theoretically and this has largely been down to beginning with an electronic configuration that does not represent the nickelates realistically. The rare earths very strongly favour the 3+ valence state, forcing the nickel (a late transition metal atom with eight electrons in its d-shell) to also be nominally 3+ oxidised. After losing the two electrons from the 4s level and one d-electron, the nickel is nominally a d^7 ion in the $R\mathrm{NiO}_3$ series. However, due to the charge transfer with oxygen, it is most likely actually $d^8\underline{L}$ with an extra electron on the nickel and a hole on the oxygen (represented by the $\underline{L}$) [34, 35]. This is

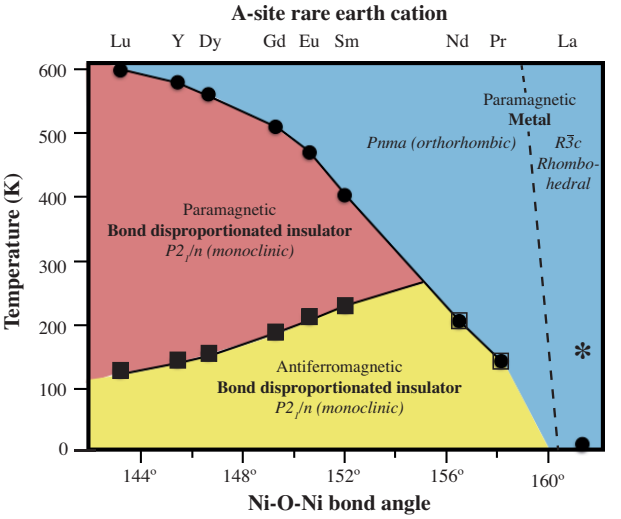

Figure 4.1: The bulk phase diagram of the rare earth perovskite nickelates showing the temperatures of the metal-insulator (circles), paramagnetic-antiferromagnetic (squares) and structural transitions as a function of the Ni-O-Ni bond angle or, on the top axis, the rare earth cation substituted onto the A-site. The asterisk represents the recent report of antiferromagnetism in single crystal $LaNiO_3$, discussed later [33]. Adapted from [30]

crucial because it means that we must consider the nickel-oxygen complex to fully understand these materials. One of the key outcomes is that the nickelates may have not one but *two* electrons in the e_g orbitals. The correct starting point of the electronic configuration is critical for the kind of *orbital engineering* that was theorised to lead to superconductivity in $LaNiO_3$-heterostructures, discussed at the end of this chapter [36].

4.3 The Nickelate Phase Transitions

4.3.1 The Metal-Insulator Transition

Perhaps the most famous feature of the $RNiO_3$ family is the sharp metal-to-insulator transition (MIT) with decreasing temperature. The MIT occurs at progressively higher temperatures as the size of the rare earth ion is reduced and, hence, the orthorhombicity increased, representing a bandwidth-controlled transition, see Fig. 4.1. Fig. 2.5c) illustrates the dependence of the bandwidth on the B-O-B bond angle, in this case the Ni-O-Ni bond angle. For the largest rare earth, R = La in $LaNiO_3$, the structure is not distorted enough to stabilise

the insulating phase at a finite temperature but, if grown as a thin film, $LaNiO_3$ will eventually become insulating at the lowest thicknesses, a state that is discussed thoroughly in Chapter 7. All the other nickelates enter an insulating state that is, most likely, distinct from the ultrathin insulating state of $LaNiO_3$ and cannot be described by conventional band theory since the system is electronically partially filled.

A great deal of theoretical work has gone into the understanding of the MIT in nickelates [37–44]. Without providing a detailed account of these various efforts, a brief description of the MIT will be given here.

The nickelate ground state can be explained in the context of the physics of negative charge transfer insulators, introduced in Section 2.2. Taking into account the starting configuration in the metallic phase of d^8L, the symmetry lowering process corresponding to the MIT is:

$$d^8L + d^8L \longrightarrow d^8L^2 + d^8 \tag{4.1}$$

giving two distinct nickel sites, a *disproportionation* [45]. The d^8L^2 site draws the oxygens closer to the nickel, resulting in a smaller O_6 octahedral cage and a stronger Ni-O hybridisation, while the d^8 state has the opposite effect. Fig. 4.2 illustrates the 3-dimensional chessboard distribution of the inequivalent nickel sites. Large and small octahedra represent the bond disproportionation that takes place during the MIT. The MIT is thus concomitant with a structural distortion based on this bond disproportionation, discussed in Section 4.3.3. While both types of nickel host eight electrons, six in the t_{2g} orbitals and two in the e_g orbitals, there is still a disproportionation of charge *density* between the two sites, which may be important in the context of so-called negative U centre superconductivity, see Chapter 8.

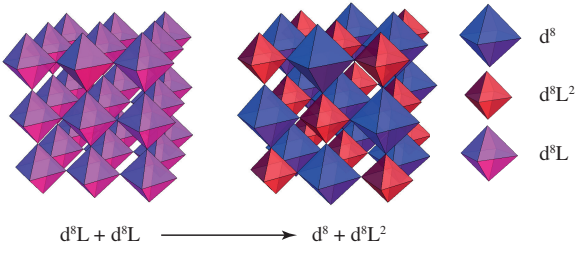

Figure 4.2: A representation of the metal-to-insulator transition in nickelates showing how the electronic configuration disproportionates within the ligand hole picture.

Moving to the low energy picture, where only the nickel e_g orbitals are considered, the MIT can be described by:

$$d^7 + d^7 \longrightarrow d^8 + d^6 \tag{4.2}$$

where the d^8 site is half-filled and Mott-like while the empty e_g of d^6-character is pushed up in energy [40]. This scenario has been called a "site-selective Mott insulator" and, compatible with the ligand hole theory, is associated with both bond and charge density disproportionations. An alternative description has the MIT driven by a structural instability [43].

The MIT is highly tunable by application of hydrostatic pressure [46], light [47], isotope substitution [48] and, in heterostructures specifically, by strain [49–52] and growth orientation [53]. All this highlights the strong coupling of the charge and lattice degrees of freedom.

4.3.2 The Néel Transition

As indicated in the phase diagram of Fig. 4.1, there is a second transition occurring with lowering temperature; the paramagnetic to antiferromagnetic transition.

Contrary to the MIT, the Néel transition temperature increases with the straightening of the Ni-O-Ni bond angle. This trend continues until $NdNiO_3$ in bulk, where the decreasing stability of the insulating phase brings charge fluctuations that suppress the magnetic ordering such that the Néel transition and the MIT occur simultaneously for further increasing Ni-O-Ni bond angle. The two transitions are finally quenched as the bond angle increases still further, leaving only $LaNiO_3$ without any transitions in bulk. However, recent reports on high quality $LaNiO_3$ single crystals find a static magnetic order at finite temperature in this material that has not been observed previously [33]. This is discussed further in Section 4.5.1.

As discussed in the previous section, the MIT involves a symmetry-lowering to a bond- and charge density-disproportionated state. In the insulating phase, the d^8L^2 shares two electrons from the surrounding oxygens that are very weakly spin-polarised and the d^8 has two electrons in the e_g orbital but in high spin configuration, in the extreme case, S = 0 and S = 1 respectively. The alternating small and large octahedra stabilise what is known as a breathing mode, resulting in a 3-dimensional chessboard structure, see Fig. 4.2. In such a structure, the $[111]_{pc}$ direction becomes one of the most highly ordered and each plane in the $(111)_{pc}$ family consists only of one type of nickel. For this reason it is perhaps not surprising that the AF order is established along the [111] direction. More unusual, however, is that the antiferromagnetism stabilises with a rather long periodicity, requiring four (111)-planes of nickels before repetition, giving a characteristic ordering of $(\frac{1}{4},\frac{1}{4},\frac{1}{4})_{pc}$ [54]. Further studies showed that the AF-order is not associated with any additional orbital ordering and it is instead represented by a pure spin density wave [55]. Also demonstrated was that, in bulk, the spin density wave is well-described by a non-collinear spin arrangement and a possible structure is suggested in Fig. 4.3.

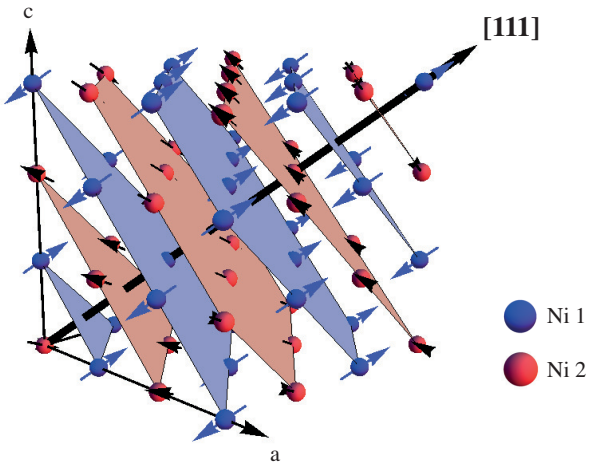

Figure 4.3: A possible magnetic structure of the rare earth nickelates. The two inequivalent nickel sites are illustrated by the blue and red balls and the magnetic moments as arrows. The (111) planes are highlighted, also in blue and red. In bold is the [111] vector.

4.3.3 The Structural Transition

In addition to rich electronic and magnetic phases, the nickelate family also hosts at least two structural transitions.

Already mentioned is the one concomitant with the MIT in bulk. This corresponds to a symmetry lowering from $Pnma$, above the MIT, to $P2_1/n$, in the insulating phase. $Pnma$ is a space group of orthorhombic symmetry with a Glazer rotation system of $a^+b^-b^-$. Often the notation $Pbnm$ is preferred as this aligns the in-phase Glazer rotation with the out-of-plane direction for thin films but the two space groups are otherwise identical and $Pbnm$ is interchangeable with $Pnma$. Once the system has undergone the MIT, and associated bond-disproportionation, it is left in a monoclinic structure, $P2_1/n$. In this state there are still two out-of-phase Glazer rotations and one in-phase rotation but the rotation magnitudes are now all different; $a^+b^-c^-$. This type of transition takes place in a smooth, continuous fashion and can be described as a second order transition.

The second structural phase transition appearing in the nickelate phase diagram is much less studied. The only bulk nickelate that is metallic at all temperatures, $LaNiO_3$, is also different to the rest of the family in terms of the structure. It is not only the least distorted in bond angle but it belongs to a separate room temperature space group altogether, $R\bar{3}c$. This corresponds to

rhombohedral symmetry and a Glazer rotation system of $a^-a^-a^-$. A direct transition from $R\bar{3}c$ to $Pnma$ is forbidden by the group-subgroup relations (recall Fig. 2.3) but this is a transition that is seldom relevant except in the study of solid solutions of $LaNiO_3$ and one of the other *R*NiO_3 compounds. This will be addressed further in Chapter 8.

These symmetry changes are readily probed. In this work we employ x-ray diffraction and Raman spectroscopy and both techniques are described in the subsequent chapter.

4.4 Thin Film Nickelates

There is a lot of interest in nickelates because they constitute a fascinating study of phase transitions, of which the sharp and highly-tunable MIT is especially appealing in the context of applications [56].

Hindering study for many years was the difficulty in obtaining high quality single crystal samples, although, very recently, reports are beginning to appear on this subject [33, 57]. This meant that, in the laboratory, nickelates could only be developed as polycrystalline powders or grown as thin films.

As it happens, nickelate thin films are fascinating in their own right and exhibit several phenomena that emerge from the interplay between heterostructure physics and the chemistry of transition metal oxides. It is found, for instance, that the MIT and Néel transitions can be strongly modified by epitaxial strain and crystallographic orientation [49–53].

4.5 $LaNiO_3$

The central compound of this thesis is $LaNiO_3$, the only nickelate that is metallic at all temperatures in bulk. Much of the research interest in $LaNiO_3$ comes from the more applied side of science. Given its low resistivity (less than 100 $\mu\Omega cm$), it is often integrated as an electrode in oxide heterostructures [58–60]. As a more functional device element, $LaNiO_3$ has also been used in the context of catalysis [61] and gas sensing [62], amongst others.

$LaNiO_3$ is also widely studied from a fundamental perspective as it constitutes an archetypal correlated metallic oxide. This section will address two open questions pertaining to the nature of $LaNiO_3$ that have drawn a great deal of interest from the physics community; namely, the possibility of magnetic order and the potential to engineer a superconducting heterostructure.

4.5.1 Magnetic Order in $LaNiO_3$

According to the established bulk phase diagram for the nickelates, which was based on polycrystalline samples, $LaNiO_3$ is the only member of the family

that is paramagnetic and metallic at all temperatures [31]. Recently, however, high quality crystals of $LaNiO_3$ have been synthesised making it possible, for the first time, to access macroscopic physical properties on bulk single crystal samples [33, 57].

While Ref. [57] finds crystalline $LaNiO_3$ to be paramagnetic with a slight susceptibility enhancement around 200 K, Guo and coworkers (Ref. [33]) observe a Néel transition at 157 K. This is the first time that static antiferromagnetism has been reported in $LaNiO_3$ in any form and this result is even more surprising given that these samples also have a very low resistivity, on the order of $\mu\Omega cm$. A likely explanation has been provided by Wang and coworkers, who find a direct link between oxygen deficiency and magnetic phases in $LaNiO_{3-\delta}$ [63]. Oxygen vacancies would also go a long way to explaining the unusually high conductivity as well. It is interesting, however, that AF order appears to exist in quite close energy proximity to the paramagnetism that is normally measured.

As part of this thesis, resonant soft x-ray diffraction was carried out on a 30 u.c. thin film of $LaNiO_3$ on (001)-oriented $LaAlO_3$, which was metallic, as expected, with a 4 K resistivity of 60 $\mu\Omega cm$. No diffracted intensity was found at the $(\frac{1}{4},\frac{1}{4},\frac{1}{4})_{pc}$ Bragg peak despite a thorough search.

Magnetism in $LaNiO_3$-based heterostructures has mostly been studied in systems that place $LaNiO_3$ beside $LaMnO_3$ because interfacial charge transfer brings the nickel towards a 2+ oxidation state [64,65]. Further, in superlattices of $La_{\frac{2}{3}}Sr_{\frac{1}{3}}MnO_3$ and $LaNiO_3$ a non-collinear magnetic order was observed even in layers of the $LaNiO_3$ that should not be affected by the charge transfer [66].

The idea that $LaNiO_3$ could become antiferromagnetic by heterostructuring is not unreasonable. After all, as discussed in Chapter 7, ultrathin films of $LaNiO_3$ become insulating so an AF order could be envisaged in this state. In fact, signatures of antiferromagnetism have been reported on superlattices of 2 u.c. of $LaNiO_3$ alternated with a band insulator [67]. It is possible that growing ultrathin $LaNiO_3$ renders the material like the other *R*NiO_3 compounds below the MIT. The other nickelates, however, also appear to have an ultrathin insulating phase, even at high temperature. Crucially, bond disproportionation of the type that characterises the nickelate MIT and allows the magnetic wave vector to propagate is not observed for the ultrathin regime [68]. In other words, this state may not be the *right type* of insulating state for antiferromagnetism.

Even if observations of a true AF state in isolated $LaNiO_3$ have not been confirmed, and were likely due to oxygen nonstoichiometry, there is evidence that this material is not impervious to induced magnetic ordering. In $(111)_{pc}$-oriented superlattices of $LaNiO_3$ and $LaMnO_3$, an insulating antiferromagnet, complex magnetic ordering was reported with a strong dependence upon the $LaNiO_3$ layer thickness [69]. The model proposed to explain this behaviour suggests that the $LaNiO_3$ is able to propagate the magnetic order from one $LaMnO_3$ layer to the next through an interfacially-induced magnetic moment.

Crucially, the coupling between the neighbouring $LaMnO_3$ layers is only antiferromagnetic when the $LaNiO_3$ thickness is 7 (111) monolayers. If the $LaNiO_3$ stabilises the same non-collinear $(\frac{1}{4},\frac{1}{4},\frac{1}{4})_{pc}$ AF ordering as the other nickelates then this thickness corresponds to $1\frac{3}{4}$ of the wave vector. The long distance antiferromagnetism of the $LaMnO_3$ is then readily explained by the total moment of the first $LaNiO_3$ layer being equal and opposite to the total moment of the seventh $LaNiO_3$ layer. The same situation should happen when the $LaNiO_3$ thickness is 3 monolayers or 11 monolayers ($\frac{3}{4}$ and $2\frac{3}{4}$ of the AF wavevector respectively) but one of the important outcomes of the study is that it does not. The $LaNiO_3$ can only propagate the magnetic ordering when the thickness is 7 (111) monolayers because, most likely, at 3 monolayers the system is too intermixed and at 11 monolayers the $LaNiO_3$ is already metallic and the delocalised electrons probably disturb the antiferromagnetism.

It now seems unlikely that $LaNiO_3$ is a rare example of a metallic antiferromagnet, at least when the oxygen content is stoichiometric, and it is not known if its ultrathin state is analogous to the insulating, antiferromagnetic ground state of the other nickelates. It does, at least when insulating, seem to be a willing ally of antiferromagnetism.

4.6 The Motivation Behind $LaNiO_3$-Based Heterostructures

High temperature superconductivity in copper oxides, since its discovery in 1986 (Ref. [70]), kickstarted a huge drive in research efforts towards pushing the critical temperature (T_c) up, the ultimate goal being a room temperature superconductor. To have all the applications of a superconductor with no expensive and cumbersome cooling system necessary would change the face of technology.

Without a detailed understanding of the mechanism underlying high temperature superconductivity, it is challenging to know how to engineer it. A popular approach has been to systematically check for superconductivity in compounds that are chemically and structurally similar to those that are already known to superconduct.

The cuprate high T_c superconductors have a structure that consists of layers of perovskite or perovskite-like planes. As discussed in Section 2.1, perovskites can accept a wide variety of cations and, when taking into account solid solutions and double perovskites, there is almost an infinity of chemical configurations. Given that the number of compounds synthesised and measured is a very small subset of the possible materials, it is likely that there are still high T_c superconductors waiting to be discovered. To guide in the search a little better, studies have generally taken an empirical approach.

Undoped, cuprates contain Cu^{2+} ions, which puts the copper into the d^9

ground state. This means that there are three electrons in the e_g orbitals; two fill the $d_{3z^2-r^2}$ leaving the $d_{x^2-y^2}$ orbital half-occupied, the non-degeneracy of these orbitals being discussed shortly. Just to the left of copper on the periodic table is nickel, which is nominally d^7 in the perovskite oxides, leaving one electron in the e_g orbitals. There are some similarities between nickelates and cuprates but also some differences. The cuprates, as mentioned, are layered materials consisting of conducting copper oxide planes whereas the nickelate structure is 3-dimensional. Furthermore, there is a substantial orbital degeneracy-breaking in the cuprates, meaning that the $d_{3z^2-r^2}$ orbital is lower in energy than, and therefore occupied preferentially to, the $d_{x^2-y^2}$ one. The resulting single-band character may be related to the high T_c superconductivity. The nickelates, on the other hand, exhibit no such orbital degeneracy-breaking in bulk and no Jahn-Teller-like distortion is observed in these materials [31]. Lacking 2-dimensionality and a broken orbital degeneracy, the nickelates could have been written off as potential superconducting systems were it not for advances in heterostructuring.

In 2008 it was suggested that superlattices of 1 unit cell (u.c.) layers of metallic $LaNiO_3$ alternated with a non-transition metal oxide band insulator may provide the ideal environment for superconductivity [36]. The atomic layers of nickel bring 2-dimensionality while the tensile epitaxial strain should split the degeneracy between the two e_g orbitals according to the schematic in Fig. 3.4.

The suggestion of Chaloupka and Khaliullin more than ten years ago, unsurprisingly, prompted a lot of research effort on these types of heterostructures, spurred on by calculations that seemed to add validity to this approach [71,72]. To date, however, no superconductivity has been reported, although the quest has produced some exciting results [73–75]. In fact, all such heterostructures are insulating. The reason for this lack of success may be fourfold:

To begin with, the starting assumption that the nickelates should have single-electron character, similar to the cuprates, may be a bit off the mark. As discussed at the beginning of this chapter, the electronic configuration of the nickelates is not as expected. There is, very likely, not one but two electrons in the e_g orbitals, the second one coming from the oxygen 2p ligand.

A second possible explanation for the lack of superconductivity in nickelate heterostructures is representative of one of the complications of heterostructure physics in general; that the structure may not adapt to the epitaxial strain in the way expected. In this case, it is possible that the oxygen octahedra do not accommodate the new tetragonality in the manner sketched in Fig. 3.4. It is very likely that instead of simply stretching or compressing their bonds to fit their new constraints, they also rotate and tilt, an effect that has been documented in nickelates already [76]. A rigid rotation of octahedra does not change the immediate oxygen coordination environment of the nickel and so the orbitals would be expected to react minimally in this case. Chapter 6 is dedicated to measuring these types of structural distortions.

Another likely issue is that the single unit cell layers of $LaNiO_3$ are found to be insulating, despite the bulk metallicity of $LaNiO_3$. The fact that these *ultra-thin* layers are insulating, when thicker layers are metallic, discussed heavily in Chapter 7, indicates that there is still a missing piece of the puzzle when the film thickness approaches the atomic limit. If the building blocks do not behave as expected it should come as no great surprise that the superlattice that repeats these blocks does not behave as expected.

Finally, possibly the most subtle point: strain engineering a complete orbital polarisation has very been challenging in nickelates but has prompted the development of advanced measurement techniques that can probe the layer-resolved orbital polarisation [73]. The highest orbital polarisation that has been achieved in bi-component superlattices of the type initially proposed by Chaloupka and Khaliullin is 25 % [74].

Greater enhancement of the orbital polarisation than that brought by just biaxial strain was suggested to stem from induced interfacial charge transfer when the band insulator is replaced with $LaTiO_3$, a Mott insulator [77].

Going up to tri-component superlattices was put forward as a possible route towards an even greater orbital polarisation [78]. Indeed, 50% orbital polarisation was found in superlattices of 1 u.c. slabs of $LaTiO_3/LaNiO_3/LaAlO_3$ that reach this enhancement due to the combined effect of the interfacial charge transfer and the broken inversion symmetry [75]. This remains the highest orbital polarisation achieved in nickelates.

The reason for this apparent experimental limit to orbital polarisation is not fully understood but may stem from the challenge in predicting the physics of complex transition metal oxides. Particularly, the nickel d-orbitals are hybridised with the oxygen 2p orbitals and may also be subject to strong Hund's coupling, making the electronic configuration preferentially high-spin shared between the t_{2g} and e_g manifolds [79–81].

Chaloupka and Khaliullin's synthetic superconductor that has yet to be realised exemplifies the difficulties of materials design in both the fields of complex oxides and of thin films, summarising neatly both the previous chapters.

Whether for lack of single crystal samples or to employ heterostructuring as a engineering strategy, the research on nickelate thin films has been extensive with detailed review articles being published on the subject [56, 82]. Making all this possible is the rapid advancement of experimental and simulation techniques adapted to thin film physics. The following Chapter will describe those most relevant for the present thesis.

Chapter 5

Experimental Techniques

5.1 Thin Film Growth

To meet the demand for high-quality epitaxial thin films, numerous growth techniques have been developed. Most of them can be classified into one of two categories; chemical vapour deposition (CVD) or physical vapour deposition (PVD). CVD is widely used in the semiconductor industry and involves a chemical reaction directly on the surface of the substrate [83]. Perovskite oxides, however, are usually grown by one of the PVD techniques; pulsed laser deposition (PLD), molecular beam epitaxy (MBE) or sputtering.

In PLD, a high intensity laser is pulsed onto a target with the desired stoichiometry of the final film (or off-stoichiometry to account for ion loss during transfer to the substrate). The ions of the target are ablated into a high energy plume of plasma. The substrate is generally positioned close to the tip of the plume where the ionic species are deposited and gradually build up the thin film.

MBE, on the other hand, requires separate sources of each element of the final material, which are heated to sublimation inside an effusion cell or evaporator. Upon reaching the substrate, the *beams* of material from each source are deposited and interact with one another. In the correct conditions (substrate temperature, pressure, oxygen atmosphere) the thin film will grow stoichiometrically and epitaxially.

Often, *in-situ* characterisation of the film growth is made possible by techniques such as reflection high energy electron diffraction (RHEED), which can provide information on the growth mode, surface quality and film symmetry as well as give a live measurement of the film growth.

The nickelate films studied in this thesis were all prepared by radio frequency (RF) off-axis magnetron sputtering, a type of PVD especially well-suited to the growth of oxide thin films [84].

5.1.1 RF Off-Axis Magnetron Sputtering

DC Sputtering

Sputtering involves bombardment of a target by a flux of particles. The bombardment must take place in the correct energy regime for effective sputtering. Fig. 5.1 illustrates the possible situations, depending upon the incident kinetic energy. At around 10 eV, the incident particles (red arrow) lack the energy to interact effectively with the target atoms (in blue). Between about 100 eV and 1 keV is the so-called "knock-on" regime. In this energy range, some surface atoms of the target are dislodged and this has a *knock-on* effect on the surrounding atoms. Eventually it is possible that a target atom is hit from below and is ejected entirely, becoming a sputtered atom. It is in this regime of hundreds of eV that sputtering deposition takes place. If the incident kinetic energy is further increased, a significant portion of the target is vaporised via a cascade mechanism. For bombarding energies exceeding 100 keV, the reduction of the collision scattering cross section means that the incident particle enters the target and is implanted [85].

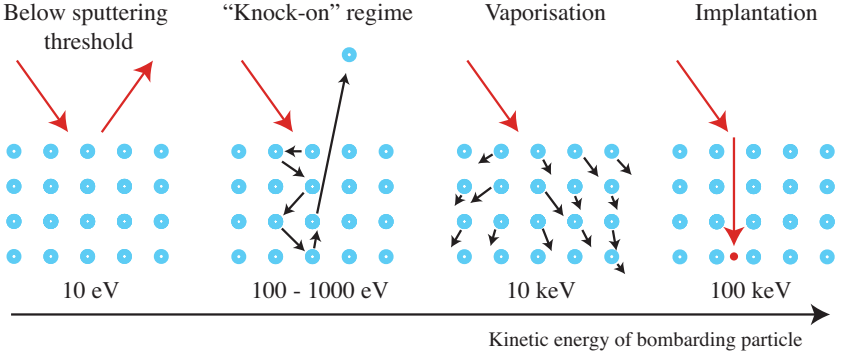

Figure 5.1: The different regimes of sputtering, depending upon the kinetic energy of the bombarding particles (red).

Typically the bombarding particles are argon ions, chosen because argon is both heavy and inert. They are created by introducing argon gas between two electrodes and applying an electric field sufficient to create a cascade of ionisation of the atoms and form a plasma. In order to direct the Ar^+ ions to sputter the target, the system is designed such that the target is the negative cathode and the entire rest of the sputtering chamber, including the substrate, is the positive anode. At the right energy, atoms of the target will be ejected, as described in Fig 5.1. Then, with a heated substrate placed in the chamber, some target atoms will reach the surface and the film will begin to grow. It is in this way that metal films are grown efficiently and on an industrial scale. There is, however, an added complication when the desired material is not a

metal.

AC Sputtering

Often, the films we want to grow are insulators, and so too will be the stoichiometric targets. In this case, there is no way to screen the build up of Ar^+ ions on the surface of the target. A strong electric field then forms inside the target that will eventually cancel out the external electric field. The argon plasma will be extinguished and the sputtering process will come to an end. To circumvent this issue, the external electric field can be regularly switched, in other words, we turn to AC sputtering to avoid the build up of charge on one of the two electrodes.

There is a further difficulty to overcome, however. When the Ar^+ ions are being accelerated towards the target, sputtering happens as normal, but with the other direction of electric field, the ions can bombard the growing film, resulting in damage to the sample. To avoid this undesirable side effect, the frequency of the AC field can be selected such that the (light) electrons can respond to it but the (much heavier) argon ions cannot. It turns out that this is in the radio frequency (RF) domain and a generator at 13.56 MHz is typically used. The Ar^+ ions then only respond to the average electric field, which exists despite the AC due to the relative sizes of the two electrodes. When the target is in the positive half of the AC cycle, the electron concentration is much higher than during the other half of the cycle because, then, the same number of electrons are spread over the entire sputtering chamber. This means there is a net negative bias on the target and it is this bias part of the electric field that the positive argon ions feel and respond to. After all that, the bombardment particles are still drawn to the target yet there is minimal charge build up and a reduced resputtering of the sample. This process is explained in Fig. 5.2

Atmosphere

To minimise contaminants, the growth chamber is kept at a base pressure on the order of 10^{-7} mbar by a chain consisting of a ultra high vacuum (UHV) pump, separated from the chamber by a valve, in turn pumped by a primary pump. The pressure is monitored by a gauge inside the chamber. During the growth, because sputtering involves a plasma, the atmosphere in the chamber must contain the plasma element, here argon, and be at relatively high pressure (tenths of a millibar). In addition, it helps for oxide films to be oxidised during growth and so a mix of argon and oxygen is in fact the best atmosphere [86]. The two gases are introduced to the chamber through gas flow valves. Both the pressure valve and the gas flow valves are controlled remotely in order to keep the atmosphere inside the chamber stable. For the samples grown as part of this work, the atmosphere was 2:7 oxygen:argon and maintained at 0.24 mbar.

Although oxide samples are better to be grown with some oxygen in the

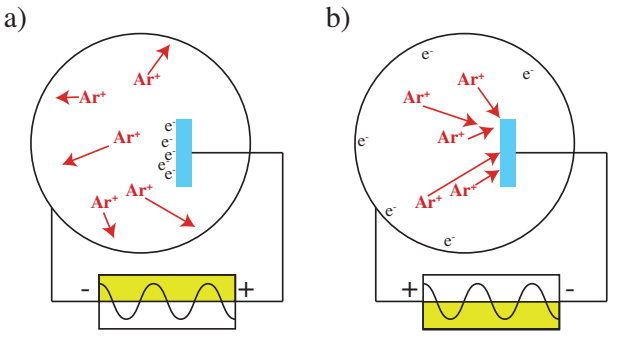

Figure 5.2: Schematics to show how the charged particles of the plasma behave under the AC field during a) the half cycle where the target is positive and b) the half cycle where the target is negative. The average over the full cycle is a net negative "DC" bias on the target, which means that the positive argon ions are attracted to it overall.

atmosphere, this can present a technical problem. The oxygen atoms, as well as the argon atoms, will be ionised in the plasma. Unlike argon, however, oxygen can be negatively ionised. These O^- tend to be attracted to the positive side of the DC bias, meaning the walls of the chamber and, more importantly, the sample. This leads to the resputtering issue again. Fortunately, a solution was found in changing the geometry of the sputtering system; to go from on-axis (the substrate is facing the target directly) to off-axis (the substrate is positioned at 90° to the target) [84]. This removes the substrate from the path of the highest energy particles and drastically reduces resputtering. Despite the decreased growth rate, typically on the order of tens of nm per hour, the off-axis geometry remains the most popular for sputtered oxide films due to the higher sample quality obtained.

Sputtering Guns

The sputtering gun is the piece of apparatus onto which the target is fixed. A sputtering chamber can comprise multiple guns, more guns being useful for the preparation of multilayer heterostructures as the entire structure can be deposited in one growth without the need to transfer the sample from chamber to chamber.

The targets used in sputtering deposition are usually stoichiometric with respect to the desired sample. They typically take the form of high-density pressed ceramic powders.

RF generators usually have a supply impedance of 50 Ω but, for the best efficiency, the supply impedance should match the plasma impedance, which is system-dependent and can drift. In order to maintain the efficiency of trans-

ferred power, therefore, the power supply is connected via a matching circuit, which is automated to continually adjust the capacitors inside.

The *magnetron* part of the name "RF off-axis magnetron sputtering" comes from the fact that the target is fixed to a cylindrical magnet. Fig 5.3 shows how the magnetic field lines produced from the magnetron work to keep the electrons close to the surface of the target, increasing ionisation. This increases the sputtering rate while simultaneously reducing the probability of negatively charged ions reaching the substrate to resputter the growing film [87].

To protect the target, the magnet and the electronics, the sputtering gun contains a cooling circuit. Finally, there is a shutter fixed in front of the gun, which is only opened during sputtering of that target. This prevents cross contamination between targets.

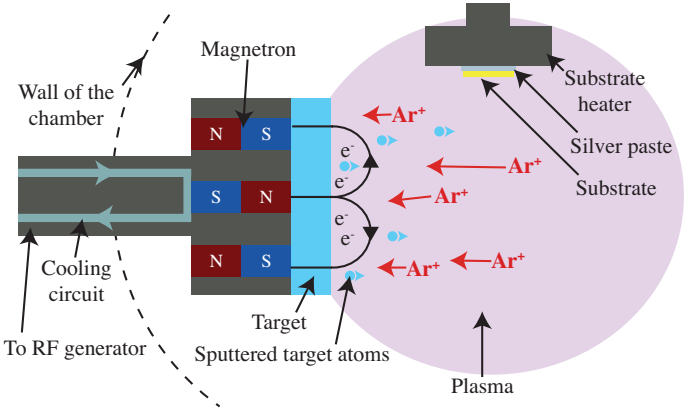

Figure 5.3: The main components of a sputtering gun to illustrate, in particular, how the magnetic field created by the magnetron confines electrons close to the surface of the target. Also shown is the substrate heater in off-axis geometry, not to scale.

Substrate Temperature

With the substrate at room temperature, the film deposited would be mostly amorphous or nanocrystalline. This can be useful, for example, in patterning or in producing control samples. In general, however, we would like our thin films to be of the highest quality and this can only be attained when the substrate is heated to hundreds of °C. The nickelate samples of this thesis were grown between 450 °C and 510 °C. As this is not particularly high, it suffices to paste the substrate onto a resistive block heater with silver epoxy. Inside the resistive block there is a thermocouple and the temperature can then be PID controlled by computer.

Characterisation of Sputtered Samples

Due to the strong permanent magnets of the sputtering guns, *in-situ* monitoring of the film growth by RHEED is not possible except in highly specialised set ups that carefully control the magnetic field [88]. This lack of live information during growth is the primary disadvantage of magnetron sputtering. Although it is generally not possible to know about the sample during the growth process, post-characterisation can provide vast amounts of information. The following section covers the various approaches to characterisation used as part of this work. These methods, coupled with a high level of repeatability from a very reliable growth technique, allow thin film heterostructures from RF magnetron sputtering to be engineered down to the atomic scale.

5.2 Thin Film Characterisation

5.2.1 Atomic Force Microscopy

One of the first ports of call with a new thin film sample is to check the surface quality by atomic force microscopy (AFM). Microscopy, itself, refers to any technique that images objects that are too small to be seen by the naked eye. AFM is a broad name for a family of surface-sensitive techniques performed by passing a microscopic tip over a sample in a controlled way. In this work, AFM was employed to record only topographic maps of the film surface but it is a versatile technique with a lot of variants. AFM, in general, can provide access to a wide range of physical information from electric polarisation to magnetism [89].

To perform AFM topographies, the tip is tapped on or just above the surface of the sample, close enough that the atoms of the sample interact electrostatically with the atoms of the tip. This interaction causes changes in the oscillation amplitude of a cantilever. Then, the amplitude is used as an input into a feedback loop keeping the tip-sample distance constant, allowing reconstruction of the sample topography when the tip is scanned laterally. Fig. 5.4 shows the AFM topography of a $(001)_{pc}$-terminated $DyScO_3$ substrate (in a) and the same substrate now with a 30 unit cell thin film of $LaNiO_3$ (bulk lattice parameter = 3.84 Å) deposited on top of it (in b). In c) is shown the profile of the step-terrace structure of the film. From the profile it can be seen that there is a very low roughness and that the steps measure one $LaNiO_3$ unit cell in height, indicating a single-site terminated surface.

Commercially purchased substrates always come with a certain "miscut" angle. This is a shallow angle, usually less than 0.1 °, that defines the surface of the substrate with respect to the atomically flat termination planes. In perovskites, for mixed A-site and B-site termination the miscutting produces step-terraces of half unit cell height and for single site termination the steps

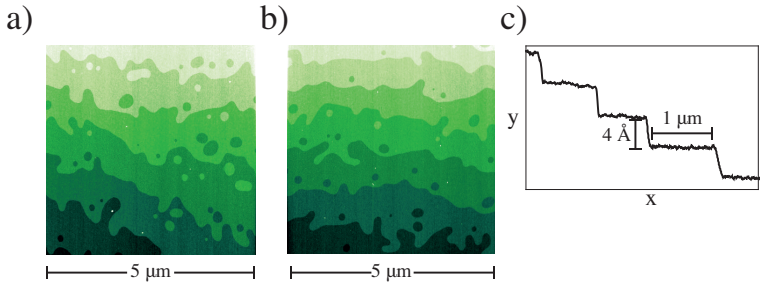

Figure 5.4: AFM topographies of a) a $(001)_{pc}$-oriented $DyScO_3$ substrate and b) a 30 u.c. $LaNiO_3$ film grown on exactly the same substrate. The similarity in topography highlights the topographically faithful nature of the growth. In c) is the height profile across the unit cell steps.

are a complete unit cell. In Fig. 5.4, the film topography is the same as the substrate topography.

If the topography of the film differs significantly from that of the substrate, especially if the terraces are obscured or there are islands of material, this points towards suboptimal growth conditions that may need to be readjusted. In this way, AFM is valuable in the characterisation of thin film samples but it is not the only method used and neither should it be; complementary information on sample quality is normally obtained from x-ray diffraction.

5.2.2 X-Ray Diffraction

Like many experimental probes in condensed matter physics, x-ray diffraction (XRD) is a *"photon in - photon out"* technique. It relies upon the phenomenon of Bragg diffraction, which occurs when many physical obstacles are arranged with some level of periodicity. Very generally, an incident wave is scattered elastically from the obstacles. Since the scattered wave is emitted radially and coherently from each obstacle, and the obstacles are regularly spaced, there emerges a pattern where the scattered waves interfere with each other. The condition for the waves to interfere constructively is when the path difference between them fits exactly an integer number of wavelengths, see Fig. 5.5. Geometrically this gives a a condition of $n\lambda = 2dsin\theta$, the Bragg law of diffraction [90]. The diffraction intensity can be measured in varying angle to obtain a *diffraction pattern*. The resulting diffraction pattern is simply the square of the Fourier transform of the array of scattering points. If the sample is large enough that the scattering array can be considered infinite, then the Fourier transform is a discrete spectrum of peaks. The case where this assumption does not hold is discussed later.

Diffraction works whether the waves are sound, light or even water waves.

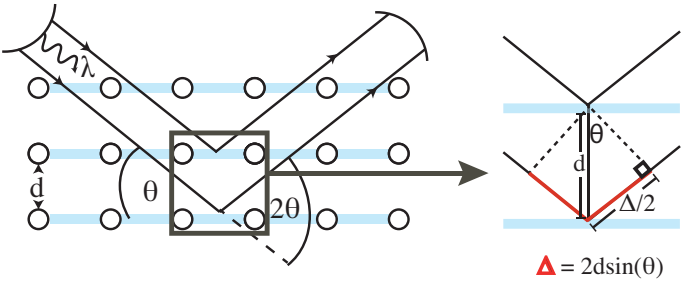

Figure 5.5: Schematic of the Bragg law showing how an incident wave of wavelength λ is diffracted from a family of diffraction planes, highlighted in blue. The path difference between the wave scattered from two consecutive planes is given by Δ and coloured red.

The only difference is that the effect is dramatically enhanced when the scattering points are around the same size as the wavelength being used. In condensed matter physics, the interest is in the structure of solid materials where the scattering points are the electron clouds of individual atoms. Almost all solids, from metals to ceramics, have a characteristic lattice periodicity on the order of an angstrom, making x-ray light the ideal probe. It is for this reason that XRD is so ubiquitous in this field.

In-house x-rays are produced in an x-ray *tube*, an apparatus, under vacuum, consisting of a cathode and an anode. The cathode is heated until electrons are ejected from it, then the electrons are accelerated in a high voltage up to the anode, whereupon they emit a spectrum of x-ray radiation in the high energy collision.

For some measurements, an in-house x-ray diffractometer is sufficient. The majority of the XRD undertaken as part of this thesis was recorded on a Philips X'Pert PANalytical Material Research Diffractometer. The x-ray source is a copper anode and the x-ray radiation is selected by a monochromatiser to correspond to the $K_{\alpha 1}$ core transition, $\lambda = 1.5406$ Å. In many instances, however, it is advantageous to perform XRD using a synchrotron light source, that is, x-rays that have been generated by electrons in a particle accelerator. In Chapter 6, synchrotron XRD is used for the high beam intensity it provides. In Section 5.2.3, the need to tune the photon energy arises in order to perform XRD in resonance and this is an ability only synchrotron light sources have.

A highly versatile tool with a huge range of applications, XRD is used for everything from checking the purity of a new sample to identifying structural phase transitions. In this work alone XRD is employed in numerous ways.

Finite Size Oscillations

As mentioned earlier, when the scattering array can be considered infinitely large in all dimensions, the diffraction pattern manifests as a discrete spectrum of peaks. As discussed in Chapter 3, reduced dimensionality and the existence of the boundaries give rise to *finite size effects* in thin films. In XRD, this means that the diffraction pattern is the Fourier transform of the "infinite" crystal convolved with the Fourier transform of a rectangular function representing the thin film bound at the top and the bottom interface. This gives a pattern of peaks modulated by oscillations that are described by a sine cardinal function. The effect is most pronounced when the scattering vector, denoted Q and equal to the difference between the outgoing and incoming wavevectors, is normal to the substrate-film interface. A scan holding the Q vector in this direction and only changing the length of it requires that the angle between the incoming wavevector and the sample is kept equal to the angle between the outgoing wavevector and the diffraction plane. This geometry of coupled scan is called a symmetric, θ-2θ or Bragg-Brentano scan [91].

Fig. 5.6 a) illustrates schematically how the Q vector is varied during a symmetric scan. In panel b) is the output of such a measurement, here showing how the thickness of the thin film sample changes the pattern of finite size oscillations. It is possible to simply count the number of oscillations to obtain the number of unit cells of the film directly. It should be noted, however, that the measurements shown in Fig. 5.6 were obtained using synchrotron light. In-house, x-ray tube-based diffractometers are unlikely to allow measurement of the oscillations furthest from the Bragg conditions, the intensity is simply too low. The good news is that even if not all the oscillations are visible, the effect is straightforward to simulate numerically and the film thickness can be extracted from a computational fit to the data.

For thin film scientists, particularly those who do not have the option of *in-situ* monitoring, one of the crucial uses of XRD is the determination of the film thickness in this manner.

More generally, the presence of finite size oscillations indicates a high crystalline coherence between the individual unit cell layers of a thin film and so is a measure of sample quality.

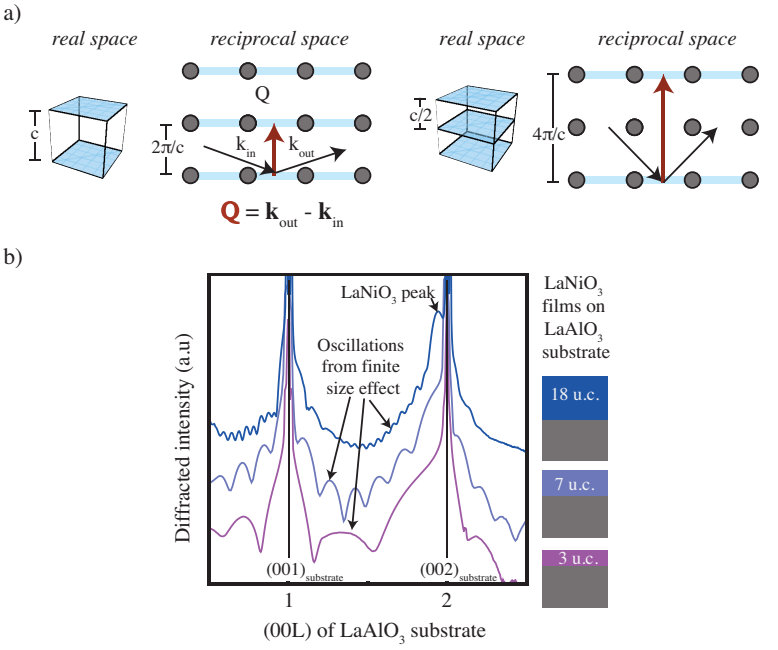

Figure 5.6: a) Schematic of how a symmetric scan (k_{in} coupled with k_{out}) works to probe the family of diffraction planes normal to the scattering vector, Q, the difference between the incoming and outgoing wavevectors. b) Some example symmetric scans along the specular direction of thin films of $LaNiO_3$ on (001)-oriented $LaAlO_3$ substrate. Visible are the sharp (001) and (002) peaks of the substrate and the corresponding peaks of the film, more rounded due to the lower scattering volume. Finally, between the specular peaks are the oscillations produced from diffraction through a sample of finite size in the direction of the Q vector. Each oscillation counts one unit cell of the thin film. The scans have been shifted vertically for clarity.

Scherrer Formula

The width of the diffracted peak carries information about the coherence of the array of scattering points. From the FWHM it is possible to calculate the thickness of the sample that the Q vector is probing. This can be a way to determine if the coherence length ($l_{coherence}$) contributing to a given Bragg peak is equal to the size of the sample or not. For differentiated structures this may not always be the case. The coherence length is given by the Scherrer formula:

$$l_{coherence} = \frac{180^o}{\pi} \frac{\lambda}{cos\theta_B} \frac{1}{FWHM(^o)} = \frac{c}{FWHM(r.l.u)} \tag{5.1}$$

where λ is the wavelength of the x-ray beam, θ_B is the Bragg angle being measured and FWHM(°) is the full width at half maximum of the diffracted peak in degrees. In reciprocal space, the real space coherence length is simply the ratio of the real space unit cell to the FWHM in reciprocal lattice units relative to that unit cell.

Because peak broadening can have other origins than the (de)coherence of the sample, for example the intrinsic instrument line broadening, the Scherrer formula determines a lower bound for the coherence length and the effective $l_{coherence}$ will be slightly larger.

Rocking Curve Analysis

While in the Bragg condition, the sample can be *rocked* around an axis normal to the measurement axis. Fig. 5.7 shows how the width of the resulting rocking curve (RC) peak gives information on the texture of the given diffraction plane. Higher texturing may be due to mosaicity, granularity, dislocations or inhomogeneities but does generally indicate a sample of lesser quality. In thin film science, it is instructive to check that the film has not picked up any extra texture compared to the substrate. For this, it is useful to simply measure the FWHM of the RC of the substrate and verify that the FWHM of the film is similar. For perfectly epitaxial growth, the FWHM of the substrate and the film should be very close.

Half-Integer Bragg Analysis

As mentioned in Chapter 2, perovskites have a pseudocubic unit cell that can be described simply as an octahedral cage of oxygens. This convenient representation allows us to visualise the entire structure as a network of corner sharing O_6 octahedra. XRD can be used to probe the structural distortions in such a network. This approach requires a greater deal of experimental and numerical effort compared to the XRD analyses described previously and the entirety of Chapter 6 is devoted to this study.

5.2.3 Resonant Soft X-Ray Diffraction

Solid materials try to minimise their total energy by finding a regular way to order the atoms, this *structural* ordering is what is probed in the standard, non-resonant, XRD described above. In many materials, however, there exists ordering beyond simply structural. The atomic orbital configuration, ionisation state and magnetic spin can all be modulated throughout the crystal lattice with a unit cell the same size as, or greater than, the chemical unit cell. These effects

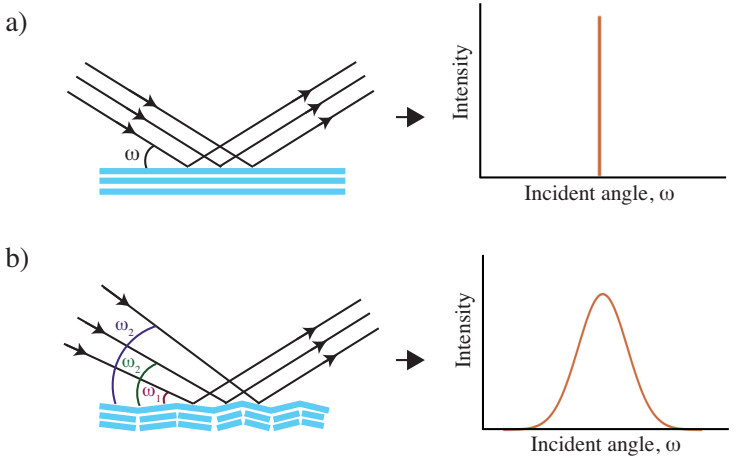

Figure 5.7: Illustration of the resulting rocking curve (RC) scan for different sample granularities. In a) the diffraction planes are angled "coherently" and so the Bragg diffraction condition is met only for one incident angle, ω, and a very sharp RC peak is obtained. In b) the sample has a certain granularity and the same diffraction condition can be met for a range of incident angles, giving a normal distribution across a spread of ω; ω_1 to ω_3.

and, in fact, all physical phenomena in any material, are dictated by the valence electrons. In standard XRD, the photons interact with the entire electron cloud of the atoms, to which the valence electrons contribute negligibly. If we wish to access information on these more exotic orderings, we must find a way of being sensitive only to the valence states. This can be done by selecting an incident photon energy that is resonant with an atomic transition up to the valence level. In 3d materials such as the nickelates, this corresponds to a transition to the d orbitals in the Ni on the order of hundreds of eV, rather low energy for x-rays hence the *soft* part of the name resonant soft x-ray diffraction (RESOXS) [92].

At these low energies, a large fraction of the x-ray beam is absorbed by the K edges of oxygen and nitrogen meaning that RESOXS experiments must be carried out in ultra high vacuum conditions. An additional complication of low energy x-ray scattering is that the Bragg angle for a given reflection is much larger meaning that the accessible range of Bragg reflections is very small. Nonetheless, RESOXS is frequently successfully employed to detect orbital, spin or charge ordering and to follow the order as a function of, e.g., temperature. It is precisely this technique that has been used to determine the Néel transition temperature in rare earth nickelate perovskite heterostructures [51].

In the antiferromagnetic (AF) phase, the magnetic ordering is directed

along the $[111]_{pc}$ crystallographic vector with a periodicity of four nickel layers. The AF state is therefore characterised by the $(\frac{1}{4},\frac{1}{4},\frac{1}{4})_{pc}$ wavevector. The $(\frac{1}{4},\frac{1}{4},\frac{1}{4})_{pc}$ Bragg peak is strongly resonant when the photon energy is tuned to the nickel-$L_{3,2}$ or rare earth-M transitions, confirming that the *R*NiO_3 lattice is the origin of the signal. In order to prove the magnetic nature of the peak, the incoming beam was linearly polarised and the dichroism, that is the difference in scattered signal between the horizontal (π) and vertical (σ) polarisations has been determined. For a peak of magnetic origin, the scattering amplitude should be greater if the light is polarised vertically and this is precisely what is found for the *R*NiO_3 compounds [93].

Depending upon the geometry of the diffractometer and the photon energy, when the films are grown in the conventional $(001)_{pc}$ direction (the axes are shown in Fig. 4.3), the $(\frac{1}{4},\frac{1}{4},\frac{1}{4})_{pc}$ reflection may be difficult to access. By mounting the (001)-film (where the [100] and [010] vectors are parallel to the sample edges) on a wedge inclined at 55° and then rotating the sample in plane by 45°, the [111] vector has essentially been aligned such that it lies in the plane of incidence of the experiment. This allows the measurement to be carried out in a straightforward specular geometry. A schematic of this is shown in Fig. 5.8.

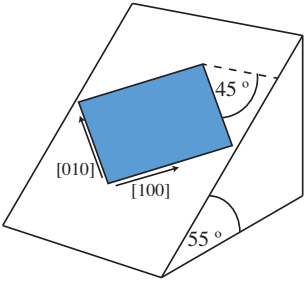

Figure 5.8: Schematic of the mounting of $(001)_{pc}$-oriented samples for RESOXS measurement of the $(\frac{1}{4},\frac{1}{4},\frac{1}{4})_{pc}$ Bragg peak.

On the other hand, if the films are grown in the (111) crystallographic orientation then the magnetic ordering vector is already parallel to the surface normal and there are no particular mounting requirements.

RESOXS has been used successfully for studying the AF ordering in *R*NiO_3 thin films oriented both in the (001) and the (111) directions [51, 53].

In this thesis, the technique was employed to verify the magnetic state of a thin film of $LaNiO_3$. No diffracted intensity was found at the $(\frac{1}{4},\frac{1}{4},\frac{1}{4})_{pc}$ Bragg condition, indicating that this sample of $LaNiO_3$ is not antiferromagnetically ordered in the same way as the other members of the *R*NiO_3 family.

5.2.4 DC Electronic Transport vs Temperature

To measure the DC electrical resistivity of a given material we need only to pass a current through it and measure the electric field produced (or vice versa). Straightforward measurements of the resistivity as a function of temperature (ρ(T)) can provide a wealth of information about the material. At first glance, the tendency of ρ(T) indicates the nature of the material, either metal (positive slope), insulator or semiconductor (negative slope) or superconductor (zero resistivity) [94]. Then, transitions between regimes are easily distinguished such as at the critical temperature for superconductivity or the well-documented metal-insulator transition in nickelates. Further, non-electronic transitions such as magnetic or structural transitions can also have a signature in the ρ(T), most often a kink or a change of slope. For a more detailed understanding of the underlying scattering mechanisms, however, it is usually necessary to attempt to fit a function to the ρ(T). This function generally takes the form of a sum of power laws plus the residual resistivity term ρ_0, meaning that the temperature dependence of resistivity is only the sum of the contributions of the various scattering channels particular to the material, which themselves are temperature dependent [95]. For instance, the famous T^2 dependence from Fermi liquid theory describing inter-electronic interactions, the T^5 of high temperature phonon-scattering and the linear temperature dependence (T^1) indicating proximity to a quantum critical point.

Fitting ρ(T) curves, therefore, sheds light on the microscopic physical mechanisms of the sample and these measurements have the added benefit of being relatively accessible.

In this thesis the majority of the ρ(T) measurements were performed in a ^{4}He dipping station. This consists simply of a dewar of liquid helium into which the sample rod (a small canister containing the sample plus a thermocouple) is progressively lowered (to decrease the temperature) and raised (to increase the temperature). This allows measurement, albeit without direct feedback on the temperature control, down to 4.2 K.

5.2.5 Magnetotransport

Resistivity as a function of applied magnetic field, the magnetoresistivity, can be used complementary to standard ρ(T) curves to uncover more details about the microscopic behaviour of a material. This measurement can either be performed with the magnetic field aligned normal to or parallel to the plane of the sample, constituting either *out-of-plane* or *in-plane* magnetotransport, and angle-dependent measurements that go between the two extremes are also routinely performed. For a normal metal, the magnetoresistivity is positive. Sometimes, however, a negative magnetoresistivity is found at low temperatures, often indicative of weak localisation.

As magnetotransport measurements require reliable temperature control

during the field sweeps, the ^{4}He dipping station used for standard ρ(T) measurements is unsuitable. For these, one of two dilution refrigerators was used, capable of reaching temperatures of tens of mK and magnetic fields of up to 8.5 T or 14.7 T, depending on the system.

5.2.6 Hall Effect

The final configuration of transport measurement described here is that of the Hall effect. As for *out-of-plane* magnetotransport measurements, the magnetic field is applied normal to the plane of the sample. Unlike the set-ups mentioned previously, however, the Hall resistivity is measured transverse to the current and is caused by the charge carriers reacting to the Lorentz force from the field. From the Hall effect, an estimate of the 2-dimensional density of mobile charge carriers can be extracted by eq. 5.2, which shows that the 2-D carrier density, n_{2D} is given by the slope of the Hall resistance, R_{xy} as a function of applied magnetic field, B.

$$n_{2D} = -\frac{B}{R_{xy}e} \tag{5.2}$$

Hall effect measurements in this work were performed in the dilution refrigerators described in the previous subsection.

5.2.7 Photolithographic Patterning

Having described the most common types of transport measurements it is clear that much can be learned from the global transport behaviour, there is, however, great benefit in knowing the absolute value of the resistivity with a high precision. This can be done through the van der Pauw method (see Ref. [96]) or with an accurate measure of the sample geometry. It is one option to bond wires directly to the thin film sample and measure the distances between them. A more reliable approach, however, is to actively define the sample geometry by photolithographic patterning. All the transport measurements reported in this work were performed on samples etched into a 100 x 680 μm Hall bar and contacted via aluminium wire bonded to sputtered platinum pads. The photolithographic process involved in making such patterns is briefly outlined in Fig. 5.9.

5.2.8 Raman Spectroscopy

Raman spectroscopy is another example of a *"photon in - photon out"* technique where the photons are scattered by the sample atoms. Almost all the scattered light is elastic in nature and falls into the category of Rayleigh scattering, this corresponds to the excitation of the atomic energy of the sample up to a virtual

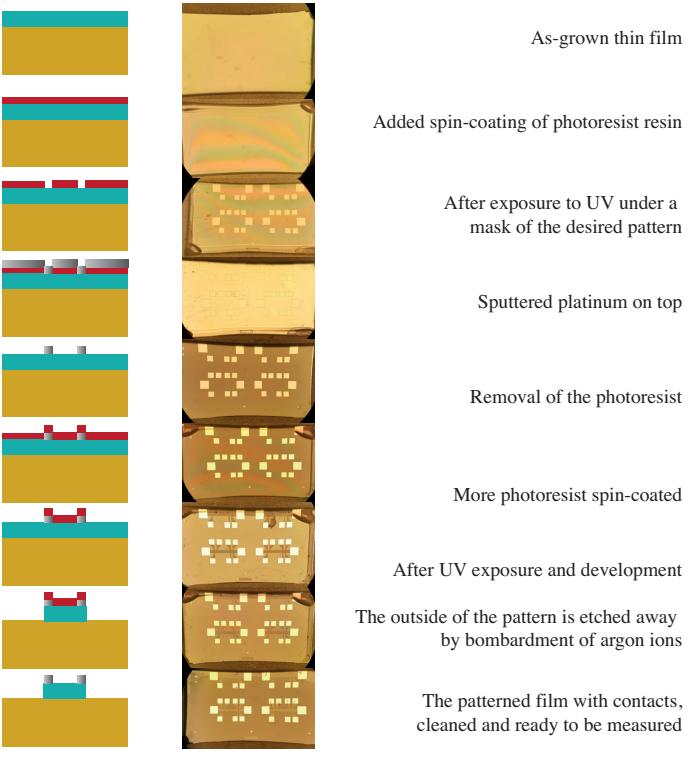

Figure 5.9: The process of photolithographically patterning a thin film sample. On the left, the cross section and in the middle a top-view microscope photograph.

state and back down into the initial state. Much more interesting is the very small fraction of the scattered signal that is inelastic and corresponds to the excitation up to a virtual energy state and back down to an excited state different to the initial one, or *vice versa*. This is the Raman scattering signal and it carries information about the various excitations available to the atoms [97, 98].

The Raman intensity is usually plotted as a function of the energy change $E_{out} - E_{in}$ called the *Raman shift* and expressed as a wavenumber or a frequency. Because it is thermodynamically less probable that the system is initially in an excited state, this means a higher intensity for negative Raman, or Stokes, shifts. All the Raman spectra in this work (Chapters 7 and 8) are plotted on a positive Raman shift axis but this is done for presentation purposes; almost all Raman spectroscopy measurements, in general, are on the Stokes, photon energy loss, side of the spectrum. Of course the Stokes and anti-Stokes

(positive Raman shift) signals are symmetrical so the reason for this inversion is simply to gain intensity.

A simplified visual of the mechanism of Raman scattering and an example spectrum are shown in Fig. 5.10.

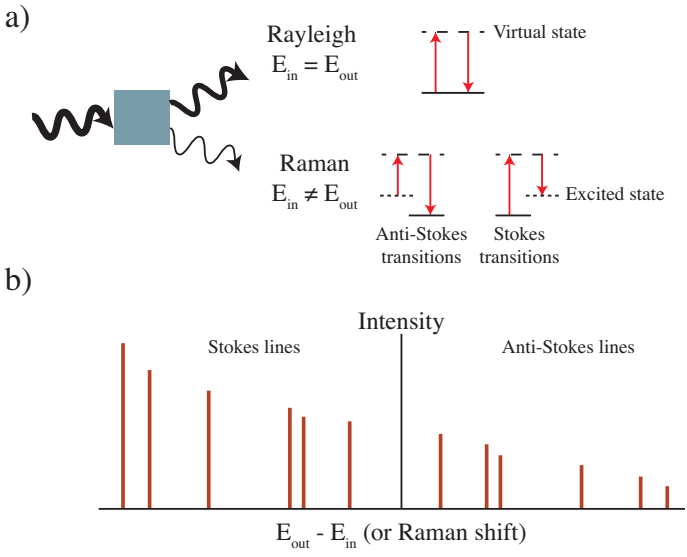

Figure 5.10: a) Simplified schematic of the difference between Rayleigh and Raman scattering. b) An example of a possible Raman spectrum, omitting the very strong Rayleigh intensity at zero Raman shift and including both Stokes and anti-Stokes scattering signal.

The Raman spectrum is unique for any given material and the number of peaks corresponds to the number of Raman active modes in the sample. Typically, the lower the symmetry of the material, the more Raman active modes are available. Raman active modes can take the form of structural, electronic or even magnetic excitations. For perovskite oxides, Raman spectroscopy is primarily used to probe the vibrational excitations, in other words the phonons of the system [99, 100]. This readily gives information on the structural symmetry, phase transitions, and, with a little extra work, on more subtle structural detail.

The application of Raman spectroscopy to thin films brings forth challenges not present in bulk studies. In addition to the familiar problem of reduced scattering volume from thin films, there is the issue of signal dominance from the substrate. Since the measured spectrum will be the sum of the (small) thin film signal and the (much larger) substrate signal, it is prudent to select a film/substrate combination such as to reduce as much as possible the overlap

of the Raman peaks. Unfortunately very many of the commonly used substrates are low symmetry, such as $NdGaO_3$, and so generate a vast number of Raman peaks spanning a large range of frequencies, rendering deconvolution of the thin film signal extremely difficult. Despite these limitations, however, Raman spectroscopy on thin films has become a well-established field [101].

Depth-profiled Raman spectroscopy coupled with a sophisticated principal component analysis has recently allowed the Raman spectrum for a $LaNiO_3$ film of only 1nm thickness to be obtained. This result, as well as a thickness-dependent study on these films and further details on the measurements, will be presented in Chapter 7. Further on, in Chapter 8, Raman spectroscopy proves an extremely effective tool to probe the structural phase transition when working with the solid solution $Nd_{1-x}La_xNiO_3$.

The Raman spectroscopy measurements that make up part of this work were carried out at the Luxembourg Institute of Science and Technology on a Renishaw inVia Reflex Raman Microscope using a He-Ne light source.

5.2.9 Scanning Transmission Electron Microscopy

One of the most powerful measurement techniques available to solid state physicists is electron microscopy. The resolution achievable by a microscope is dependent upon the wavelength of the probe. For visible light microscopes, this gives a resolution limit of not much less than a micrometer. Using the wave-like property of matter, however, can decrease this limit immensely.

In a scanning transmission electron microscope (STEM), a beam of highly focussed electrons is shone through a sample and the transmitted beam is collected by a detector on the other side. The sample must be cut, polished and etched down to a very thin slice in order for the beam to be transmitted sufficiently. The *scanning* part of the name comes from the feature that the beam can be moved over the sample to generate a raster image. Nowadays STEM resolution can be as low as tens of picometers. In other words, atoms themselves are visible.

STEM is a sophisticated and very powerful technique that has been employed to image even light elements such as the oxygen in transition metal oxides [19]. Despite being limited in throughput by the extensive sample preparation times, this technique allows an unprecedented insight into the atomic-scale physics of materials.

For Chapter 7 STEM measurements were carried out at the Université Paris-Sud and the technique proves invaluable in shedding light onto what happens in $LaNiO_3$ ultrathin films.

Chapter 6

Quantifying Octahedral Distortions in Perovskites

6.1 The Importance of Structure

The principal role of the structure in determining the physical properties of transition metal oxides is widely appreciated. In nickelates, the electronic and magnetic properties exhibit a particularly clear lattice dependence. The nickelate phase diagram itself is almost always shown with the x-axis representing the structural distortion in one way or another, for example, the Ni-O-Ni bond angle that dictates the orbital overlap. See Fig. 2.5 for a reminder of this mechanism.

Determination of the structure is where challenges may arise, especially for thin film systems due to low scattering volume and other effects outlined in Chapter 3. The present chapter describes a methodology for obtaining detailed structural information, about perovskites specifically, while making few assumptions.

6.2 Octahedral Distortions

In Chapter 2 the idea of simplifying perovskites to a network of corner-sharing octahedra was introduced as well as Glazer notation, the shorthand commonly employed to describe such systems. In his original work, Glazer suggested a way to determine the symmetry of perovskites by checking for the presence (or absence) of half-integer Bragg peaks in x-ray diffraction (XRD) [3]. These half-integer (HI) peaks, so-called because they appear, in reciprocal space, half-way between the integer diffraction peaks arising from the pseudocubic unit cell, correspond to a doubling of the unit cell in real space. The way in which the

unit cell is doubled, that is, by which Glazer rotation system, causes different peaks to be allowed or forbidden. The array of allowed HI peaks can be reasoned by symmetry, following the recipe presented by Glazer, or it can be predicted by directly calculating the diffraction pattern from a given structure. For this study it was first necessary to be able to generate the atomic positions from the input parameters of the Glazer rotation system and Glazer rotation magnitudes, requiring some 3-dimensional geometry.

6.3 Geometric Considerations

The main assumption made in this procedure is that the octahedra are perfectly rigid, although, in reality, some degree of bond length distortion is expected. Fig. 2.2a) shows the definition of the rotation angles α, β and γ where, because we are considering the rotation of a rigid body, it is important that these angles are taken with respect to the internal symmetry axes of the octahedron and not to the original, unrotated Cartesian axes. Fig. 6.1 illustrates how the axes are defined for an order of operation of the Glazer angles $\alpha \rightarrow \beta \rightarrow \gamma$.

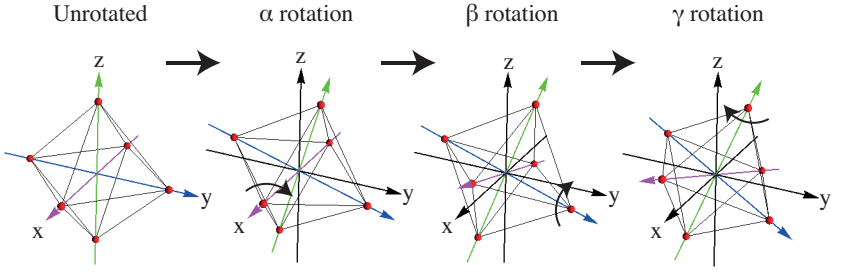

Figure 6.1: Schematic to show how the axes of rotation are defined with respect to the unrotated Cartesian axes (in black). α rotations are around what started as the Cartesian x-axis (magenta), β and γ rotations are around the former y-axis (blue) and z-axis (green) respectively but have now been rotated by the previous operations. After each partial rotation the axes are redefined.

A second geometric subtlety is that the group of 3-dimensional rotations, SO(3), is non-Abelian, meaning that the order in which the rotations are applied will change the final atomic positions. We find, for small angles of distortion, less than 10 °, the variation between the final vectors is minimal and the rotations could be performed in any order for a very similar result. When the rotation magnitude exceeds 10 °, however, the final positions begin to diverge heavily with a change in the order of operation. A way to get around this issue is to break the large rotation angle operation into several small rotation angle operations.

The operation is performed by the Rodrigues formula (from [102]):

$$\begin{pmatrix} cos\varphi + u_x^2(1-cos\varphi) & u_y u_x(1-cos\varphi) - u_z sin\varphi & u_z u_x(1-cos\varphi) + u_y sin\varphi \\ u_x u_y(1-cos\varphi) + u_z sin\varphi & cos\varphi + u_y^2(1-cos\varphi) & u_z u_y(1-cos\varphi) - u_x sin\varphi \\ u_x u_z(1-cos\varphi) - u_y sin\varphi & u_y u_z(1-cos\varphi) + u_x sin\varphi & cos\varphi + u_z^2(1-cos\varphi) \end{pmatrix}$$

which is applied iteratively around the three internal axes of octahedral symmetry in turn, each time by an increment of the total rotation angle for that axis. The m^{th} incremental rotation, φ, is performed around a unique vector $(u_x, u_y, u_z)_m$, which has been defined by successive application of all the m-1 rotation operations before. To obtain a final set of vectors that is independent of the order of operation, 50 iterations of the Rodrigues formula around each axis is found to be sufficient for a convergence within 0.1 % when the Glazer rotation magnitudes are very large (more than 15 °, meaning a very distorted perovskite). Fig. 6.2 shows how the resulting atomic positions, which depend upon the order of operation, converge to the same vector coordinates when the number of iterations increases.

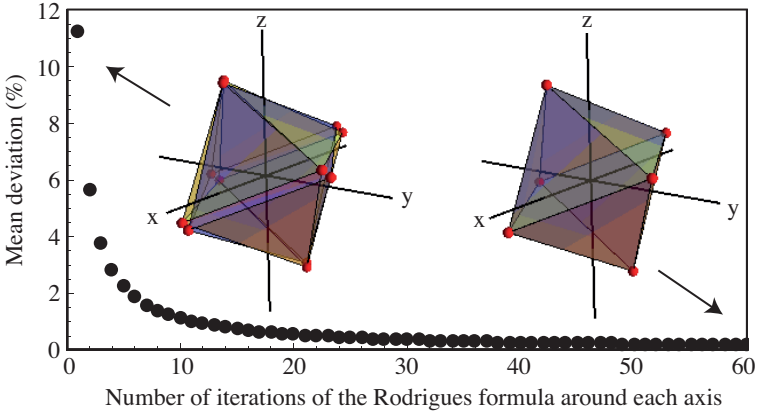

Figure 6.2: The percentage mean difference between resulting atomic positions calculated with the rotations applied in the order $\alpha \rightarrow \beta \rightarrow \gamma$ compared to in the order $\gamma \rightarrow \beta \rightarrow \alpha$. The insets are the graphical outputs of the simulation when the angles are applied in their entirety (one iteration) and when there are 60 iterations, each time by $\frac{\alpha}{60}$, $\frac{\beta}{60}$ and $\frac{\gamma}{60}$. The angles input for this test were very large; $\alpha = \beta = 16$ ° and $\gamma = 17$ °.

The process just described generates the positions of the corners of a rotated octahedron, in other words; the oxygen atomic sites, for a given set of input angles α, β, γ. Scaling up to the full unit cell requires another seven octahedra to be generated (to account for the doubling of the unit cell in three dimensions) with the same rotation magnitudes α, β and γ but with one or more of the rotations being negative, according to the Glazer system of interest. The

final result is a full reduced-symmetry unit cell consisting of 24 oxygen atoms, the positions of which can be used to simulate the HI diffraction intensity.

6.4 Simulating diffraction patterns

At a given Bragg vector (h, k, l), the intensity of the diffracted x-ray signal is calculated via the structure factor, F_{hkl}, given by:

$$F_{hkl} = f_{O^{2-}} \sum_{n=1}^{24} exp(2\pi i(hx_n + ky_n + lz_n)) \tag{6.1}$$

where the n^{th} oxygen atom is situated at the vector (x_n, y_n, z_n) in coordinates relative to the doubled unit cell. The prefactor $f_{O^{2-}}$ is the form factor for O^{2-} and represents the Fourier transform of the spatial electron density of that particular ion.

The final intensity is simply the square of the structure factor(s) along with some normalisation factors or corrections, if required. In the system of oxygen octahedral rotations, it is necessary to consider four separate structure factors. For rotation angles of (α, β, γ) there are three other sets of rotations that will give geometrically equivalent atomic positions, ($-\alpha$, β, γ), (α, $-\beta$, γ) and (α, β, $-\gamma$). Of course when probed with a Bragg vector (h, k, l) these domains are inequivalent and must be summed over to account for the four possible tilting configurations. The overall intensity is therefore:

$$I = \sum_{p=1}^{4} d_p [F_{hkl}]^2 \tag{6.2}$$

where the d_p are weighting factors that can be treated as further parameters in the fit to the experimental data.

Fig. 6.3 shows two examples of the output of simulating diffraction intensities on the plane $l = \frac{3}{2}$. To determine the Glazer rotation magnitudes it is necessary to compare these simulated intensities to those measured experimentally and find the best match. The *integer* Bragg peaks, that is, the ones measured in conventional XRD, do not arise from the simulation of only the oxygens so they do not appear in, for example, Fig. 6.3. In reality, however, the integer Bragg peaks are produced by the cation sub-lattice, which, in this simulation, does not undergo a doubling of the unit cell. For structures where there is some cation displacement expected along with the octahedral rotations, the cation position is another parameter to be optimised in the fit.

In order to achieve the best structural refinement, several HI Bragg peaks must be measured, both from unique families and within the same family to probe, for instance, the domain population fractions. Measurement of around ten HI Bragg peaks, of which six are unique (in the sense that they share no

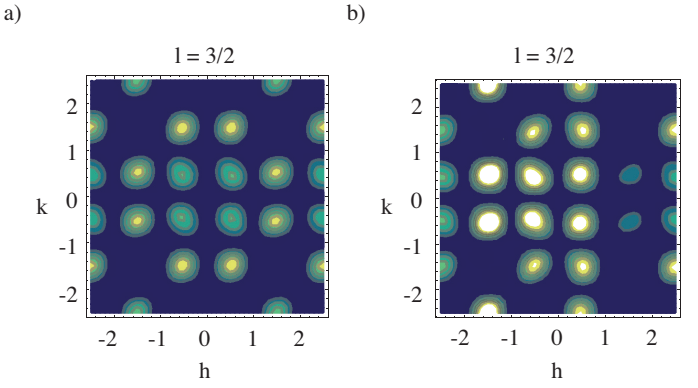

Figure 6.3: Simulated reciprocal space maps of diffraction intensity corresponding to the unit cell doubling due to distortions of the O_6 octahedra on the $l = \frac{3}{2}$ plane. a) Is for a system of $a^0b^-c^-$ where α = 0 º, β = 5 º and γ = 10 º and all the geometric domains are equally populated. b) Is for a system of $a^-a^-c^-$ where $\alpha = \beta$ = 5 º and γ = 10 º but only two of the four domains are populated (simulating a "twinned" structure).

in-plane symmetry between them), typically gives a sufficiently high reliability to the fit.

6.5 Measurement of Half-Integer Diffraction Peaks

HI diffraction peaks are typically several orders of magnitude lower in intensity than the integer ones. For low volume structures like thin films, usually the only way to access these reflections is by using high intensity synchrotron radiation.

All HI XRD measurements were performed at the Materials Science beamline X04SA, Surface Diffraction endstation at the Swiss Light Source, Paul Scherrer Institut in collaboration with Professor Willmott [103].

The samples were mounted on a hexapod in a 6-circle diffractometer allowing for a wide range of geometries. For these measurements the geometry was set to have a fixed incident angle of 4º. This is a wider angle than is typically used in surface diffraction but it was selected taking into consideration the sample size and beam footprint area to ensure that the beam never overspills the sample. It is essential that the sample volume being probed is independent of the diffraction peak being observed because the absolute value of the intensity is crucial for the analysis. Without this fixed geometry, the measured

intensities would need to be corrected, adding complexity to the treatment of the data.

The samples were measured at room temperature, under flowing helium (to minimise radiation damage to the sample) and at a photon energy between 13 keV and 15.5keV to avoid any absorption edges of the relevant elements.

Allowing efficient measurement is the 2-dimensional Pilatus-II pixel detector. The ability to capture the entire diffracted beam in one image means that alignment is quick and intuitive and the integration time can be cut to seconds.

Alignment is done with respect to the substrate lattice due to the higher intensity and the known structure and orientation. Then the measurements themselves take the form of crystal truncation rods (CTRs), XRD scans normal to the film surface. The CTRs are always expressed relative to the substrate reciprocal lattice, even if the substrate produces no HI Bragg peak at that point. Specular CTRs were recorded in order to extract the film thickness from the finite size oscillations (see Fig. 5.6 for an example) but all the other CTRs were off-specular and half-integer to access the doubled unit cell of the oxygen sublattice. The parameter of interest is the total intensity of a given reflection, found by integrating the signal. Two examples of the types of HI peaks measured are presented in Fig. 6.4. The function used to fit the data was of the form:

$$y = A\left[exp\left(\frac{-(x-B)^2}{2C^2}\right)\right] + Dx + E \tag{6.3}$$

with the first term a Gaussian function, the second term a linear slope offset and the third term a constant background. The final integrated intensity is given by the integral of the Gaussian part, $AC\sqrt{2\pi}$. Fig. 6.4 shows two HI diffraction peaks, one where the substrate contributes a diffraction signal and one where it does not. In both cases the Gaussian fit is straightforward to obtain and the integrated intensity can be extracted.

Once both the simulated and experimental intensities have been obtained they are normalised to the same (h,k,l), usually the one corresponding to the highest experimental intensity, giving two comparable sets. If the normalised simulated intensity for the n^{th} diffraction peak is $I_{sim}(h,k,l)_n$ and the normalised experimentally measured intensity for the n^{th} diffraction peak is $I_{exp}(h,k,l)_n$ then the residual sum of squares (RSS) is defined such that:

$$RSS = \sum_n |I_{sim}(h,k,l)_n - I_{exp}(h,k,l)_n|^2 \tag{6.4}$$

and, from this, the input parameters (α, β, γ and the d_p) can be varied until the RSS is minimised, determining the best fit structure.

The programming for the procedure outlined here was written on Wolfram Mathematica and is more advanced than the methods previously reported [76, 104, 105]. Here we have simulated the full 3-dimensional structure, taking

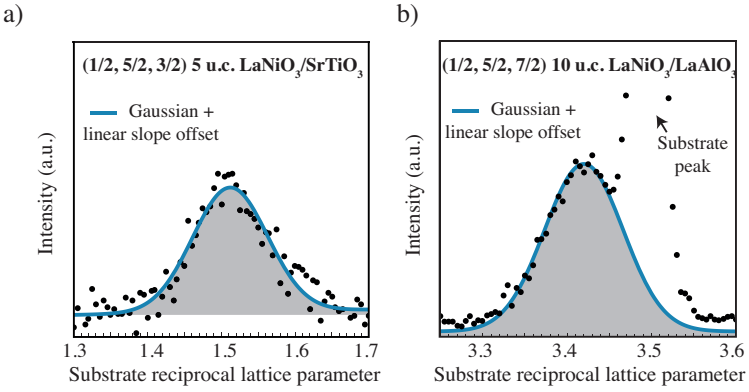

Figure 6.4: CTR scans of HI diffraction peaks showing the fit function used to calculate the integrated intensity for a) a 5 unit cell (u.c.) $LaNiO_3$ film on a substrate that has no room temperature octahedral rotations of its own ($SrTiO_3$) and for b) a 10 u.c. $LaNiO_3$ film on a substrate of the same rhombohedral symmetry as $LaNiO_3$ ($LaAlO_3$) but a different lattice parameter meaning that the two peaks are separated sufficiently to allow the film signal to be treated independently.

care with how the rotation operations are applied, whereas a simplification is to only consider rotations projected onto the initial Cartesian planes. This streamlines the computation but begins to be unreliable with larger ($> 10^o$) rotation angles, a problem not encountered here.

With all this we are now prepared to measure real thin film perovskite samples.

6.6 Application to Perovskite Films

Experiments in the theme of what is described in the previous sections have been undertaken on various perovskite systems. The HI Bragg peak approach has provided insight into, for instance, the structure of perovskite films grown on different substrates, highlighting how readily the oxygen octahedra rotate to accommodate biaxial strain [76, 104, 105] or a substrate-film symmetry mismatch [106]. More complex systems have been studied as well, such as superlattices of two alternating perovskites where, by playing with the length scales of interfacial structural coupling, a specific structure can be engineered [107]. Simulations that take into account cation displacements as well have also been developed [108]. More advanced analysis techniques based on phase retrieval also exist such as coherent Bragg rod analysis (CoBRA), which has been used to achieve layer-resolved structures in perovskites [109–114]. Studies com-

bining the half-integer Bragg technique with transmission electron microscopy show a good agreement between the two [115]. The interest in determining the octahedral rotations is also reflected by the growing appreciation of their importance from the theoretical side [116–120].

When a perovskite material is grown as a thin film, its structure largely reflects the imposed tetragonal distortion brought by the biaxial strain with the substrate. Adaptations to this new unit cell can take the form of bond length modifications, octahedral rotations or defect formation (see Fig. 3.2). Beyond this, as discussed in Chapter 3, the structure close to the surface and near the heterointerface with the substrate may look quite different to the rest of the film. This can be due to polar discontinuity, cation discontinuity, symmetry mismatch and so forth [15, 20, 121]. The contribution to the overall film from these boundary layer structures is small when the film is thick but as the film is made thinner, the relative influence of these layers increases. Due to this, it is reasonable to expect a quantitative change in structure with changing film thickness. To our knowledge, there have been no studies explicitly focussed on the thickness-dependence of the octahedral rotations determined by HI Bragg peaks. For the work reported here, the main interest was in pushing the thickness as low as possible.

6.6.1 $LaAlO_3/SrTiO_3$

The (001)-oriented $LaAlO_3/SrTiO_3$ system is famous for the 2-dimensional electron liquid, which is also superconducting, formed at the interface, despite $LaAlO_3$ and $SrTiO_3$ both being band insulators [22, 23]. Here, however, we are not concerned with the electronic properties as $LaAlO_3/SrTiO_3$ provides the ideal test system for the type of analysis described in this chapter.

At room temperature, $SrTiO_3$ is purely cubic and so there are no HI reflections. Bulk $LaAlO_3$, on the other hand, belongs to the space group $R\bar{3}c$ and exhibits Glazer rotations of $a^-a^-a^-$ with $\alpha = \beta = \gamma = 5.6^o$. This Glazer system produces every peak (h, k, l) where h, k and l are all half-integer except the reflections where $h = k = l$, which are symmetry forbidden. $SrTiO_3$ has a room temperature lattice parameter of 3.905 Å, which imposes a tensile strain on the $LaAlO_3$ (lattice parameter = 3.789 Å) of 3 %. Taking the strain into account, the expected Glazer system of a $LaAlO_3$ film on $SrTiO_3$ substrate would be $a^-a^-c^-$. It is also expected that γ is smaller than α and β due to the tensile strain and this is discussed later. Further simplicity is brought by the fact that the domain population fractions, d_p, should be equal with a cubic substrate.

The $LaAlO_3$ films were grown on (001)-oriented, TiO_2-terminated $SrTiO_3$ substrate by pulsed laser deposition, described briefly in Section 5.1. The samples were grown in a pressure of 8 x 10^{-5} mbar at a temperature of 800 °C and a laser repetition rate of 1 Hz. The films were then post-annealed in 200 mbar of oxygen at 530 °C for an hour. One film was grown with a thickness of 10 u.c. and the other with 5 u.c. After a standard sample characterisation

(see Section 5.2), the samples were then measured at the Swiss Light Source as described in the previous section.

The symmetry of the films was confirmed to be at least $a^-a^-c^-$ where the equivalence of the α and β was assumed due to the in-plane symmetry and then confirmed by comparing the intensities of peaks from different quadrants within the a-b plane. To find the rotation magnitudes it is necessary to proceed with the simulation described previously.

Fig. 6.5 shows the output of the simulation for a (001)-oriented $LaAlO_3$ film of 10 u.c. thickness grown on a $SrTiO_3$ substrate. Panels a) and b) are density plots of the sum of the squares of the differences between the measured and simulated intensities (RSS). Panel b) is calculated with a higher level of precision in the parameter space. Panels c) and d) show the input angles that give the lowest RSS values when the optimisation is repeated hundreds of times, each time with a random noise of $\pm$ 5 % (c) and $\pm$ 1 % (d). The optimised α, β and γ remain within the same range of values with the application of artificial experimental noise, indicating the robustness of the simulation to the input data. This is a known method of checking that a simulation is not overfitting [108]. Eq. 6.5 describes how, for each measured intensity I_{exp}, a new intensity I'_{exp} can be calculated. In this process, the parameter R_n is a randomly generated number between, for instance, -0.05 and $+0.05$ for a 5 % artificial error.

$$I'_{exp}(h,k,l)_n = I_{exp}(h,k,l)_n + R_n I_{exp}(h,k,l) \tag{6.5}$$

Over 350 repetitions give a mean of $\alpha = \beta = 6$ ° and $\gamma = 2.3$ ° (panel d)), which corresponds to the minimum RSS in the density plot (panel b)) and all the scattered values coming from the artificially-added experimental noise lie within the contour delineating 1 % of the minimum RSS. Therefore the mean of the scattered data is taken as the final result.

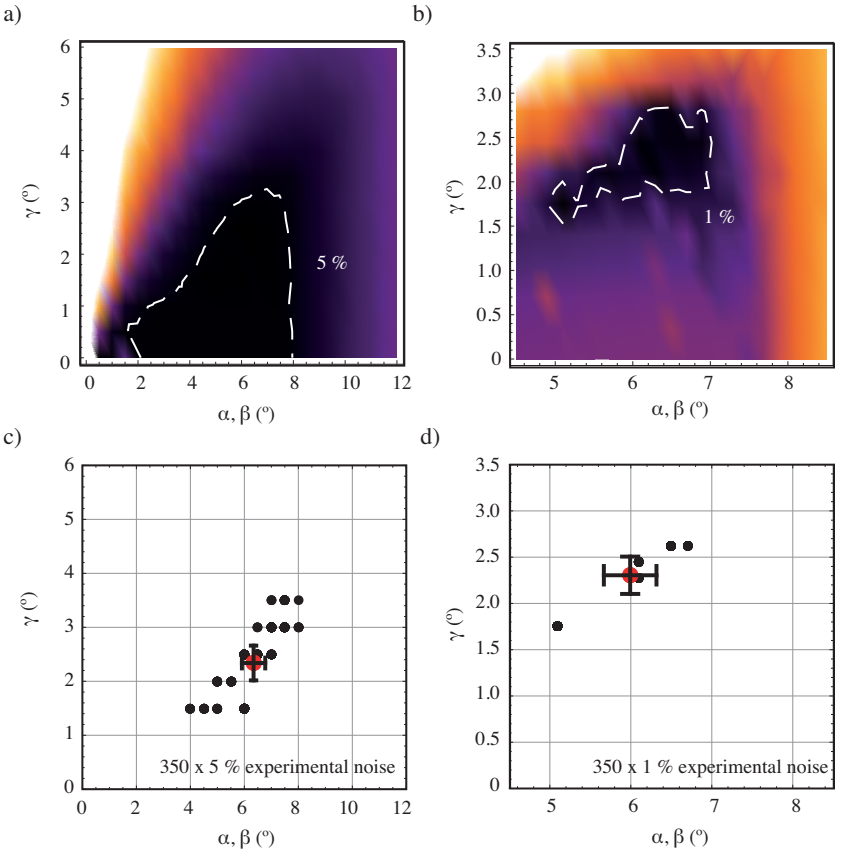

Figure 6.5: a) and b) are density plots in the parameter space of the input Glazer angles showing the RSS of the optimisation. The darker colour indicates a lower residual and, hence, a better fit. Shown by the dashed white line is the contour marking the values within 5 % (a) and 1 % (b) of the minimum RSS. c) and d) are scatter plots showing the values of α ($=\beta$) and γ that produce the lowest RSS, in other words the best fit, when the process is repeated 350 times with a random noise added to the experimental data that is within 5 % (c) and 1 % (d). The mean of the 350 runs (all the black points, many of which are superimposed) is shown by the red mark and the error bars correspond to the standard deviation on this mean.

With the same statistical analysis performed on the second sample, the results can be summarised as follows:

	α=β (°)	γ (°)
10 u.c. $LaAlO_3/SrTiO_3$	6.0 ± 0.8	2.3 ± 1.1
5 u.c. $LaAlO_3/SrTiO_3$	0.7 ± 1.0	0.2 ± 1.0

The Glazer angles determined for the 10 u.c. sample reflect the tetragonality of the tensile strain in that the out-of-plane tilts are greater in magnitude than the in-plane rotation, the latter of which is considerably reduced. The out-of-plane effect does not appear to be extreme, however, as the out-of-plane tilt magnitude, α (=β) is found to be 6 °, only slightly enhanced from the bulk 5.6 °. This may be due to the low thickness of the film and, as suggested by the results in the following section on the similar $LaNiO_3/SrTiO_3$ system, the pure tetragonality effect may not stabilise until the thickness exceeds around 12 - 15 u.c.. At only 5 u.c., however, the rotations are strongly suppressed both in-plane and out-of-plane. This is in concordance with a transmission electron microscopy study that finds the out-of-plane tilt, α (=β), to be around 5 ° for a 7 u.c. $LaAlO_3/SrTiO_3$ sample [122]. This distortion suppression may possibly be due to the proximity to the cubic $SrTiO_3$ substrate, an effect that will be discussed in the section to follow.

It should be noted that the signal on the HI Bragg peaks remains measurable, even when the film thickness is only 5 u.c. (2 nm). It seems likely that this does not yet represent a lower thickness limit for the feasibility of these measurements and so a more extensive thickness study can be carried out.

6.6.2 $LaNiO_3$ Thickness Dependence

A series of $LaNiO_3$ samples was grown by radio frequency off-axis magnetron sputtering at a temperature of 510 °C and in a 7:2 Ar:O_2 mix at a pressure of 0.24 mbar. For more details on the growth see Section 5.1. The (001)-oriented $LaAlO_3$ and TiO_2-terminated (001)-oriented $SrTiO_3$ substrates were both supplied by CrysTec GmbH. Structural parameters of the substrates as well as bulk $LaNiO_3$ are provided in the following table [123, 124].

Room temperature bulk structures	$LaNiO_3$	$LaAlO_3$	$SrTiO_3$
Pseudocubic lattice parameter (Å)	3.838	3.789	3.905
Space group	$R\bar{3}c$	$R\bar{3}c$	$Pm3m$
Glazer system	$a^-a^-a^-$	$a^-a^-a^-$	$a^0a^0a^0$
Octahedral rotation $\alpha = \beta = \gamma$ (°)	5.2	5.6	0

The samples are of high quality with atomically flat step-like topographies, as demonstrated by atomic force microscopy, enduring epitaxial coherence, as evidenced by transmission electron microscopy and a high degree of crystallinity, as seen in the XRD shown shortly as well as in Fig. 5.6. The results that follow were all obtained by the procedure described in this Chapter and are summarised in Fig. 6.6.

The film thicknesses and c-axis parameters were obtained by analysing the specular CTRs and the results are shown in Fig. 6.6a). Due to the compressive strain applied by the $LaAlO_3$ substrate (ϵ_{xx} = -1.3 %), the $LaNiO_3$ is expanded out-of-plane with respect to the bulk structure and the opposite effect is seen for the samples on $SrTiO_3$ - out-of-plane compression due to the tensile biaxial strain state (ϵ_{xx} = 1.7 %). There is a further, intriguing discrepancy between films on the two substrates; the c-axis parameter of $LaNiO_3$ depends strongly on the total film thickness when grown on $SrTiO_3$ but does not depend at all on total film thickness when grown on $LaAlO_3$. Possible reasons for this are discussed at the end of this chapter.

Fig. 6.6b) shows the coherence length as a function of total film thickness for all the samples in this study as calculated by the Scherrer formula (eq. 5.1). The interpretation of this quantity is the minimal thickness of the lattice structure that produces the diffraction peak in question, projected onto the probing (Q) vector, which, in the case of these CTR scans, is simply normal to the sample surface. If $l_{coherence}$ corresponds to the total film thickness, as determined by counting the fringes in the specular CTRs produced due to the finite size effect, this suggests that the films adhere to the same symmetry at all depths and there is no extra contribution coming from the substrate. This seems to be the case here except for the thinnest samples where the coherence length starts to exceed the film thickness, indicating that perhaps the topmost few unit cells of the substrate are influenced by the film above, an effect that has been observed in, for example, transmission electron microscopy on similar systems [19]. This implies that the unit cell doubling distortion propagates deeper into the substrate when the film is thinner and could possibly be due to the proximity to the film surface, where extreme structural distortions can manifest and may penetrate downwards.

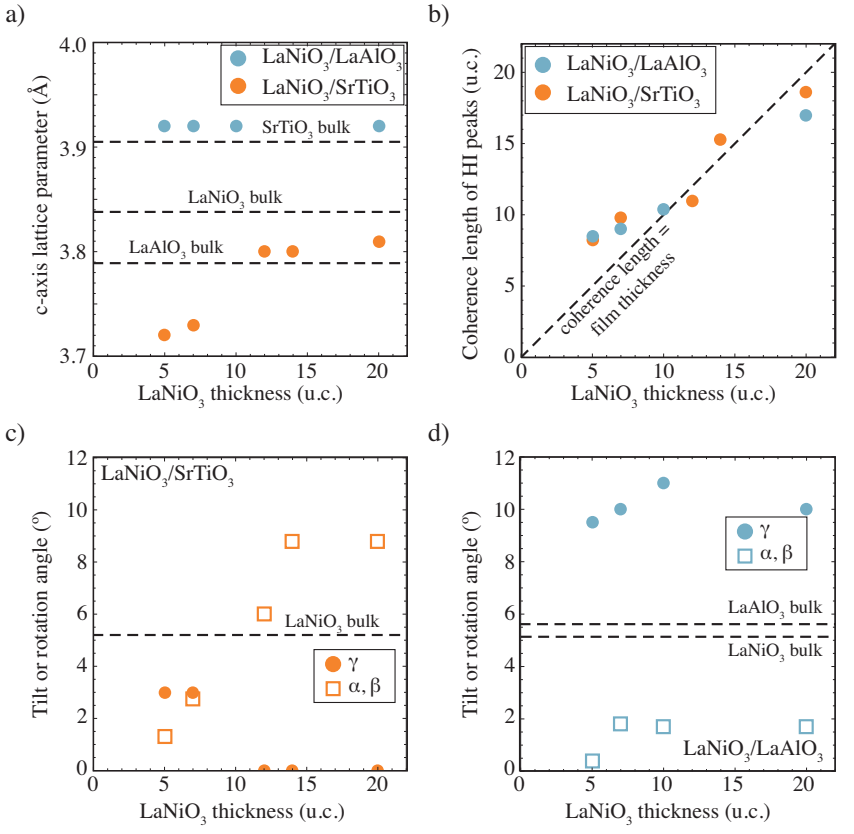

Figure 6.6: a) The c-axis lattice parameter as a function of $LaNiO_3$ film thickness on both $SrTiO_3$ (orange) and $LaAlO_3$ (blue). Bulk values for all materials are indicated by the dashed lines. b) The coherence length calculated from the Scherrer formula as a function of total film thickness for all samples on both substrates. The dashed line marks the points where the coherence length would be equal to the total film thickness. c) The tilt or rotation angle from the Glazer description as a function of total film thickness on $SrTiO_3$ substrate. d) The tilt or rotation angle from the Glazer description as a function of total film thickness on $LaAlO_3$ substrate. In c) and d) the bulk rotation angle for $LaNiO_3$ is denoted by the dashed line.

Panels c) and d) of Fig. 6.6 show the results of the optimisation to the experimental HI Bragg peak intensities by the simulation detailed in this chapter. Panel c) corresponds to the best fit angles ($\alpha = \beta$ and γ) for $LaNiO_3$ on $SrTiO_3$ substrate while panel d) shows the best fit angles for $LaNiO_3/LaAlO_3$. The squares represent the out-of-plane tilts, α and β whereas the circles in-

dicate the in-plane rotation magnitude γ. The data on $LaAlO_3$ substrate has little thickness dependence while the data on $SrTiO_3$ is more complex. Fig. 6.7 shows a visualisation of these results in the parameter space of the rotation magnitudes along with some schematics of the structures found.

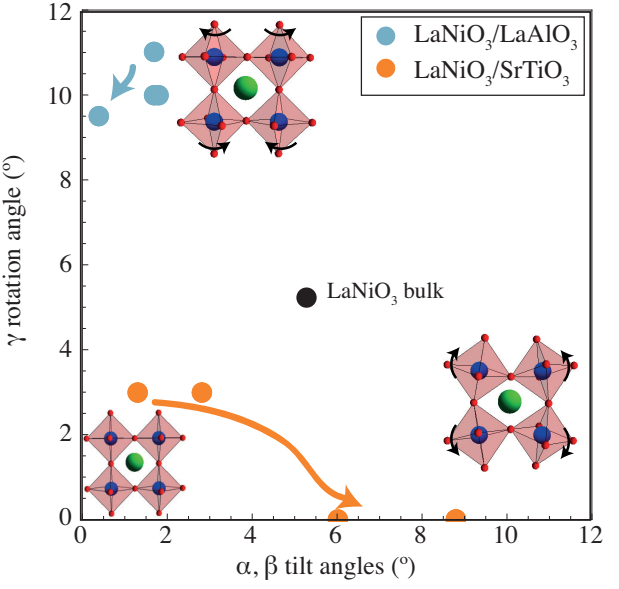

Figure 6.7: The best fit α, β and γ angles for all the samples investigated. The arrow directions indicate increasing film thickness of $LaNiO_3/SrTiO_3$ (orange) and $LaNiO_3/LaAlO_3$ (blue). The data is the same as Fig. 6.6 c) and d) but here plotted on the (α=β)-γ plane, mapping the parameter space.

For the thicker (> 14 u.c.) samples, the angles reflect what would be expected from only considering the effect of biaxial strain. On $SrTiO_3$, the strain is tensile so the $LaNiO_3$ oxygen octahedra would be expected to straighten their in-plane Ni-O bonds to maximise the in-plane space, this means a rotation around the c-axis and smaller γ of nearly 0°. The α and β, on the other hand, are much larger at almost 9°. The octahedra reduce their out-of-plane extension by increasing α and β to account for the tetragonal distortion stemming from tensile biaxial strain. This is schematised by the inset on the bottom right (high α and β but low γ) of Fig. 6.7. The opposite situation is observed for $LaNiO_3/LaAlO_3$, a compressive strain state. Here γ is forced to around 10° by in-plane restriction and the secondary result is that α and β decrease to accommodate the new tetragonal distortion that is longer out-of-plane than in-plane. At least until 40 u.c., the strain state of these films is retained, as evidenced by reciprocal space maps that show the in-plane lattice parameter

matching that of the substrate. These Glazer systems would therefore likely be found for continually increasing thickness until strain relaxation, where the bulk values would be preferred. Ref. [76] finds, for slightly thicker $LaNiO_3$ on both $LaAlO_3$ and $SrTiO_3$ substrates, Glazer angles that are in good agreement with what we see here. Theoretical calculations on $LaAlO_3$ films also reproduce these higher thickness, biaxially-strained structures and $LaNiO_3$ would be expected to be similar [105, 125]. It seems likely, therefore, that the modified octahedral network structures determined here for films that are thicker than 15 u.c. but still biaxially strained are preferential.

In the case of the films on $LaAlO_3$ substrate, the biaxial strained structure holds until as little as 5 u.c., similar to how the c-axis parameter appears to be independent of the total thickness, see Fig. 6.6a). By contrast, the octahedral rotations in films on $SrTiO_3$ depend much more strongly on the total thickness. In particular, as the thickness is decreased, the α and β tilts seem to be tending towards 0° which, it should be noted, is the room temperature rotation angle in the cubic $SrTiO_3$ substrate. It is therefore likely that the film structure is inclined to adopt the same out-of-plane rotations as the substrate through octahedral coupling at the heterointerface. The effect of the interfacial octahedral coupling reduces when the thickness approaches 12 - 15 u.c., the same length scale over which the c-axis parameter also changes on the $SrTiO_3$ substrate. The actual interfacial coupling length could be much less than 12 u.c., however, as it should be kept in mind that these measurements are sensitive to the entire film thickness and so give an average structure.

Notably, the angles obtained for 10 u.c. and 5 u.c. of (001)-oriented $LaAlO_3/SrTiO_3$ found in the previous subsection compare favourably with the thickness-dependence of $LaNiO_3/SrTiO_3$ here, suggesting that $LaAlO_3$ and $LaNiO_3$ react to the $SrTiO_3$ interface in a similar way. This is most likely as a result of their structural similarities in bulk (for instance, both are rhombohedral), as summarised in the table at the beginning of this part and also aids in the understanding of the $LaNiO_3/LaAlO_3$ interface.

In the $LaNiO_3/LaAlO_3$ system, the two materials are much closer in lattice parameter and the interface has, nominally, no polar discontinuity, no A-site discontinuity and no symmetry discontinuity so the $LaNiO_3$ can adopt a more stable, low energy, structure. In the $LaNiO_3/SrTiO_3$ system, however, there are many more discontinuities so it could be that the $LaNiO_3$ is more frustrated and has to respond to the interface in a more complex way; first by octahedral coupling and then by accommodating the biaxial strain. Although strain relaxation on the scale of the thicknesses measured here can be ruled out by reciprocal space maps, there is still the possibility that the $LaNiO_3/SrTiO_3$ interface has a higher propensity to develop point defects and this may be having an effect as well. Regardless of the origin, the smooth evolution of the thickness dependence of the octahedral rotations in the $LaNiO_3/SrTiO_3$ system may have an application in atomic-scale structural engineering through integration in a superlattice structure.

6.7 Summary

In this chapter, a simulation designed to give the Glazer rotation system and angle magnitudes through fitting half integer Bragg peaks in x-ray diffraction was described. The simulation was then used to obtain structural information on three thin film perovskite oxide systems; $LaAlO_3/SrTiO_3$, $LaNiO_3/SrTiO_3$ and $LaNiO_3/LaAlO_3$, all in $(001)_{pc}$ crystallographic orientation.

$LaNiO_3/LaAlO_3$ appears to be a system where the compatibility between the two components leads to a film structure that is independent of the total film thickness and the Glazer rotation angles reflect an almost pure biaxial strain effect.

$LaNiO_3/SrTiO_3$ and $LaAlO_3/SrTiO_3$ are very similar, owing to the corresponding similarity between bulk $LaNiO_3$ and $LaAlO_3$. In this thin film system, however, the stark differences between the ideal film structure and the substrate are such that the film appears to accommodate the heterointerface in a complex and thickness-dependent way; first by octahedral rotation to match the substrate and then, for thicker films, by octahedral rotation to fill the tetragonality imposed by biaxial strain.

The simulation developed and used here can be further applied to other perovskite oxide systems. It can be adapted to take into account cation displacements and so studies on $Pnma$-type perovskite thin films are foreseeable. More complex structures, such as multilayers and superlattices, can also be readily measured with such a technique and future work will go in this direction.

Chapter 7

Ultrathin $LaNiO_3$

7.1 Motivation

As the only rare earth nickelate that does not exhibit the rich phases and transitions of the rest of the family, $LaNiO_3$ has, in recent years, mainly been studied with the notion of high temperature superconductivity as the motivation. As discussed in Section 4.6, it was predicted that superlattices that alternate a metallic 1 u.c. layer of $LaNiO_3$ with a non-transition metal perovskite oxide band insulator may provide a welcome environment for superconductivity, analogous to the high temperature superconducting cuprates. Besides the likely issue that the electronic configuration of the nickelates is not as similar to the cuprates as it may first appear, there is also a challenge in understanding the behaviour of $LaNiO_3$ in the ultrathin limit.

7.2 Electronic Transport

Thin films of $(001)_{pc}$-oriented $LaNiO_3$ are metallic, in reflection of the bulk metallicity. They do, however, begin to show a resistivity upturn when thinner than 6 - 10 pseudocubic unit cells (u.c.) (2.3 nm - 3.8 nm) and become completely insulating when their thickness is further reduced to 3 - 6 u.c. (1.1 - 2.3 nm) [126–128]. The upturn regime at intermediate thicknesses has been ascribed to a weak localisation phenomenon, described in detail in [128]. The threshold thicknesses for the upturn and insulating regimes depend upon the substrate selected for epitaxial growth but are found to correspond to an equivalent sheet resistance; the crossover to the insulating phase happening at $R_s = \frac{h}{e^2} \approx 25\ k\Omega$, the 2-dimensional quantum of resistance. At around the same thicknesses, a dramatic change in the Fermi surface is observed by angle-resolved photoemission spectroscopy, indicating that these *ultrathin* films of $LaNiO_3$ are physically distinct from their thicker counterparts [129, 130].

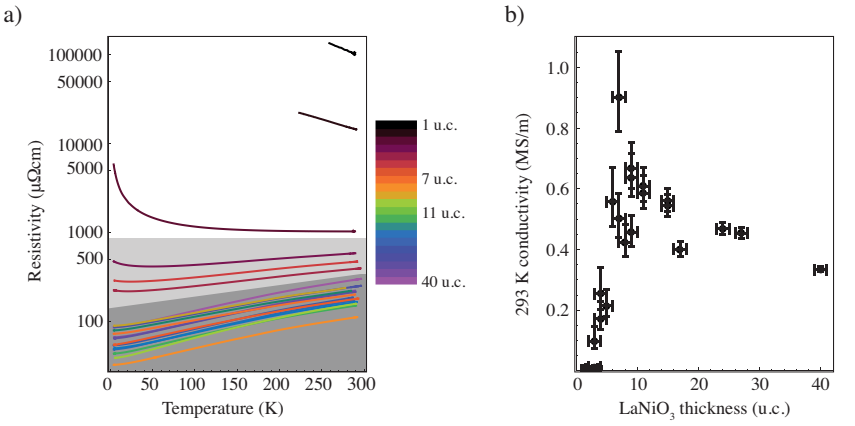

Figure 7.1: a) ρ(T) curves of (001)-oriented $LaNiO_3/LaAlO_3$ thin films of varying thicknesses. The thickness is indicated by the colour code. Three regimes of behaviour are highlighted. b) The room temperature conductivity of the same samples as panel a) plotted as a function of total film thickness. Published in [131].

Fig. 7.1 shows in a) a collection of ρ(T) curves for different thicknesses of $LaNiO_3$ grown on $(001)_{pc}$-oriented $LaAlO_3$. The three regimes of behaviour; metallic, upturned and insulating, are shown by the grey parts. For the metallic films, we observed that the most conducting films belong to an intermediate thickness regime, 6 u.c. - 11 u.c.. The least resistive film has a 4 K resistivity of 32 $\mu\Omega cm$. In panel b) the room temperature conductivities of these films are plotted as a function of total $LaNiO_3$ thickness. The error bars correspond to the uncertainty of $\pm$ 1 u.c. in determining the thickness, which also contributes the greatest error in determining the resistivity. Even within the sample-to-sample scattering, there is a marked conductivity enhancement for film thicknesses from 6 - 11 u.c. (2.3 - 4.3 nm). This enhancement is also observed up to room temperature.

Similar, although less extensive, series were grown on $NdGaO_3$ and LSAT substrates, both $(001)_{pc}$-oriented. The ρ(T) characteristics are shown in Fig. 7.2. Between the $LaAlO_3$, $NdGaO_3$ and LSAT substrates it seems that only the series on $LaAlO_3$ shows the marked enhancement of conductivity for $LaNiO_3$ thicknesses between 6 - 11 u.c.

The metallic ρ(T) curves can be fitted at low temperature by an expression of the form $\rho(T) = \rho_0 + AT^n$. The exponent, n, is in the range 1.8 - 2.0, close to the well-known T^2 behaviour of Landau-Fermi liquid systems coming from the quadratic scattering rate [132]. The A coefficient of the T^2 term is proportional to the square of the effective mass, a quantity that describes how much *heavier* a charge carrier feels in response to interactions. In these $LaNiO_3$ thin films,

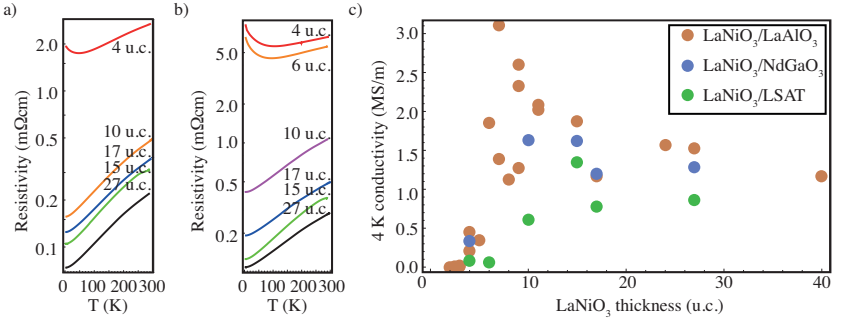

Figure 7.2: ρ(T) curves of $LaNiO_3/NdGaO_3$ films (a) and $LaNiO_3/LSAT$ films (b) of varying thicknesses. In c) is the 4 K conductivity plotted as a function of total film thickness taken from the ρ(T) curves of panels a) and b) and from the $LaNiO_3/LaAlO_3$ ρ(T) curves of Fig. 7.1.

the T^2-coefficient appears to not vary with thickness, see Fig. 7.3a), suggesting that the electronic correlations are not strongly thickness-dependent.

Impurities in these films could manifest in the form of point defects, vacancies, or, as seen in electron microscopy, cation stacking faults [131]. In resistivity measurements, impurities mostly contribute to the residual resistivity. Removing the residual resistivity (or, in this case, the 4 K resistivity) from the room temperature value and converting to conductivity provides a measure of the thickness-dependent effect with the impurity contribution removed. As shown in Fig. 7.3b), the conductivity peak is diminished slightly by this treatment, but remains robust, indicating that the trend is not linked to defects and that another temperature-dependent scattering mechanism must be dependent upon thickness.

The 2-D Hall carrier density is plotted in Fig. 7.3c) along with a linear fit to the data (dashed line). The sheet carrier density is found to be rather linear with thickness, providing a 3D hole density of 1.5 x 10^{22} cm^{-3}. The linear fit almost intercepts the origin, suggesting that these films have no "dead layers". The perpendicular magnetoresistance at 4 K for three thicknesses of $LaNiO_3/LaAlO_3$ is shown in Fig. 7.3d). The magnetoresistance is less than 0.1% T^{-1}, in both perpendicular and parallel field, the latter indicating that there is negligible effect of magnetic impurities.

The importance of the lattice structure, specifically the Ni-O-Ni bond angle, in determining the physical properties of the nickelates, is well-established, see for instance the phase diagram in Fig. 4.1. It is possible that in these $LaNiO_3/LaAlO_3$ samples there is a variation of the average structure with total film thickness, confirmed by Raman spectroscopy, as discussed shortly. Although, as described in Chapter 6, for films of $LaNiO_3/LaAlO_3$, at least the c-axis parameter and Glazer rotations, both film-averaged, are independent of

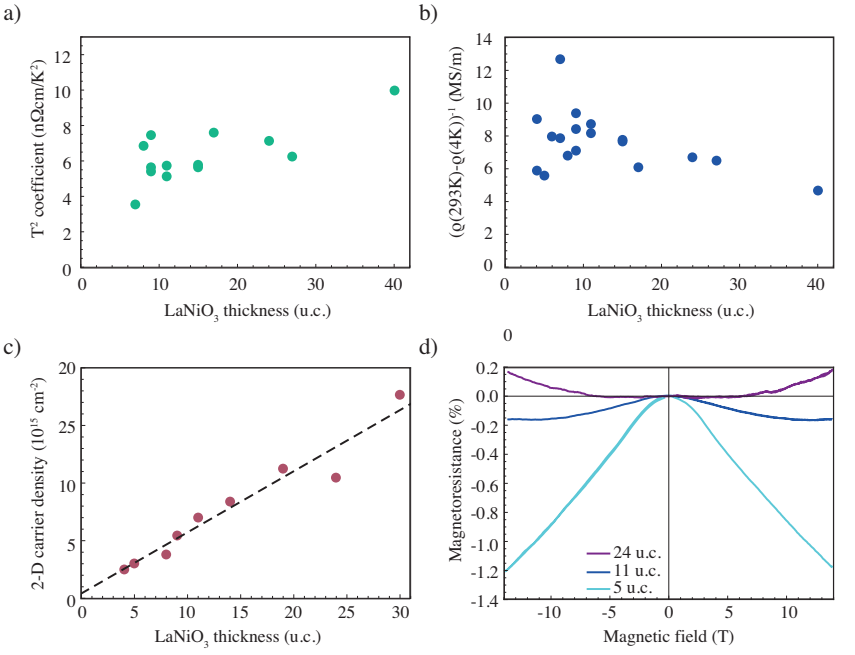

Figure 7.3: a) The A coefficient from the fit $\rho(T) = \rho_0 + AT^2$ as a function of the film thickness. b) The conductivity with the impurity contribution removed as a function of the film thickness. c) The 2-D carrier density as a function of the total film thickness. The dashed line is a linear fit to the data. d) The out-of-plane (perpendicular) magnetoresistance for three different thicknesses of $(001)_{pc}$-oriented $LaNiO_3$/$LaAlO_3$. Published in [131].

the thickness ($c \approx 3.92$ Å, $\alpha = \beta \approx 1$ º and $\gamma \approx 10$ º).

The structure of this system has been previously studied and a strong surface distortion was observed by Kumah *et al* [112, 133]. Such a distortion is not unexpected; as mentioned in Chapter 3, surfaces are often unstable and a structural reconstruction is one possible route to minimise the energy. Added to this general feature of surfaces is the polar nature of the $LaNiO_3$ surface in the (001) crystallographic orientation. The kind of surface buckling discussed in [133] results in a decreased Ni-O-Ni bond angle and, so, a decreased orbital overlap and corresponding increase in resistivity. In the same study, the structural distortion on the surface is found to be largely alleviated by the addition of an insulating $LaAlO_3$ encapsulating layer and the resulting film is also found to be more conductive, lending further support to the bandwidth argument [133].

A similar transport study was conducted here on $LaNiO_3$ films of varying

thicknesses capped with an in-situ-grown 1 nm layer of crystalline $LaAlO_3$, the results of which are shown in Fig. 7.4. Panel a) shows the dramatic effect of $LaAlO_3$-capping on the resistivity of the $LaNiO_3$ where, for instance, a 2 u.c. film can be made more than two orders of magnitude more conductive. While the topmost layer of bare $LaNiO_3$ is the highly unstable, distorted surface, the topmost layer in $LaNiO_3$ capped with $LaAlO_3$ is protected. The $LaAlO_3$ layer likely accommodates the distortions that otherwise would have affected the $LaNiO_3$, providing continuity to the polarity as well as completing the oxygen octahedra of the final nickelate layer. The effect of the capping layer on the resistivity decreases as the film thickness increases, reflecting simply the reduced contribution of the surface layers to the overall properties.

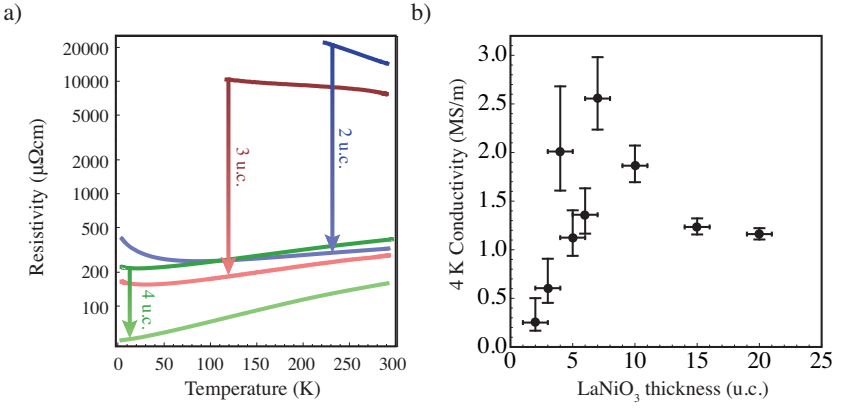

Figure 7.4: a) ρ(T) curves of $LaNiO_3/LaAlO_3$ thin films of 2 u.c. (blue), 3 u.c. (red), 4 u.c. (green) showing the effect of adding a 1 nm $LaAlO_3$ capping layer in-situ. b) The 4 K conductivity of $LaAlO_3$-capped $LaNiO_3/LaAlO_3$ as a function of the thickness of the $LaNiO_3$ layer. The error bars correspond to an uncertainty of ± 1 in determining the film thickness. Published in [131].

Fig. 7.4b) plots the corresponding data to Fig. 7.1b) showing that the conductivity is still enhanced at around the same thickness even with the $LaAlO_3$ cap, the only difference being the shallower decrease in conductivity on the low thickness side of the peak. Worth noting is that even with the addition of the encapsulating layer, a 1 u.c. $LaNiO_3$ film is still too insulating for measurement, indicating that either the structural distortions are not completely suppressed or there is a different origin of the ultrathin insulating phase. Further investigation of the structure is required for clarification.

7.3 Raman Spectroscopy

Raman spectroscopy readily offers information on the symmetry of a given material as well as any qualitative trends in structure. Because it is a scattering technique, the Raman signal is proportional to the sample volume and, for this reason, Raman measurements on ultrathin oxides have not been performed extensively. With the expertise of A. Schober and Dr M. Guennou in the group of Professor Kreisel at the Luxembourg Institute of Science and Technology, we use Raman spectroscopy to gain further insight into the structure and properties of the (001)-oriented $LaNiO_3$/$LaAlO_3$ system. In Fig. 7.5a), some Raman spectra are shown for various thicknesses of $LaNiO_3$, the thinnest film measured being only 3 u.c. (1.3 nm), thinner than previous reports of similar studies [134].

To obtain a Raman signal on such thin films is not trivial. To achieve this, the focal point of the incoming light was gradually scanned in the z-direction, from above the sample, through the film and into the substrate [135]. Because the z-dependence of the signals from the substrate and the film are different, it was possible to perform principal component analysis on these depth-resolved spectra to isolate the film intensity from the substrate intensity.

The modes observed can be assigned the labels A_{1g} and E_g in correspondence with the observed modes in bulk $LaNiO_3$ [136]. The structural excitation relevant for the A_{1g} mode takes the form of a rigid rotation of the oxygen octahedron around the (111) vector and can be seen as a compound of the Glazer α, β and γ rotations discussed in Chapter 6. On the other hand, the mode E_g corresponds to a distortion of the octahedral shape itself, manifested in bond-length changes. Both types of mode are seen to shift to higher frequency upon reducing thickness, see Fig. 7.5b), suggesting that the structure of the $LaNiO_3$ is pushed away from its most energetically favourable arrangement. This mode hardening is likely an effect of increased substrate influence and seems to begin under around 10 u.c., the same thickness where the enhanced conductivity starts to appear. As will be discussed in the following sections, the film structure is found to be strongly modified in the region close to the substrate.

Such a mode hardening would suggest a thickness-dependent structure, averaged over the film since Raman spectroscopy probes the entire sample. However, as already discussed in Chapter 6, the c-axis parameter and Glazer rotations are found to be independent of the thickness. Those measurements were done by x-ray diffraction, which also probes the entire sample, so there is perhaps a more subtle structural effect at play in these $LaNiO_3$/$LaAlO_3$ films. This will be partially elucidated by the structural studies discussed in the following sections.

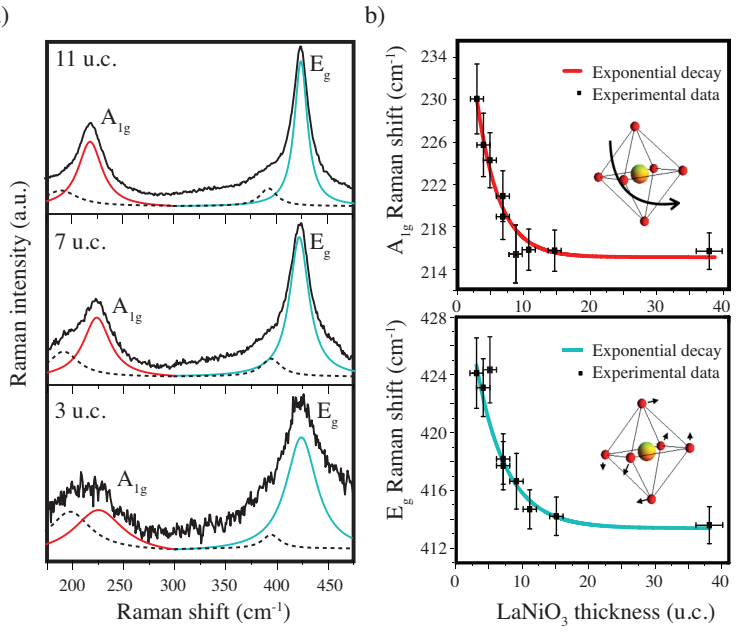

Figure 7.5: a) Raman spectra for three thicknesses of $LaNiO_3/LaAlO_3$. Highlighted are the Lorentzian line shapes used to fit the data. In orange is the mode corresponding to the A_{1g} of bulk $LaNiO_3$ and in green is the mode corresponding to the E_g of bulk $LaNiO_3$. The black dotted line represents additional modes that are expected from the symmetry lowering caused by epitaxial strain, but is not taken into account in the detailed analysis. b) The Raman shift as a function of the $LaNiO_3$ film thickness for the A_{1g} mode (top) and E_g mode (bottom). Both panels contain an exponential decay fit to the data as well as an inset schematising the type of structural distortion relevant for the phonon mode concerned. Published in [131].

7.4 Density Functional Theory Approach

To examine the structure in more detail, ab initio calculations were performed by Dr J. Íñiguez at the Luxembourg Institute of Science and Technology. The study took the form of density functional theory (DFT) calculations implemented in the Vienna ab initio simulation package (see Ref. [137]) on the $LaNiO_3/LaAlO_3$ system with various film thicknesses, giving an atomic resolution of the structure. The calculations take into account the distorted structure of the substrate as well as allow the topmost unit cell of the substrate to relax its atomic positions. These simulations, therefore, produce more than just

$LaNiO_3$ with its unit cell tetragonally distorted to reflect the biaxial strain from the lattice parameter mismatch with the substrate. Some representative results of the DFT calculations for different thicknesses of $LaNiO_3$ are shown in Fig. 7.6.

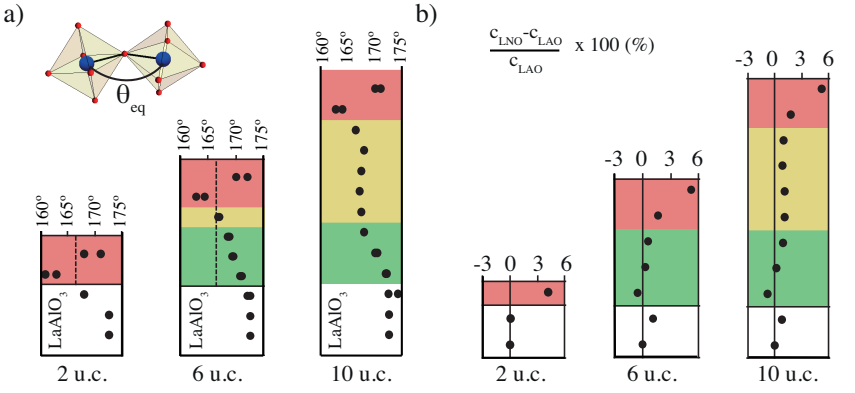

Figure 7.6: Results from DFT simulations. a) The layer-resolved equatorial Ni-O-Ni bond angle in three thicknesses of $LaNiO_3$ film on $LaAlO_3$ substrate. The dashed line represents the result of tetragonally distorting $LaNiO_3$ to match the in-plane lattice parameters of $LaAlO_3$. b) The layer-resolved c-axis expansion, quantified as the La-La distance in the film normalised by the La-La distance in the substrate. Published in [131].

Fig. 7.6 shows the simulated depth evolution of the Ni-O-Ni bond angle (a) and the c-axis parameter (b) for $LaNiO_3$ films on $(001)_{pc}$-oriented $LaAlO_3$ substrate. Looking at Fig. 7.6a) and b), the topmost two u.c. see a 5 % out-of-plane expansion, with an extreme change in bond angle from 163° to 170°. At the heterointerface with $LaAlO_3$, meanwhile, both the bond angle and the out-of-plane parameter tend towards those of the substrate. In the interior region of the film, the structure is free from boundary effects and the out-of-plane expansion is stable at around +1 % while the Ni-O-Ni angle is 167.5°, which is very close to that obtained from simply biaxially straining bulk $LaNiO_3$ by the lattice parameters of $LaAlO_3$ (dashed line). At a lower film thickness of 6 u.c., this interior region has nearly vanished, but the same behaviour of the Ni-O-Ni angle and out-of-plane parameter close to the substrate and on the surface is seen, as for the thicker film. Finally, at 2 u.c., only the characteristic surface structure is retained; it is this distortion that takes dominance towards the atomic limit. The depth-averaged structure, overall, does not depend upon thickness, consistent with the measurements in Section 6.6.2.

The calculations performed here are highly sophisticated, taking into account the reduced symmetry of the film, the structural distortions of the substrate and allowing the atomic positions to relax freely. Studies of this type

require intense computing power, increasing dramatically with the number of atoms. It is for this reason that the thickest sample calculated here was 10 u.c., any thicker would be immensely computationally taxing. Fortunately, complementary information can be obtained experimentally.

7.5 Scanning Transmission Electron Microscopy

The powerful technique of scanning transmission electron microscopy (STEM) was introduced in Section 5.2.9. In order to compare with the theoretical structures, STEM measurements were carried out on the (001)-oriented $LaNiO_3$/$LaAlO_3$ system by G. Tieri and Dr A. Gloter in the laboratory of Professor Stéphan at the Université Paris-Sud. Fig. 7.7a) shows some aberration-corrected annular dark field (ADF) cross-sectional images of $LaNiO_3$ films of different thicknesses. Panel b) of the same figure is the result of geometric phase analysis (GPA) on these samples, giving the out-of-plane (c-axis) lattice expansion. There is no possibility to measure absolute distances in-situ so this quantity is presented normalised to the c-axis parameter of the $LaAlO_3$ substrate below. Fig.7.7b) can therefore be directly compared to Fig. 7.6b). As can be seen, both the DFT and STEM approaches yield similar results; a picture of a film differentiated into three distinct local structures corresponding to the surface layers, interior layers and heterointerface layers respectively. Upon thickness reduction, the bulk-like (but strained) interior layers are the first to be compromised and there is a smooth transition between the part of the structure affected by the heterointerface and the surface structure. Finally, when the atomic limit is approached, the structure of the remaining layers, as determined from both theory and experiment, resembles the characteristic surface structure of the thicker films.

7.6 The Parallel Conductor Model

Still to understand is the nature of the conductivity enhancement shown in Fig. 7.1b). Taking into account the ranges and relative dominances of the three local structures observed in DFT and STEM, a model of parallel conductors was constructed with the following form:

$$\sigma_{total} = \frac{\sigma_s n_s + \sigma_i n_i + \sigma_h n_h}{n_{total}} \tag{7.1}$$

where the σ are the conductivities of the surface (s), interior (i) and heterointerface (h) layers and the n are the number of unit cell layers of each type of structure. The total conductivity, σ_{total}, can then be calculated as a function of the total film thickness ($n_{total} = n_s + n_i + n_h$). The result of the best fit is shown in Fig. 7.8.

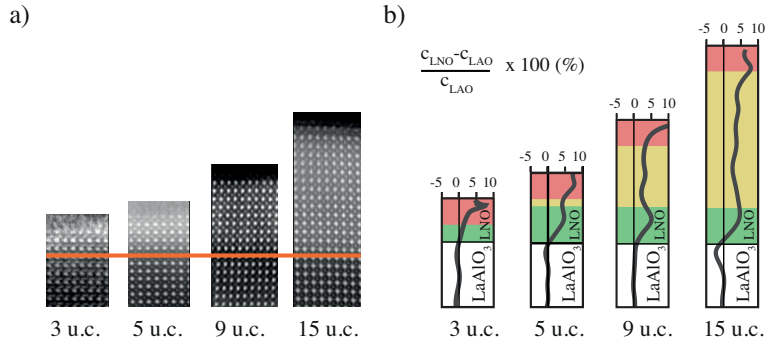

Figure 7.7: a) Aberration-corrected ADF images from STEM of four films of (001)-oriented $LaNiO_3/LaAlO_3$ of varying thicknesses. The interface is marked in red. b) From the images, the result of GPA showing the La-La distance in the film normalised to the same quantity of the substrate. Three characteristic regions of behaviour are highlighted in red (surface), yellow (interior) and green (heterointerface). Published in [131]

Fig. 7.9 summarises the best fit parameters for the three types of layer at both 4 K and room temperature. The conductivity of the interior layers, provides a high thickness asymptote of $\sigma_i = 1$ MS/m at 4 K and $\sigma_i = 0.25$ MS/m at room temperature, marked by the dashed yellow lines on Fig. 7.8. The conductivity of the surface layers, σ_s, is assumed to be the most resistive, at 1 kS/m, in line with the results of the $LaAlO_3$ capping experiment and Ref. [133]. These layers, therefore, provide the slope of the decreasing conductivity towards the lowest thicknesses. The sum of the thicknesses of the surface and heterointerface layers, $n_s + n_h$, determines the position of the peak and the thickness of the interior layers, n_i is simply what remains after subtracting n_s and n_h from the total thickness. Therefore, the only fully free parameter in the model of parallel conductors is the conductivity of the heterointerface layers, σ_h, which is found to be five times greater than the conductivity of the interior layers, σ_i, at 5 MS/m at 4 K and 1.3 MS/m at room temperature. The total film conductivity enhancement seen for thicknesses between 6 - 11 u.c. can therefore be attributed to these heterointerface layers. The thickness of the enhancement simply corresponds to the thickness with the maximum number of these layers before dilution by the lower-conductivity interior layers at higher thickness.

Also shown on Fig. 7.8a), as blue dots, is the conductivity calculated directly from the ab initio structures by Professor Filippetti at the Università di Cagliari. The ab initio conductivity, which is calculated by the Bloch-Boltzmann approach implemented in BoltZTrap code (see Ref. [138])assuming a constant scattering rate, reproduces the peak in conductivity at 8 u.c. but with a smaller amplitude than the corresponding experimental data. Unfortunately, the ab

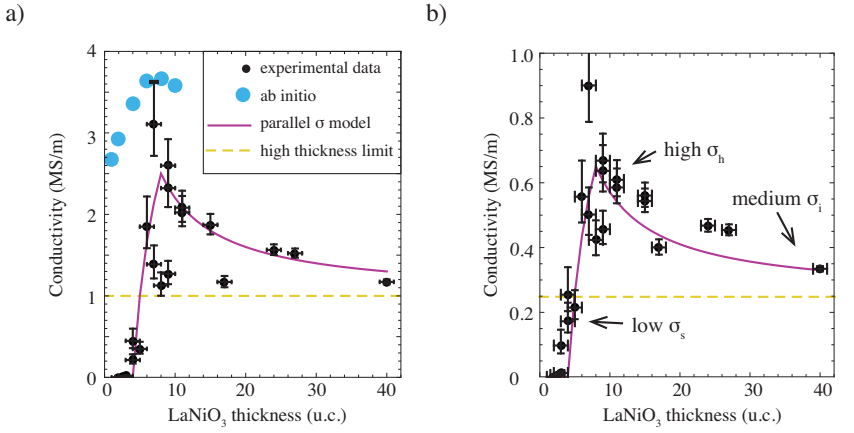

Figure 7.8: The best fit parallel conductor models at a) 4 K and b) room temperature. In both, the pink line traces the output of the parallel conductor model with the parameters of best fit, described in the text and summarised in Fig. 7.9. The dashed yellow line corresponds to the conductivity of the interior layers alone and the blue circles in panel a) represent the result of calculating the conductivity directly from the ab initio structures. Published in [131].

initio conductivities, as with the DFT simulations from which they were derived, could not be calculated above a thickness of 10 u.c. due to the high consumption of computing resources in producing the original structures.

7.7 Discussion

Heterointerfaces can have chemical, polar, and symmetry discontinuities, on top of the lattice parameter discontinuity that affects the entire film until strain relaxation. Looking at the parallel conductor model, ab initio structures, and the results of GPA, the film structure starts to match that of the substrate within 3–4 u.c. of the heterointerface. Similar length scales are found for other perovskite oxide systems [19, 20, 121, 139].

As shown in Fig. 7.6a), the structure of the $LaNiO_3$ film attempts to mimic the structure of the $LaAlO_3$ substrate close to the heterinterface. It may be that the specific structure imposed by the $LaAlO_3$ is important as two similar series of samples were grown on LSAT and $NdGaO_3$ with no significant enhancement of conductivity between 6 - 11 u.c. observed (see Fig. 7.2c)). For the $LaNiO_3$/$LaAlO_3$ system, the Ni-O-Ni bond angle is straighter in the heterointerface layers to match the less-distorted structure of $LaAlO_3$, providing a greater orbital overlap. Considering that the bandwidth is proportional to

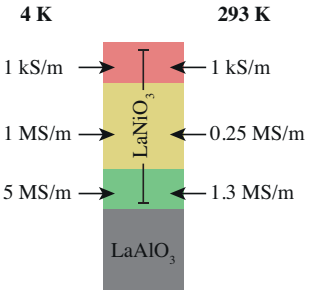

Figure 7.9: The best fit conductivities of the depth-differentiated $LaNiO_3$ layers from the parallel conductor model at both low temperature and room temperature.

$cos^2\theta$ (see Section 2.2 and, in particular, Fig. 2.5c)) a bond angle straightening on the order of what is calculated here would result in, at most, a 10 - 15 % increase in bandwidth. The bandwidth effect alone, therefore, cannot explain a conductivity increase of 5x in the heterointerface layers compared with the interior layers above.

What makes this discussion more complicated for nickelates is that the Ni-O-Ni bond angle also affects the charge transfer between the Ni 3d and O 2p orbitals, where the resulting insulating gap decreases as the orbital overlap increases. This could add to the bandwidth effect but may still not be enough to account for the 5x inflation in conductivity close to the interface, the exact origin of which is not yet understood [140].

Not captured in the parallel conductor model is the insulating nature of films of 1 - 2 u.c. in thickness as these films are predicted to exhibit the conductivity fitted for only the surface layers of 1 kS/m.

As with the parallel conductor model, the ab initio conductivity, which successfully reproduces the peak in conductivity at 8 u.c., does not adequately describe the behaviour of 1 - 2 u.c. films, which are still very conductive in the theoretical treatment. Add to this the fact that $LaNiO_3/LaAlO_3$ films of less than 2 u.c. cannot be rendered metallic even with the addition of a $LaAlO_3$ encapsulating layer, it is clear that these ultrathin samples that are so close to the atomic limit are subject to effects not captured by any of the treatments discussed in this chapter. Electron-phonon coupling, cation intermixing (which is measured to have a spatial extent of no more than 1 u.c. from the interface in these samples) or vacancies could have a role to play in deciding the physics in this extreme thickness regime. This discussion is relevant for many metallic oxides that become insulating upon reaching the ultrathin limit.

In the end, the parallel conductor model was based upon experimentally and theoretically determined structures, the ab initio conductivity was calculated directly from the DFT structures and the $LaAlO_3$-capping experiments

most likely rely on structural modifications. In doing this, the conductivity enhancement between 6 - 11 u.c. in $LaNiO_3/LaAlO_3$ films can be reliably reproduced, highlighting the significance of, even subtle, lattice-charge coupling in the nickelates.

7.8 Summary

In this chapter we described an unusual thickness-dependence of the electronic properties of a series of $LaNiO_3/LaAlO_3$ films. The conductivity was seen to be enhanced in a thickness regime of 6 - 11 u.c. and this behaviour was explained by an astonishingly large increase of conductivity close to the heterointerface. This region of increased conductivity is of unknown origin and a bandwidth-based argument from the structural modulations is insufficient to account for the increase of 500 %. Also not yet understood is what happens in the ultrathin limit when $LaNiO_3$ becomes completely insulating and none of the approaches taken in this chapter can capture this.

These results would allow the design of heterostructures with a maximum conductivity but also carry implications for heterostructures where single unit cell layers are required.

Chapter 8

The $Nd_{1-x}La_xNiO_3$ Solid Solution

8.1 Motivation

At the beginning of this thesis, we introduced the concept of a *property by design*. In electronic materials, perhaps no property is as sought-after as high temperature superconductivity as the applications are seemingly endless. The exact mechanism of high temperature superconductivity is not yet fully understood and there is a considerable research activity ongoing to try to pin down the origin. Until this has been achieved, one of the most common approaches to engineer superconductivity has been mostly based on empirical observations. That is, to look at a superconductor, note what may be special about it, and attempt to recreate that feature in another system. This was the logic behind searching for superconductivity in $LaNiO_3$-based heterostructures; the electronic structure was thought to mimic the high temperature superconducting cuprates [36].

In this chapter, we discuss a possible link between superconductivity and the phenomenon of *valence skipping* and then describe a potentially analogous system in the nickelates.

8.2 Valence Skipping Elements

Many of the high temperature superconducting cuprates contain heavy metals such as lead, bismuth or thallium, all 6p elements. These elements are all known to be *valence skipping* meaning that there is one valence state whose formation is highly unfavourable; it tends to be skipped. Fig. 8.1 shows the electronic configurations for these heavy metal valence states. The one in the

middle is the one that is skipped for all three elements and corresponds to Tl^{2+}, Pb^{3+} and Bi^{4+}. The reason this ionisation state is skipped is clear when considering that the 6s orbital is half filled while the valence states with one more or one fewer electron consist of closed shells, the 6s and 5d respectively. This intermediate valence state is less energetically favourable than those to either side.

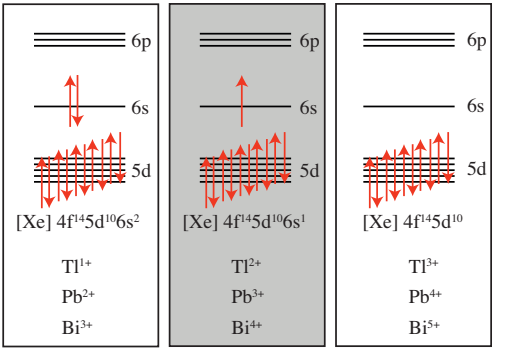

Figure 8.1: Sketches of the electronic configurations of the *valence-skipped* ion (in the central grey box) and the two neighbouring valence states. The corresponding valences of Tl, Pb and Bi are listed below the sketches.

The phenomenon of valence skipping has successfully described the behaviour of, for instance, $BaBiO_3$ [141]. As with most perovskites, the valence is set by the A-site cation and since barium can only oxidise into a 2+ valence state, the bismuth must nominally be in its 4+ state. This would, as shown by Fig. 8.1, give a half-filled band and $BaBiO_3$ should thus be metallic. It is, however, an insulator. It is also found to be non-magnetic, suggesting that bismuth is not in the 4+ (spin $\frac{1}{2}$) state so the insulating behaviour cannot be explained by Mott physics either. In fact, it happens that $BaBiO_3$ is charge disproportionated in order to avoid the unfavourable 4+ state [142]. This means that $BaBiO_3$ is divided into two distinct interpenetrating sublattices; one where the bismuth sites are 3+ oxidised and one where they are 5+ oxidised.

In free space, no spontaneous disproportionation will occur. In a crystal, on the other hand, the electric field can locally screen the ionic charge and change the onsite Coulomb repulsion, U. In some cases, the skipped valence state is characterised by a *negative* U [143]. For this reason, valence skipping insulators are also known as *negative U* insulators, a concept first introduced by Anderson [144].

Negative U insulators can, in some ways, be seen as the “opposite” to a Mott

insulator. While Mott insulators, with a positive U, prefer to have the electrons localised with one per site, in negative U insulators it is energetically favourable to have a double occupancy on one site and an empty site to compensate.

As mentioned, valence skipping elements are often found in high temperature superconductors such as the $Bi_2Sr_2Ca_{n-1}Cu_nO_{2n+4+x}$ family [145] or the $TlBa_2Ca_{n-1}Cu_nO_{2n+3}$ family [146]. The link between valence skipping elements and superconductivity goes beyond this possible coincidence, however; superconductivity in some non-transition metal-based materials has been ascribed to a negative U-mediated pairing. $Tl_xPb_{1-x}Te$, $BaPb_{1-x}Bi_xO_3$, $Ba_xRb_{1-x}BiO_3$ and $Ba_xK_{1-x}BiO_3$ are all found to be superconducting with rather high critical temperatures (up to 30 K) and all contain one or more elements known to skip valences [147–150].

8.3 Negative U-mediated Superconductivity

The mechanism for negative U-mediated superconductivity was explained by considering fluctuations between the two degenerate valence states either side of the skipped valence [143, 147]. These fluctuations may provide the necessary interaction for an unconventional, real space, pairing of electrons that leads to superconductivity and persists even in the normal state. It has been described as a charge Kondo effect, in analogue to the original spin Kondo effect [148, 151, 152].

So far, negative U-mediated superconductivity has mostly been discussed in the context of the doped monochalcogenides and the $BaBiO_3$ compounds as these certainly contain a nominally valence skipping cation. Similar physics may be achieved in systems that do not explicitly host valence skipping chemistry. For instance, Geballe and Kivelson suggest that oxygen vacancies may serve as negative U centres in $SrTiO_3$ [153].

A potential system in which negative U centres may be considered is the nickelates. As discussed in Chapter 4, below the metal-insulator transition (MIT), all the RNiO$_3$ compounds with $R \neq$ La enter a bond disproportionated state [45].

Along with the bond disproportionation, there is also a charge disproportionation (d^8 + d^6 in the low energy description) or a disproportionation of charge *density* (d^8 + $d^8\underline{L}^2$ in the ligand hole picture). This is not quite the same scenario as valence skipping, as the Ni^{3+} state is not valence skipped and, in the low energy picture, exists above the MIT. It can be argued, however, that the resulting charge arrangement in the nickelate insulating state bears a certain similarity to the valence skipped compounds. What appears to be important for the superconductivity in these valence skipping, negative U compounds, is that there are quantum fluctuations between the two distinct sites of the disproportionation. For this reason, it is possible that superconductivity will not be found simply by doping one of the RNiO$_3$ compounds in the

insulating phase. The nickelate disproportionation is static in nature and, perhaps, too stable in energy. This is characteristic of such systems; if the negative U is too large in magnitude then an insulating localised state will be favoured. We therefore look for a material that has instabilities towards charge disproportionation, rather than one that is fully localised already. This may still be achievable in the nickelates.

In a solid solution of one of the $R\mathrm{NiO}_3$ compounds that has an MIT and LaNiO_3, which is metallic at all temperatures in bulk, there will be a material with a particular composition that will be just on the verge of becoming insulating [30, 154–157]. At this composition, the system should be close enough to being metallic that there is still a certain level of electron itinerancy and close enough to the insulating $R\mathrm{NiO}_3$ that the system has a propensity to charge disproportionate. This may be the optimal place to start looking for negative U-mediated superconductivity.

The $\mathrm{Nd}_{1-x}\mathrm{La}_x\mathrm{NiO}_3$ solid solution will be discussed in this chapter with the motivation of finding the composition, x, which may serve as a negative U-mediated superconductor or, perhaps, as the parent compound of one. Once the composition has been determined, it may be necessary to add carriers by, for example, electric field gating, in order to tune the degeneracy of the disproportionated sites.

In the process of determining the optimal composition, which itself depends upon the substrate, a systematic characterisation of the phase diagram was carried out, as described in the remainder of this chapter.

8.4 Growth of Solid Solution Thin Films

Gradually replacing neodymium by lanthanum in the $\mathrm{Nd}_{1-x}\mathrm{La}_x\mathrm{NiO}_3$ phase diagram proceeds according to the Hume-Rothery rules, which state that, for a mixture to be considered a substitutional solid solution, the substituting and substituted ions must have compatible radii, compatible electronegativities and compatible valences. Neodymium and lanthanum should satisfy these rules and, indeed, the $\mathrm{Nd}_{1-x}\mathrm{La}_x\mathrm{NiO}_3$ solid solution has already been grown as bulk polycrystalline samples [30, 154–156, 158]. Work has also been carried out on $\mathrm{Nd}_{1-x}\mathrm{La}_x\mathrm{NiO}_3$ thin films grown by molecular beam epitaxy [157].

Here, the films were grown by radio frequency off-axis magnetron sputtering, see Section 5.1. Sputtering thin films of a solid solution compound can be done by a standard growth where the target corresponds to the stoichiometry of the desired film with the correct composition. If the study in mind requires a systematic change of the composition, however, this may be inefficient as it would require a brand new target for each desired composition. A more practical approach is to use two targets, representing the two end compounds, and mix them during growth.

Two stoichiometric targets of NdNiO_3 and LaNiO_3 were set up in the same

deposition chamber. Then, the solid solution thin film was achieved by a series of sub-depositions from the two targets alternately, the length of time of deposition from each target depending upon the desired composition. The ideal solid solution sample would have a homogenous mix of Nd and La, even on the smallest scale. To achieve the best mixture possible and avoid polysomatic samples, the sub-depositions should be extremely short. On the other hand, due to the time that the central control of the sputtering system requires to verify the stability of the pressure, gas flow and temperature between depositions (around one minute), smaller unit cell coverages drives up the total deposition time significantly.

In order to check if film properties are affected by this growth method and by the choice of sub-deposition coverage, several samples were grown with varying unit cell coverages per deposition. For the end materials, which can be grown without target mixing, the sub-deposition films were compared directly to the single deposition films. This is summarised in Fig. 8.2.

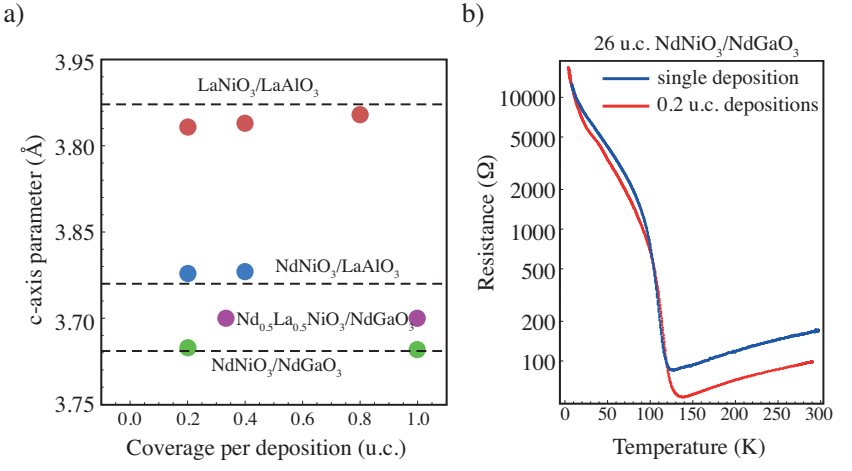

Figure 8.2: a) The c-axis parameters of $LaNiO_3/LaAlO_3$ films (red), $NdNiO_3/LaAlO_3$ films (blue), $NdNiO_3/NdGaO_3$ films (green) and the solid solution $Nd_{1-x}La_xNiO_3$ films with x = 0.5 on $NdGaO_3$ (purple) all as a function of the unit cell coverage per sub-deposition. The dashed lines indicate the c-axis for a film that was grown in a single deposition, where such a sample is possible. All films within the same series have the same thickness, either 18 u.c. (7 nm) or 26 u.c. (10 nm), and were grown on $(001)_{pc}$-oriented substrates. b) The resistance as a function of temperature (warming up only) for two "equivalent" samples of (001)-oriented $NdNiO_3/NdGaO_3$ where one film was grown in a single deposition (blue) and the other in sub-depositions of 0.2 u.c. showing the MIT occurring at the same temperature.

Fig. 8.2a) shows how the c-axis parameters of the films depend upon the unit cell coverage per sub-deposition. For the end compounds, the dashed lines indicate the c-axis parameter of a film grown by a single deposition (the conventional method). What is clear is that there is no discernible dependence of the film structure on the unit cell coverage and films grown by the sub-deposition technique are not noticeably different from those grown in the conventional way. What may even be the case in the sub-deposition growth of $LaNiO_3$/$LaAlO_3$ (red points) is that the film quality is slightly higher than the equivalent single-deposition film. This is suggested by the decreasing c-axis lattice parameter with decreasing sub-deposition unit cell coverages since, typically, a larger c-axis indicates a higher defect density in the sample [159]. It may be that during the time between sub-depositions, the newly deposited layer of the film is able to stabilise and reach its lowest energy configuration before the next sub-deposition begins.

Not only the structural properties but the physical properties seem not to be significantly affected by the sub-deposition growth method. In Fig. 8.2b) are two curves of resistance as a function of temperature, one for a single deposition $NdNiO_3$/$NdGaO_3$ film and the other for a $NdNiO_3$/$NdGaO_3$ film grown in stages of 0.2 unit cell coverage sub-depositions. The temperature of the MIT, as well as its sharpness, is unchanged by this difference in growth.

To maintain time efficiency in the sample growth while still attempting to maximise the sample quality, a sub-deposition time equating to a 0.4 unit cell coverage was decided upon (although a larger coverage would not be expected to significantly affect the film properties, according to Fig. 8.2). This means that, for instance, for x = 0.5 there would be 0.2 u.c. of $NdNiO_3$ deposited followed by 0.2 u.c. of $LaNiO_3$. This is then repeated for the appropriate length of time to grow the desired sample thickness.

With the confirmation that the solid solution films can be prepared reliably, the study on their properties across the composition range can proceed. The La:Nd ratio is not easily verifiable by, for instance, Rutherford back scattering as the films are thin and the two cations are very similar in atomic number. Instead, the calibration of the separate growth rates of each compound is used and this appears to be a reliable tactic as seen in, for example, the monotonic change of the frequency of the E_g-like Raman mode (Fig. 8.7). All the films reported in the following section were grown at 450 °C in an atmosphere of 0.24 mbar 7:2 Ar:O_2 mix. Four $(001)_{pc}$-oriented substrates were used; $LaAlO_3$ with a lattice parameter of 3.789 Å (compressive strain of -1.3 % on $LaNiO_3$ and -0.6 % on $NdNiO_3$), $NdGaO_3$ with a lattice parameter of 3.86 Å (tensile strain of +0.6 % on $LaNiO_3$ and +1.3 % on $NdNiO_3$), LSAT with a lattice parameter of 3.87 Å (tensile strain of +0.8 % on $LaNiO_3$ and +1.6 % on $NdNiO_3$) and $SrTiO_3$ with a lattice parameter of 3.905 Å (tensile strain of +1.7 % on $LaNiO_3$ and +2.5% on $NdNiO_3$).

8.5 Probing the Phase Diagram

8.5.1 The Metal-Insulator Transition

While $NdNiO_3$ (x = 0) has an insulating ground state, $LaNiO_3$ (x = 1) is metallic in bulk. Therefore the solid solution $Nd_{1-x}La_xNiO_3$ should have an MIT at 0 K for some composition. This composition would also be expected to depend upon the substrate.

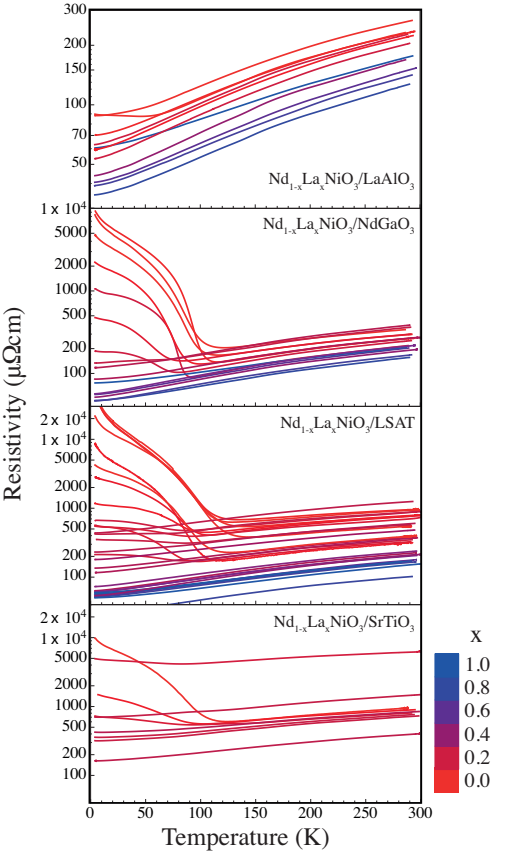

Figure 8.3: Resistivity as a function of temperature for 18 u.c.-thick $Nd_{1-x}La_xNiO_3$ of different compositions on $(001)_{pc}$-oriented substrates of $LaAlO_3$, $NdGaO_3$, LSAT and $SrTiO_3$. The composition is indicated by the colour code, see the key to the right. Only the curves on increasing temperature are shown for simplicity but the transition, when it occurs, is first order with a visible hysteresis.

Fig. 8.3 shows how the MIT at x = 0 is lowered in temperature before being suppressed entirely as the lanthanum content is increased. On $NdGaO_3$, LSAT and $SrTiO_3$ substrates, this occurs at around x = 0.2. On the other hand, for the series grown on $LaAlO_3$, almost all the compositions are metallic to low temperatures. Even pure $NdNiO_3$ (x = 0) on $LaAlO_3$ has only a small upturn in resistivity at around 45 K. $(001)_{pc}$-oriented $NdNiO_3/LaAlO_3$ is usually observed to have an MIT at around 100 K or higher [53, 160]. It has, however, also been reported to be fully metallic [50, 161]. This discrepancy may be due to an oxygen off-stoichiometry as the $RNiO_3$ compounds are found to be highly sensitive to the oxygen concentration [159, 162, 163].

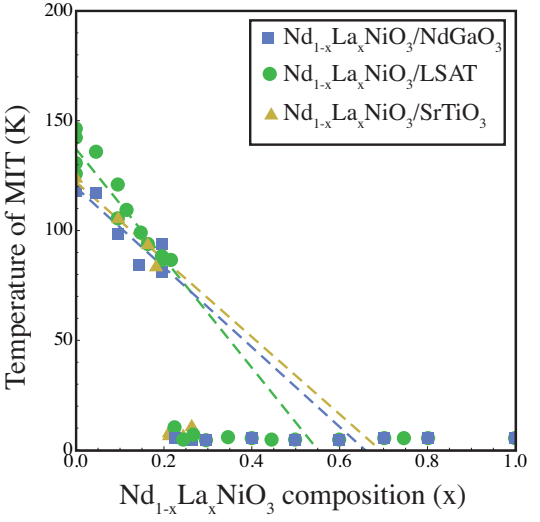

Figure 8.4: The metal-insulator transition (MIT) temperature as a function of the composition of $Nd_{1-x}La_xNiO_3$ on $(001)_{pc}$-oriented LSAT,$(001)_{pc}$-oriented $NdGaO_3$ and $(001)_{pc}$-oriented $SrTiO_3$. The MIT temperature was taken as the temperature of minimum resistivity in the warming part of the ρ(T) curve. The dashed lines are linear fits to each of the sets of data in the region x < 0.2.

From the ρ(T) curves shown in Fig. 8.3, the temperature of the minimum resistivity of each was taken as the temperature of the MIT. This was then plotted as a function of the composition to give Fig. 8.4, providing the first points for the phase diagram of the $Nd_{1-x}La_xNiO_3$ solid solution under tensile strain. The series on $LaAlO_3$ was omitted from this figure as only one of the compositions shows a finite MIT temperature at x = 0.

It is found that, upon increasing lanthanum content away from pure $NdNiO_3$, the MIT temperature reduces rather linearly, as shown by the dashed lines that are linear fits to the points. Following this linearity, the MIT would

be expected to be tuned to 0 K for compositions around x = 0.6 and this, then, would be the region in which to look for negative U physics and, possibly, negative U-mediated superconductivity. The low-x linear trend, however, does not persist as all samples with x > 0.2 are found to be metallic. A further curiosity is that the linear decrease up until the sharp drop at x = 0.2 is seen on all three tensile substrates. The reason for this drop is not well-understood but may be related to the film symmetry and this will be discussed in Sect. 8.5.3.

As no samples have been obtained with an MIT lower than 80 K, it is not trivial to identify the optimal composition of $Nd_{1-x}La_xNiO_3$ in which to search for negative U physics and even superconductivity. Nevertheless, several low temperature studies, with and without an attempt at doping, have been performed on various compositions between 0.19 < x < 0.45. Sect. 8.6 will describe some of these efforts.

In the following sections, we discuss the further mapping out of the phase diagram.

8.5.2 The Néel Transition

At the time of writing, no measurements have been performed on the $Nd_{1-x}La_xNiO_3$ thin film system to check for magnetic ordering. What might be expected is that, in analogue to the bulk phase diagram, there is a Néel transition concomitant with the MIT. Even if this is not the case, it is likely that there is still a crossover of magnetic behaviour; while $NdNiO_3$ (x = 0) has an insulating and antiferromagnetic ground state, the $LaNiO_3$ thin film (x = 1) is metallic and paramagnetic. Interestingly, in the series of $Nd_{1-x}La_xNiO_3$ powder samples reported in Ref. [154], they find not a sharp magnetic transition but rather a smooth evolution of the magnetic susceptibility from x = 0 to x = 1.

Future resonant soft x-ray diffraction studies will uncover more about the Néel transition in these films and the onset of, or continuation of, the antiferromagnetic state in nickelates.

8.5.3 The Structural Transition

In bulk $NdNiO_3$ the metal-insulator transition is concomitant with both the Néel transition and with a symmetry-reducing structural transition. Neither of these two transitions that should occur with the MIT have been probed so far in the $Nd_{1-x}La_xNiO_3$ thin film system. There is, however, a second structural transition in the $Nd_{1-x}La_xNiO_3$ phase diagram that will be discussed in detail here.

This second structural transition should be evident at room temperature since the two end compounds are of different symmetries. The goal is to determine the composition where the crossover from $Pnma$ (orthorhombic at x = 0, $NdNiO_3$) to $R\bar{3}c$ (rhombohedral at x = 1, $LaNiO_3$) takes place and follow

its dependence upon temperature. In thin films, $R\bar{3}c$ rhombohedral symmetry is, in fact, reduced to monoclinic symmetry with $C2/c$ space group, which is a subgroup of $R\bar{3}c$, due to the biaxial strain. According to group theory, neither $Pnma$ - $R\bar{3}c$ nor $Pnma$ - $C2/c$ are allowed transitions but, nevertheless, the two end compounds are well characterised and a crossover of structure must take place. The group theoretical considerations are discussed further at the end of this section.

To probe this $Pnma$ to $C2/c$ structural crossover in $Nd_{1-x}La_xNiO_3$ thin films, studies were carried out using symmetric scans in x-ray diffraction (XRD) and Raman spectroscopy. See Chapter 5 for a description of these two techniques.

X-ray Diffraction

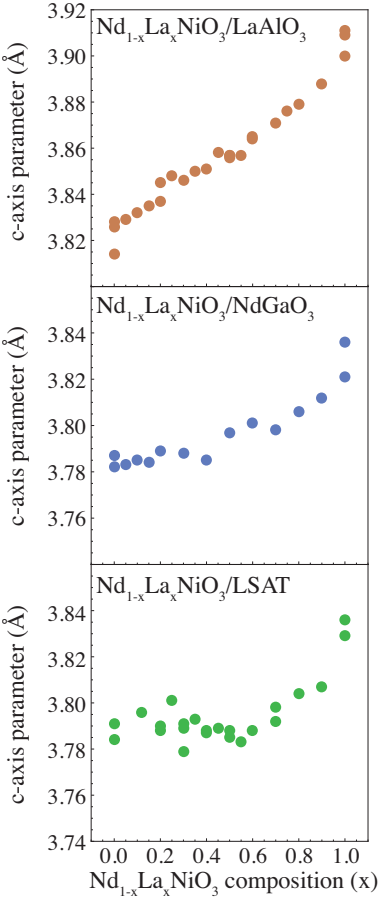

Figure 8.5: The c-axis parameters extracted from XRD as a function of the $Nd_{1-x}La_xNiO_3$ composition. Shown on three $(001)_{pc}$-oriented substrates, $LaAlO_3$ (top), $NdGaO_3$ (middle) and LSAT (bottom).

Fig. 8.5 shows the out-of-plane (c-axis) parameters for $Nd_{1-x}La_xNiO_3$ films of 18 u.c. (7 nm) thickness. The room temperature c-axis parameters from symmetric XRD scans (see Section 5.2.2) do not show a clear anomaly with composition (such as a kink, jump or change of slope) as might be expected upon encountering the structural phase transition. Nonetheless, the trends are interesting.

The series on $LaAlO_3$ (top panel of Fig. 8.5) gives a rather linear behaviour

of the c-axis parameter with composition, seeming to adhere to the empirical Vegard's law, which predicts the lattice parameters of a solid solution from a rule of mixtures of the end compounds [164]. This is surprising given the expected structural phase transition. There does, however, seem to be a very slight curvature that is also observed, to a greater extent, for the other two substrates. A curved behaviour, rather than a linear one, may be expected given that these are not bulk crystals but rather thin films that are constrained in two dimensions and subject to an out-of-plane expansion that will depend upon the Poisson ratio. The large curvature observed for films grown on $NdGaO_3$ and LSAT cannot be explained by this alone. There is also a considerable level of sample-to-sample scattering on these two tensile substrates that may be due to a variation of substrate quality. It is apparent, then, that in order to study the structural transition, room temperature symmetric XRD scans may not be the most ideal approach.

Raman spectroscopy

Collaborating with the group of Professor Kreisel at the Luxembourg Institute of Science and Technology, room temperature Raman spectroscopy was then carried out on the same series of samples and the results are displayed in Fig. 8.6. Only $LaAlO_3$ and LSAT substrates were used for the study as $NdGaO_3$ is very Raman active and therefore impractical as a substrate for thin films in Raman spectroscopy measurements. It is likely, however, that $Nd_{1-x}La_xNiO_3/NdGaO_3$ would give a similar outcome as $Nd_{1-x}La_xNiO_3$/LSAT due to the similarity in the substrate lattice constants, and, therefore, the strain they apply. Indeed, the $Nd_{1-x}La_xNiO_3$ c-axis lattice parameters and metal-insulator transition temperatures already shown are very similar between the two substrates.

Bulk $LaNiO_3$ hosts five Raman active modes; four degenerate E_g modes and one A_{1g} mode [136]. Although it is not strictly correct to maintain these labels for thin film $LaNiO_3$, due to its lowered symmetry, the structural distortions corresponding to these modes are still observed and labelled as A_{1g}-like and E_g-like accordingly, as sketched in Fig. 8.7. The E_g-like mode represents changes in the bond lengths of the structure while the A_{1g}-like mode is related to rotations of the oxygen octahedra of the perovskite pseudocubic unit cell.

Being orthorhombic, bulk $NdNiO_3$ has many more Raman modes than $LaNiO_3$; 24 to be precise [165, 166]. As can be seen in Fig. 8.6, there is a mode that appears at around 250 cm^{-1} on the $NdNiO_3$ side of the $Nd_{1-x}La_xNiO_3$ phase diagram that is not present on the $LaNiO_3$ side. This mode is most likely A_{1g}-like and also related to rotations of the O_6 octahedra [167]. Very similar results were obtained for $Nd_{1-x}La_xNiO_3/LaAlO_3$ as for the $Nd_{1-x}La_xNiO_3$/LSAT series shown in Fig. 8.6.

Notably, the Raman spectra presented in Fig. 8.6 do not show any phase coexistence and, rather, demonstrate a smooth evolution from $NdNiO_3$ to $LaNiO_3$.

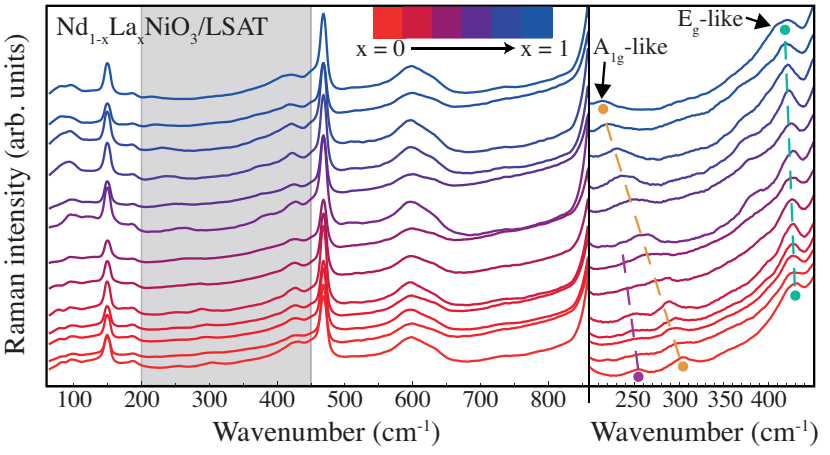

Figure 8.6: Raman spectra for 18 u.c. $Nd_{1-x}La_xNiO_3$ on (001)-oriented LSAT substrate. The grey box outlines the area that is shown in close up on the right. The A_{1g}-like and E_g-like modes of $LaNiO_3$ are indicated by the orange and green dots respectively. For the x = 0 composition (pure $NdNiO_3$) there is an additional mode marked by the violet dot. Spectra are vertically shifted for clarity by an offset proportional to the composition.

This suggests that the films represent true homogeneous solid solutions with no polysomatic phase segregation.

Fig. 8.7 plots the Raman frequencies of the modes pinpointed in Fig. 8.6 as a function of the film composition from x = 0 (pure $NdNiO_3$) to x = 1 (pure $LaNiO_3$), now with the corresponding series on $LaAlO_3$ shown in the left panel. One of the first things to notice is that all the modes vary rather smoothly and virtually no sample-to-sample scattering is observed, even for the series on LSAT that produced a significant level of scattering when plotting the c-axis parameter (Fig. 8.5 lower panel). This smooth evolution indicates that the composition can be reliably controlled and that the growth rates used for calibration are very stable.

The E_g-like mode (in green) is seen to decrease, or *soften*, almost linearly as the composition x is increased. This softening is as a result of the increasing unit cell size when going towards $LaNiO_3$ and so increasing bond lengths. It can also be seen shifting when comparing the samples grown on $LaAlO_3$ (left) to those grown on LSAT (right), which shows how the strain state affects the phonon vibrations.

The A_{1g}-like mode (orange) also softens as the composition goes from $NdNiO_3$ to $LaNiO_3$. This mode, at least in $LaNiO_3$, is well understood to be related to the out-of-phase rotations of the oxygen octahedra. The fact that this type of mode is harder in $NdNiO_3$ is due to the fact that the oxygen octahedra

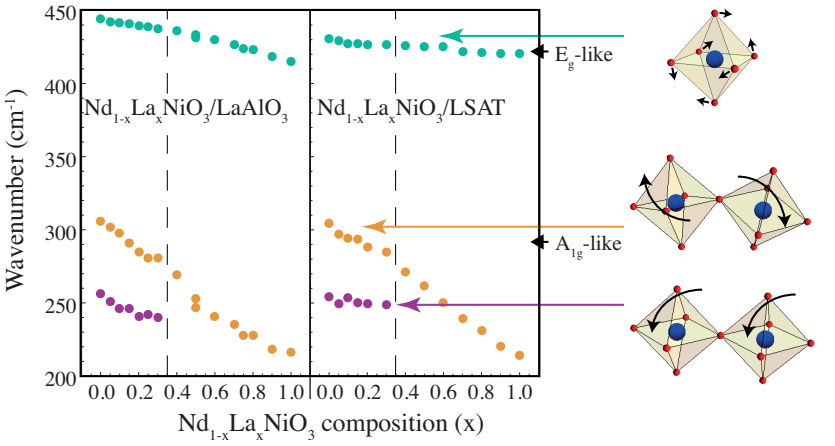

Figure 8.7: Raman mode frequencies as a function of composition for the $Nd_{1-x}La_xNiO_3/LaAlO_3$ system (left) and the $Nd_{1-x}La_xNiO_3/LSAT$ system (right). The probable structural distortions corresponding to the observed modes are sketched on the far right.

are subject to a greater structural distortion. There is also a visible anomaly at around x = 0.35, which may be the first indication of a structural transition. Perhaps a stronger sign of the $Pnma$ to $C2/c$ structural transition is seen when following the mode coloured in violet in Fig. 8.7. As this mode completely disappears above x = 0.35, the same composition as the anomaly in the A_{1g}-like one, this already suggests that the structural transition has been uncovered. Furthermore, this mode is understood to correspond to a rotation of oxygen octahedra, similar to the A_{1g}-like one, in bulk $NdNiO_3$ [167]. Distinct from the A_{1g} mode of $LaNiO_3$, however, this mode probably corresponds to an *in-phase* rotation of O_6 octahedra. Recall that the Glazer systems of $NdNiO_3$ and $LaNiO_3$ films are $a^+b^-b^-$ and $a^-b^-b^-$ respectively. The in-phase rotation-related mode is therefore unique to the $NdNiO_3$ side of the phase diagram and its disappearance is indicative of the departure from the $Pnma$ phase. Therefore, for $Nd_{1-x}La_xNiO_3$ films, regardless of the substrate, the room temperature transition is taken to occur at x = 0.35.

Interestingly, the room temperature Raman spectra are very similar between $Nd_{1-x}La_xNiO_3/LaAlO_3$ and $Nd_{1-x}La_xNiO_3/LSAT$ despite the differences in electronic transport, $Nd_{1-x}La_xNiO_3/LaAlO_3$ being almost always metallic to low temperature. As shown on the bulk phase diagram (Fig. 4.1), however, a metallic phase can exist with either the orthorhombic or rhombohedral structure. It is only the structural transition not studied for the $Nd_{1-x}La_xNiO_3$ system yet, $Pnma$ to $P2_1/n$, that is intimately tied to the MIT.

The first point on the structural phase diagram has now been obtained. In order to map out the rest of the phase diagram, it will be necessary to move up and down in temperature and either repeat the Raman spectroscopy measurements or measure, for instance, half-integer Bragg peaks in XRD (see Chapter 6). Furthermore, in order to fully understand the structural phase diagram, a structural refinement should be performed to verify the assumed symmetries. Confirmation will come from calculation of the phonon modes, allowing comparison with the experimental Raman data. Moreover, from a group theory perspective, the symmetries in the $Nd_{1-x}La_xNiO_3$ phase diagram are rather complex, as will now be addressed.

Group Theoretical Considerations

As mentioned, a direct transition between the space groups $Pnma$ and $C2/c$ or $R\bar{3}c$ is not allowed by symmetry. This then raises the question of how the crossover between the two end compound structures can take place.

Eventually, $Nd_{1-x}La_xNiO_3$ could be in a similar situation to what was reported in the ferroelectric $PbZr_{1-x}Ti_xO_3$ solid solution [168]. In the $PbTiO_3$ side of the phase diagram, the structure is tetragonal, while, at the $PbZrO_3$ side, it is rhombohedral. These two structures have no group-subgroup relation so a direct transition between them is not allowed. It was shown in [168] that there is a narrow, almost vertical (weak temperature dependence) band in the phase diagram, between tetragonal and rhombohedral, corresponding to a monoclinic structure. The space group for this monoclinic unit cell falls into a subgroup of both the tetragonal and rhombohedral space groups meaning that the system has found a way to transition by passing through an allowed intermediate phase.

If, like $PbZr_{1-x}Ti_xO_3$, an intermediate phase exists for $Nd_{1-x}La_xNiO_3$, then the most likely scenario can be reasoned by referring to Fig. 2.3. It is possible that $NdNiO_3$ ($Pnma$) may transition to $LaNiO_3$ ($C2/c$ in thin films) via the higher symmetry tetragonal $Imma$ space group, of which the space groups of the two end compounds are subgroups. By considering the Glazer notation, this two-step transition would be intuitive; the in-phase rotatation in $Pnma$ ($a^+b^-b^-$) is gradually undone until the rotation magnitude along that axis is zero ($a^0b^-b^-$ for the $Imma$ structure) then the out-of-phase rotation is gradually introduced along the same axis to finish in the $a^-b^-b^-$ of $C2/c$. In bulk, the higher symmetry $R\bar{3}c$ space group of $LaNiO_3$ can be reached by the undistorted $Pm\bar{3}m$ ($a^0a^0a^0$) or, more likely, through the $C2/c$ by simply equilibrating the rotation magnitudes around the a- and b-axes with the one around the c-axis to attain the final structure. As in the case of $PbZr_{1-x}Ti_xO_3$, however, such an intermediate phase may only be stable over a narrow range of compositions so to observe it would require an extremely precise structural refinement on very specifically-composed samples.

Recalling the sharp drop in the MIT temperature as a function of

$Nd_{1-x}La_xNiO_3$ composition, a possible explanation for this is now appreciated. It could perhaps be that the films with x > 0.2 are blocked in a metastable $C2/c$ structure, not able to transition to $Pnma$. Then, the typical bond disproportionated structure with space group $P2_1/n$ is forbidden by symmetry and the films remain metallic.

Uncovering the reason for the drop in the electronic $Nd_{1-x}La_xNiO_3$ phase diagram, and whether or not it is indeed structural, will require more measurement, either by Raman spectroscopy, XRD or by another means, and low temperature data as well. Whatever the reason for this discontinuity in the MIT temperature with x, it may have profoundly affected the search for superconductivity by negative U centres in $Nd_{1-x}La_xNiO_3$.

8.6 The Search for Superconductivity

8.6.1 Low Temperature Transport

As mentioned earlier, it is possible that, at a composition of $Nd_{1-x}La_xNiO_3$ where the MIT is incipient, negative U physics may be found. The further possibility that such negative U physics may lead to negative U-mediated superconductivity necessitates electronic transport measurements to lower temperatures than those performed while obtaining the electronic phase diagram shown in Fig. 8.4.

Preliminary low temperature transport checks for superconductivity were carried out. Four films of $(001)_{pc}$-oriented $Nd_{1-x}La_xNiO_3$/LSAT (x = 0.30, 0.35, 0.40, 0.45) and two films of $(001)_{pc}$-oriented $Nd_{1-x}La_xNiO_3$/$NdGaO_3$ (x = 0.30, 0.40) were measured down to 30 mK in a dilution refrigerator. All six samples have a finite resistivity at base temperature. They show a resistivity upturn at around 7 K followed by a flattening below 200 mK, see Fig. 8.8.

Similar behaviour as shown in Fig. 8.8b) has previously been observed in $LaNiO_3$ thin films that display metallic behaviour at higher temperatures [169]. The upturn was ascribed to weak localisation while the resistivity saturation below that was discussed in the context of spin fluctuations. Although, the possibility that such behaviour is related to the proximity to a superconducting state cannot be ruled out.

Further low temperature transport measurements will be performed. It may still be the case that no composition of $Nd_{1-x}La_xNiO_3$ is superconducting on its own and, if so, a different approach is required.

8.6.2 Efforts towards carrier doping

In all of the systems that are reported to be superconducting with negative U pairing, there is a certain level of carrier doping required. It is possible that in $Nd_{1-x}La_xNiO_3$, if this does indeed represent a negative U material, it

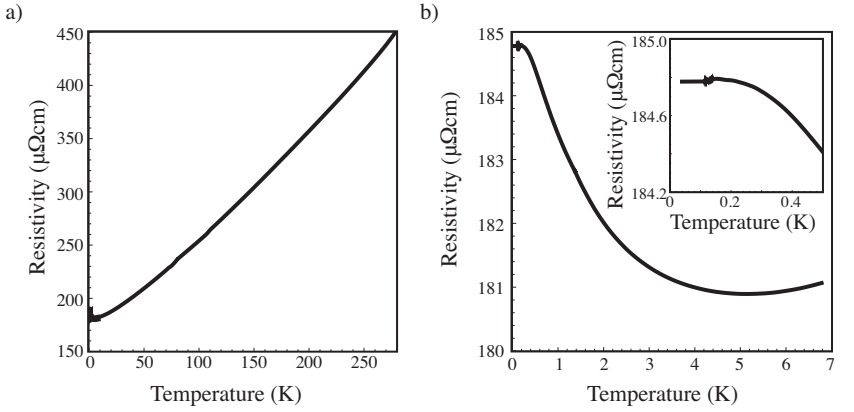

Figure 8.8: Resistivity as a function of temperature for a $(001)_{pc}$-oriented $Nd_{0.65}La_{0.35}NiO_3$/LSAT film of 18 u.c. thickness. a) Shows the data over the full temperature range and b) shows a close up of the resistivity upturn. The inset to b) emphasises the flattening.

will be necessary to do likewise. In this scenario, finding the composition of $Nd_{1-x}La_xNiO_3$ in which the electrons are not fully localised but the system still has the propensity to charge disproportionate amounts to identifying the parent compound of a potential negative U-mediated superconductor.

Electric field effect may provide the necessary orthogonal axis along which a superconducting ground state may be found. $Nd_{1-x}La_xNiO_3$ on, for instance, $SrTiO_3$ (with its high dielectric constant at low temperature) would allow field effect experiments to be carried out in back-gate geometry [170]. To this end, three samples of $Nd_{1-x}La_xNiO_3/SrTiO_3$ were back-gated and measured in a dilution refrigerator. The compositions probed were x = 0.19, 0.22 and 0.25, in other words, both sides of the phase discontinuity at x = 0.20. The back-gate field was swept between -200 V and + 200 V and no field effect was observed for any of the compositions.

It could be that the carriers introduced through back-gating $SrTiO_3$ are not enough, in which case the effect could be effectively increased by structuring a small channel of the film. Alternatively, back-gating relies on the potential difference across the 0.5 mm thick $SrTiO_3$substrate, diminishing the effect. Another option to utilise field effect is to employ ionic liquid gating and bypass the need for a back-gate electrode altogether [171].

A more practical way of introducing carriers to $Nd_{1-x}La_xNiO_3$ may be by interfacial doping. It was found that heteroepitaxial interfaces of $LaNiO_3$ on $LaMnO_3$ are prone to interfacial electron transfer from Mn to Ni. In the hopes of benefitting from this charge transfer, four superlattices of $[LaMnO_3/Nd_{1-x}La_xNiO_3]$/LSAT(001) were grown and measured at low tem-

perature with x = 0.22, 0.24 and either five or ten pseudocubic layers of the nickelate. As in the undoped thin film samples, the low temperature transport shows a small upturn before the resistivity saturates for all four superlattice samples. Although, it should be noted, transport in $LaNiO_3$ is found to be dominated by a p-type conduction channel so the electrons transferred may in-fact be reducing the carrier density. Further investigation, in particular Hall effect measurements, is worthwhile.

8.7 Summary

To summarise, the phase diagram of $Nd_{1-x}La_xNiO_3$ under tensile strain has begun to be mapped out. An unusual discontinuity in the metal-insulator transition temperature as a function of composition is seen at x = 0.2. We analysed the structure of the solid solution films, so far only obtained at room temperature, and discuss the possibility of an interesting phase crossover from $Pnma$ to $C2/c$. Perhaps due to the film symmetry, we find no $Nd_{1-x}La_xNiO_3$ films with a metal-insulator transition lower than 80 K. This obfuscates the 0 K incipient MIT around which we expected to find negative U physics and, eventually, a negative U-mediated superconducting state.

Future studies will be required to understand the complex structural phase diagram and, in doing this, it may become clear why the low temperature MIT appears to be blocked. In parallel, we will attempt to elucidate the possibility of superconductivity through, for instance, further electric field gating experiments, interfacial carrier doping or by ionic liquid gating.

Chapter 9

Conclusions and Perspectives

Transition metal oxides very often have rich phase diagrams owing to the comparable energy scales of the relevant microscopic interactions. Heterostructuring is one of the most tangible ways in which the correlated phases can be manipulated. Emerging from this fascinating intersection of oxide physics and thin film physics are often novel phenomena that can be turned into innovative functionalities. On the other side of the same coin, however, is the challenge in understanding the physics that governs these systems.

In this work, partly motivated by the possibility of finding a superconducting groundstate in nickelate heterostructures, we discussed interface-driven phenomena and strove to further understand the complexity therein.

This thesis focussed on heterostructures of the correlated oxide $LaNiO_3$, which were grown by radio frequency off-axis magnetron sputtering. Samples were then characterised primarily by x-ray diffraction, both in-house and with synchrotron light, electronic transport and magnetotransport, scanning transmission electron microscopy and Raman spectroscopy. These techniques together revealed the complex structures emerging from heterointerface-surface interactions and their correlation with electronic properties.

A technique to obtain the oxygen octahedral rotations of perovskites from simulating half integer Bragg peaks in x-ray diffraction was developed and used to trace the structural distortions of $LaNiO_3$ as a function of the total film thickness. A stark difference in behaviour was seen for different substrates, which is suggested to stem from more than just the lattice parameter mismatch. Appreciating how the film lattice distorts to accommodate heterostructuring, and how it often does so in a depth- and thickness-dependent way, will allow future heterostructure projects to be carried out with a greater reliability in the result. A further step could be to use the depth- and thickness-dependent structures in order to create a tailor-made functional oxide. The specification of the crystal structure could, for instance, be made by selecting the appropriate thickness of repeating layer in a superlattice.

With decreasing film thickness comes intriguing electronic behaviour. A series of $LaNiO_3$ films grown on $(001)_{pc}$-oriented $LaAlO_3$ substrate shows an enhancement in conductivity when the films are between 6 - 11 unit cells thick. This enhancement is proposed to manifest due to a complex interplay between multiple types of local structure in the films, an effect that is corroborated by both experimental and theoretical determinations of the atomically-resolved structure. Knowing that there is a thickness at which the metallicity is optimised has a great advantage in device fabrication where the conductivity is important. In the same study, we found that the ultrathin insulating regime of $LaNiO_3$ cannot be explained by a lattice-charge coupling alone. The origin of this state remains unknown but uncovering the underlying mechanism may prove invaluable in heterostructure engineering.

In an approach that does not necessarily involve heterostructure engineering as such, we describe the $Nd_{1-x}La_xNiO_3$ solid solution system in the context of superconductivity that is mediated by negative U centres. The first points on the phase diagram were mapped out through a systematic study of composition. The metal-insulator transition is found to discontinuously drop at around x = 0.2, behaviour that may derive from a blocked symmetry. The possibility of an intermediate structure between the two end compounds, as group theory would require, was also discussed.

With the purpose of searching for negative U physics, even if no composition with an incipient MIT was observed, electronic transport measurements were extended down to 30 mK, along with efforts to carrier dope. No superconducting ground state was observed in any of the samples measured, however.

The scope for future studies on $LaNiO_3$-based heterostructures is wide but some of the more pertinent avenues to follow from the work of this thesis are mentioned below.

On the $Nd_{1-x}La_xNiO_3$ solid solution side, the search for superconductivity has just begun. The idea that pairing may be enhanced in a thin film superconductor grown on a $Nd_{1-x}La_xNiO_3$ sample will be explored. Also, as just mentioned, investigating superconductivity along an orthogonal axis allowing doping at this special composition, for instance by field effect through ionic liquid gating, is an exciting route to follow.

Outside of the search for superconductivity, it remains to be determined how the $Nd_{1-x}La_xNiO_3$ structure makes the crossover from orthorhombic to rhombohedral, how this transition varies with temperature and whether or not it has any bearing on the electronic phase diagram.

Around the composition of $Nd_{1-x}La_xNiO_3$ where the insulating and metallic states are very close in energy, the material properties should be extremely sensitive to external stimuli and the heterostructure environment. On the latter, changing the orientation of epitaxial growth from $(001)_{pc}$ to $(111)_{pc}$ may establish a stronger interfacial structural coupling. With a well-selected substrate, it may be possible to transform a metal into an insulator simply by making this change in growth orientation, another promising research direction.

Finally, with the recent synthesis of high quality single crystal nickelates comes an opportunity to characterise these fascinating materials in a complementary way to polycrystalline and thin film samples. It may be that the nickelates still have some secrets waiting to be uncovered.

Acknowledgments

As is always the case, a thesis is produced not only by the person named on the front but also by the help, support and contribution of an almost uncountable number of people.

Naturally, the first acknowledgement must go to Prof. Jean-Marc Triscone who directed this project and was instrumental at each step. From him I have learned, of course, a tremendous amount about physics but also, and perhaps more importantly, the value of scientific integrity. I believe that I could not have found a better environment in which to carry out my thesis work than that of Jean Marc's group.

I was greatly honoured that my work was evaluated by such distinguished scientists so I wish to thank Prof. Charles Ahn, Prof. Antoine Georges and Prof. Phil Willmott for having agreed to serve as my thesis jury. I was lucky enough to have had the opportunity to discuss or collaborate with all three of them during my studies.

Over the last few years I have found myself working alongside many talented scientists and wonderful people.

I was first introduced to the fascinating field of oxides by Nick Plumb and Milan Radovic at the Paul Scherrer Institut and by Cliff Hicks and Andy MacKenzie in St Andrews so I owe a big thank you to them for helping me to discover this subject.

More recently, it has been wonderful to work as part of the "Nickelates Team" in Geneva. That is, Sara Catalano, Claribel Dominguez and Marta Gibert. Marta, in particular, deserves one of the biggest acknowledgements of all for going through my manuscript with a fine-tooth comb.

Anyone who has worked in the Triscone group knows that it is a special experience so thank you to all the group members, past and present, for the excursions and coffee breaks as well as the day-to-day work in the labs: Margherita Boselli, Joeri de Bruickere, Ritsuko Eguchi, Stéphanie Fernandez, Elías Ferreiro, Alexandre Fête, Stefano Gariglio, Dirk Groenendijk, Jorrit Hortensius, Denver Li, Céline Lichtensteiger, Wei Liu, Hugo Meley, Gernot Scheerer, Giulio Tieri, Davide Valentinis, Michel Viret, Adrien Waelchli, Christian Weymann, Zhenping Wu and Pavlo Zubko.

Specifically to this thesis there are a number of people to thank: Alex Schober, Mael Guennou, Jens Kreisel and Jorge Iñiguez helped us immensely in the work presented in chapter 7 and chapter 8 and the discussions we had during my visits to Luxembourg were enlightening. I will never forget the first time I saw an electron microscopy image of one of my samples and this new insight came from Giulio and his supervisors, Alexandre Gloter and Odile Stéphan, in Paris. A valuable addition to chapter 7 were the calculations performed by Alessio Filippetti, from whom I learned a great deal during our discussions on the paper. Chapter 6, on the other hand, was inspired by the work of Steve May and whenever I had a doubt or a question about my own studies he was more than willing to help me get things straightened out.

This thesis could not have been produced without samples and measurements so I really must thank Marco Lopes and Sébastien Muller for keeping the labs running!

The last word on the professional side should go to the people who made the organisation and administration of the thesis (including all five years!) much simpler for me; Denise Borjon, Nathalie Buret, Nathalie Chaduiron, Sandro D'Aleo, Elisabeth Giudicelli and Fabienne Hartmeier. Merci!

Outside of my academic world there is a whole host of characters who have supported me in one way or another and I although I cannot list all of them, I would like to thank a select few directly now.

Oliver. Thank you for understanding that sometimes I can't spend as much time with you as I, and you, would like. It was always nice, after a late night in the lab, to come home to my little furry friend waiting for me. Along similar lines, a I owe a huge debt of gratitude to Manoela and Rafael for looking after Olly when I had to go away, we couldn't have done this without you!

I know that I have been very fortunate and I can identify three parts to this:

The first part was from the moment I was born into a loving and supportive family. Thank you, then, to all of you - both in Scotland and further afield - but especially to my grandparents, Lex and Byrnece, my brother, Andrew and my parents, Bill and Susan and, of-course, Ruby. I'm only sorry I haven't been able to visit you more during these years.

The second part of my good fortune showed up in the many inspiring, patient and dedicated educators I have had over the years, from primary school up until graduate level. Among them there is one that stands out: my first physics teacher and good friend, Mr Caldwell. As I am sure you will be the only person to read this thesis for pleasure I thought it's only right to dedicate it to you!

Finally, the last third of my fortune is also the other - better - half of me. Philippe, you make life a joy and I love you.

Bibliography

[1] Roger H. Mitchell. *Perovskites: Modern and Ancient*. Almaz, 2003.

[2] Daniel I. Khomskii. *Transition Metal Compounds*. Cambridge University Press, 2014.

[3] A. M. Glazer. Simple ways of determining perovskite structures. *Acta Crystallogr. Sect. A*, 31(6):756–762, 1975.

[4] Christopher J. Howard and Harold T. Stokes. Group-theoretical analysis of octahedral tilting in perovskites. *Acta Crystallogr. Sect. B Struct. Sci.*, 54:782–789, 1998.

[5] J. B. Goodenough. Electronic and ionic transport properties and other physical aspects of perovskites. *Reports Prog. Phys.*, 67(11):1915–1993, 2004.

[6] D. P. Kozlenko, N. O. Golosova, Z. Jirák, L. S. Dubrovinsky, B. N. Savenko, M. G. Tucker, Y. Le Godec, and V. P. Glazkov. Temperature- and pressure-driven spin-state transitions in $LaCoO_3$. *Phys. Rev. B - Condens. Matter Mater. Phys.*, 75(6):1–10, 2007.

[7] Y Tokura and N. Nagaosa. Orbital Physics in Transition Metal Oxides. *Science (80-.).*, 288:462–468, 2000.

[8] John B. Goodenough and J.-S. Zhou. Orbital ordering in orthorhombic perovskites. *J. Mater. Chem.*, 17(23):2394, 2007.

[9] G. A. Sawatzky, W. Geertsma, and C. Haas. Magnetic interactions and covalency effects in mainly ionic compounds. *J. Magn. Magn. Mater.*, 3(1-2):37–45, 1976.

[10] Walter A. Harrison. *Electronic Structure and the Properties of Solids: The Physics of the Chemical Bond*. Dover Publications, 1990.

[11] Y. Okimoto, T. Katsufuji, Y. Okada, T. Arima, and Y. Tokura. Optical spectra in (La,Y)TiO_3: Variation of Mott-Hubbard gap features with change of electron correlation and band filling. *Phys. Rev. B*, 51(15):9581–9588, 1995.

[12] J. Zaanen, G. A. Sawatzky, and J. W. Allen. Band gaps and electronic structure of transition-metal compounds. *Phys. Rev. Lett.*, 55(4):418–421, 1985.

[13] T. Mizokawa, H. Namatame, A. Fujimori, K. Akeyama, H. Kondoh, H. Kuroda, and N. Kosugi. Origin of the band gap in the negative charge-transfer-energy compound $NaCuO_2$. *Phys. Rev. Lett.*, 67(12):1638–1641, 1991.

[14] Di Lu, David Baek, Seung Sae Hong, Lena F Kourkoutis, Yasuyuki Hikita, and Harold Y Hwang. Synthesis of freestanding single-crystal perovskite films and heterostructures by etching of sacrificial water-soluble layers. *Nat. Mater.*, 15:1255–1260, 2016.

[15] Pavlo Zubko, Stefano Gariglio, Marc Gabay, Philippe Ghosez, and Jean-Marc Triscone. Interface Physics in Complex Oxide Heterostructures. *Annu. Rev. Condens. Matter Phys.*, 2(1):141–165, 2011.

[16] H. Y. Hwang, Y. Iwasa, M. Kawasaki, B. Keimer, N. Nagaosa, and Y. Tokura. Emergent phenomena at oxide interfaces. *Nat. Mater.*, 11(2):103–113, 2012.

[17] Ulrich Aschauer, Reto Pfenninger, Sverre M. Selbach, Tor Grande, and Nicola A. Spaldin. Strain-controlled oxygen vacancy formation and ordering in $CaMnO_3$. *Phys. Rev. B - Condens. Matter Mater. Phys.*, 88(5):1–7, 2013.

[18] M. Gibert, M. Viret, A. Torres-Pardo, C. Piamonteze, P. Zubko, N. Jaouen, J. M. Tonnerre, A. Mougin, J. Fowlie, S. Catalano, A. Gloter, O. Stéphan, and J. M. Triscone. Interfacial Control of Magnetic Properties at $LaMnO_3$/$LaNiO_3$ Interfaces. *Nano Lett.*, 15(11):7355–7361, 2015.

[19] Ryotaro Aso, Daisuke Kan, Yuichi Shimakawa, and Hiroki Kurata. Atomic level observation of octahedral distortions at the perovskite oxide heterointerface. *Sci. Rep.*, 3:1–6, 2013.

[20] A. Vailionis, H. Boschker, Z. Liao, J. R.A. Smit, G. Rijnders, M. Huijben, and G. Koster. Symmetry and lattice mismatch induced strain accommodation near and away from correlated perovskite interfaces. *Appl. Phys. Lett.*, 105(13):0–5, 2014.

[21] Jacek Goniakowski, Fabio Finocchi, and Claudine Noguera. Polarity of oxide surfaces and nanostructures. *Reports Prog. Phys.*, 71(1):016501, 2008.

[22] A Ohtomo and H Y Hwang. A high-mobility electron gas at the LAO/STO heterointerface. *Nature*, 427(6973):423–426, 2004.

[23] N Reyren, S Thiel, A D Caviglia, L Fitting Kourkoutis, G Hammerl, C Richter, C W Schneider, T Kopp, A.-S. Ruetschi, D Jaccard, M. Gabay, D A Muller, J-M Triscone, and J Mannhart. Superconducting interfaces between insulating oxides. *Science (80-.).*, 317(August):1196–1199, 2007.

[24] X. Renshaw Wang, C. J. Li, W. M. Lü, T. R. Paudel, D. P. Leusink, M. Hoek, N. Poccia, A. Vailionis, T. Venkatesan, J. M. D. Coey, E. Y. Tsymbal, Ariando, and H. Hilgenkamp. Imaging and control of ferromagnetism in $LaMnO_3/SrTiO_3$ heterostructures. *Science (80-.).*, 349(6249):716–719, 2015.

[25] J Mannhart and D G Schlom. Oxide Interfaces—An Opportunity for Electronics. *Science (80-.).*, 327(5973):1607 LP – 1611, 2010.

[26] Pu Yu, Ying Hao Chu, and Ramamoorthy Ramesh. Oxide interfaces: Pathways to novel phenomena. *Mater. Today*, 15(7-8):320–327, 2012.

[27] J.H. Ngai, F.J. Walker, and C.H. Ahn. Correlated Oxide Physics and Electronics. *Annu. Rev. Mater. Res.*, 44(1):1–17, 2014.

[28] Kourosh Kalantar-zadeh, Jian Zhen Ou, Torben Daeneke, Arnan Mitchell, Takayoshi Sasaki, and Michael S. Fuhrer. Two dimensional and layered transition metal oxides. *Appl. Mater. Today*, 5:73–89, 2016.

[29] M Lorenz, M S Ramachandra Rao, T Venkatesan, E Fortunato, P Barquinha, R Branquinho, D Salgueiro, R Martins, E Carlos, A Liu, F K Shan, M Grundmann, H Boschker, J Mukherjee, M Priyadarshini, N DasGupta, D J Rogers, F H Teherani, E V Sandana, P Bove, K Rietwyk, A Zaban, A Veziridis, A Weidenkaff, M Muralidhar, M Murakami, S Abel, J Fompeyrine, J Zuniga-Perez, R Ramesh, N A Spaldin, S Ostanin, V Borisov, I Mertig, V Lazenka, G Srinivasan, W Prellier, M Uchida, M Kawasaki, R Pentcheva, P Gegenwart, F Miletto Granozio, J Fontcuberta, and N Pryds. The 2016 oxide electronic materials and oxide interfaces roadmap. *J. Phys. D. Appl. Phys.*, 49(43):433001, 2016.

[30] J. B. Torrance, P. Lacorre, A. I. Nazzal, E. J. Ansaldo, and Ch Niedermayer. Systematic study of insulator-metal transitions in perovskites $RNiO_3$ (R=Pr,Nd,Sm,Eu) due to closing of charge-transfer gap. *Phys. Rev. B*, 45(14):8209–8212, 1992.

[31] M Medarde. Structural , magnetic and electronic properties of $RNiO_3$ perovskites (R = rare earth). *J. Phys, Condens. Matter*, 9:1679–1707, 1997.

[32] G. Catalan. Progress in perovskite nickelate research. *Phase Transitions*, 81(7-8):729–749, 2008.

[33] H. Guo, Z. W. Li, L. Zhao, Z. Hu, C. F. Chang, C. Y. Kuo, W. Schmidt, A. Piovano, T. W. Pi, O. Sobolev, D. I. Khomskii, L. H. Tjeng, and A. C. Komarek. Antiferromagnetic correlations in the metallic strongly correlated transition metal oxide $LaNiO_3$. *Nat. Commun.*, 9(1), 2018.

[34] T Mizokawa, D I Khomskii, and G a Sawatzky. Spin and charge ordering in self-doped Mott insulators. *Phys. Rev. B*, 61(17):4, 2000.

[35] Valentina Bisogni, Sara Catalano, Robert J. Green, Marta Gibert, Raoul Scherwitzl, Yaobo Huang, Vladimir N. Strocov, Pavlo Zubko, Shadi Balandeh, Jean Marc Triscone, George Sawatzky, and Thorsten Schmitt. Ground-state oxygen holes and the metal-insulator transition in the negative charge-transfer rare-earth nickelates. *Nat. Commun.*, 7:1–8, 2016.

[36] Jiří Chaloupka and Giniyat Khaliullin. Orbital order and possible superconductivity in $LaNiO_3/LaMO_3$ superlattices. *Phys. Rev. Lett.*, 100(1):3–6, 2008.

[37] I. I. Mazin, D. I. Khomskii, R. Lengsdorf, J. A. Alonso, W. G. Marshall, R. M. Ibberson, A. Podlesnyak, M. J. Martínez-Lope, and M. M. Abd-Elmeguid. Charge ordering as alternative to Jahn-Teller distortion. *Phys. Rev. Lett.*, 98(17):1–4, 2007.

[38] Hyowon Park, Andrew J. Millis, and Chris A. Marianetti. Site-selective Mott transition in rare-earth-element nickelates. *Phys. Rev. Lett.*, 109(15):1–5, 2012.

[39] Steve Johnston, Anamitra Mukherjee, Ilya Elfimov, Mona Berciu, and George A. Sawatzky. Charge disproportionation without charge transfer in the rare-earth-element nickelates as a possible mechanism for the metal-insulator transition. *Phys. Rev. Lett.*, 112(10), 2014.

[40] Alaska Subedi, Oleg E. Peil, and Antoine Georges. Low-energy description of the metal-insulator transition in the rare-earth nickelates. *Phys. Rev. B - Condens. Matter Mater. Phys.*, 91(7):1–16, 2015.

[41] Julien Varignon, Mathieu N. Grisolia, Jorge Íñiguez, Agnès Barthélémy, and Manuel Bibes. Reconciling the ionic and covalent pictures in rare-earth nickelates. *npj Quantum Mater.*, 2:21:1–8, 2017.

[42] R. J. Green, M. W. Haverkort, and G. A. Sawatzky. Bond disproportionation and dynamical charge fluctuations in the perovskite rare-earth nickelates. *Phys. Rev. B*, 94(19):1–5, 2016.

[43] Alain Mercy, Jordan Bieder, Jorge Íñiguez, and Philippe Ghosez. Structurally triggered metal-insulator transition in rare-earth nickelates. *Nat. Commun.*, 8(1):1–6, 2017.

[44] J. Ruppen, J. Teyssier, I. Ardizzone, O. E. Peil, S. Catalano, M. Gibert, J. M. Triscone, A. Georges, and D. Van Der Marel. Impact of antiferromagnetism on the optical properties of rare-earth nickelates. *Phys. Rev. B*, 96(4):1–5, 2017.

[45] U. Staub, G. I. Meijer, F. Fauth, R. Allenspach, J. G. Bednorz, J. Karpinski, S. M. Kazakov, L. Paolasini, and F. D'Acapito. Direct Observation of Charge Order in an Epitaxial $NdNiO_3$Film. *Phys. Rev. Lett.*, 88(12):4, 2002.

[46] X. Obradors, L. M. Paulius, M. B. Maple, J. B. Torrance, A. I. Nazzal, J. Fontcuberta, and X. Granados. Pressure dependence of the metal-insulator transition in the charge-transfer oxides $RNiO_3$ (R=Pr,Nd,$Nd_{0.7}La_{0.3}$). *Phys. Rev. B*, 47(18):12353–12356, 1993.

[47] A. D. Caviglia, R. Scherwitzl, P. Popovich, W. Hu, H. Bromberger, R. Singla, M. Mitrano, M. C. Hoffmann, S. Kaiser, P. Zubko, S. Gariglio, J. M. Triscone, M. Först, and A. Cavalleri. Ultrafast strain engineering in complex oxide heterostructures. *Phys. Rev. Lett.*, 108(13), 2012.

[48] M. Medarde, P. Lacorre, K. Conder, F. Fauth, and A. Furrer. Giant ^{16}O-^{18}O Isotope Effect on the Metal-Insulator Transition of $RNiO_3$ Perovskites (R=Rare Earth). *Phys. Rev. Lett.*, 80:2397–2400, 1998.

[49] Ashutosh Tiwari, C. Jin, and J. Narayan. Strain-induced tuning of metal-insulator transition in $NdNiO_3$. *Appl. Phys. Lett.*, 80(21):4039–4041, 2002.

[50] Jian Liu, M. Kareev, B. Gray, J. W. Kim, P. Ryan, B. Dabrowski, J. W. Freeland, and J. Chakhalian. Strain-mediated metal-insulator transition in epitaxial ultrathin films of $NdNiO_3$. *Appl. Phys. Lett.*, 96(23):1–4, 2010.

[51] S. Catalano, M. Gibert, V. Bisogni, O. E. Peil, F. He, R. Sutarto, M. Viret, P. Zubko, R. Scherwitzl, A. Georges, G. A. Sawatzky, T. Schmitt, and J. M. Triscone. Electronic transitions in strained $SmNiO_3$ thin films. *APL Mater.*, 2(11):2–9, 2014.

[52] Adam J. Hauser, Evgeny Mikheev, Nelson E. Moreno, Jinwoo Hwang, Jack Y. Zhang, and Susanne Stemmer. Correlation between stoichiometry, strain, and metal-insulator transitions of $NdNiO_3$ films. *Appl. Phys. Lett.*, 106(9), 2015.

[53] S. Catalano, M. Gibert, V. Bisogni, F. He, R. Sutarto, M. Viret, P. Zubko, R. Scherwitzl, G. A. Sawatzky, T. Schmitt, and J.-M. Triscone. Tailoring the electronic transitions of $NdNiO_3$ films through $(111)_{pc}$ oriented interfaces. *APL Mater.*, 3(6):062506, 2015.

[54] J. L García-Muñoz, J Rodríguez-Carvajal, and P Lacorre. Sudden Appearance of an Unusual Spin Density Wave At the Metal-Insulator Transition in the Perovskites $RNiO_3$ (R = Pr, Nd). *Europhys. Lett.*, 20(3):241–247, 1992.

[55] V. Scagnoli, U. Staub, A. M. Mulders, M. Janousch, G. I. Meijer, G. Hammerl, J. M. Tonnerre, and N. Stojic. Role of magnetic and orbital ordering at the metal-insulator transition in $NdNiO_3$. *Phys. Rev. B - Condens. Matter Mater. Phys.*, 73(10):1–4, 2006.

[56] S Catalano, M Gibert, J Fowlie, J Íñiguez, and J.-M. Triscone. Rare-earth nickelates $RNiO_3$: thin films and heterostructures. *Reports Prog. Phys.*, 2018.

[57] Junjie Zhang, Hong Zheng, Yang Ren, and J. F. Mitchell. High-Pressure Floating-Zone Growth of Perovskite Nickelate $LaNiO_3$ Single Crystals. *Cryst. Growth Des.*, 17(5):2730–2735, 2017.

[58] S. T. Zhang, X. J. Zhang, H. W. Cheng, Y. F. Chen, Z. G. Liu, N. B. Ming, X. B. Hu, and J. Y. Wang. Enhanced electrical properties of c -axis epitaxial Nd-substituted $Bi_4Ti_3O_{12}$ thin films. *Appl. Phys. Lett.*, 83(21):4378–4380, 2003.

[59] Kyunghoon Kim, M. Paranthaman, D. P. Norton, T. Aytug, C. Cantoni, A. A. Gapud, A. Goyal, and D. K. Christen. A perspective on conducting oxide buffers for Cu-based YBCO-coated conductors. *Supercond. Sci. Technol.*, 19(4), 2006.

[60] Flavio Y. Bruno, Sören Boyn, Stéphane Fusil, Stéphanie Girod, Cécile Carrétéro, Maya Marinova, Alexandre Gloter, Stéphane Xavier, Cyrile Deranlot, Manuel Bibes, Agnès Barthélémy, and Vincent Garcia. Millionfold Resistance Change in Ferroelectric Tunnel Junctions Based on Nickelate Electrodes. *Adv. Electron. Mater.*, 2(3):1500245, 2016.

[61] Jian Zhang, Yubao Zhao, Xiao Zhao, Zhaolin Liu, and Wei Chen. Porous perovskite $LaNiO_3$ nanocubes as cathode catalysts for Li-O_2 batteries with low charge potential. *Sci. Rep.*, 4:2–7, 2014.

[62] Feng Hou, Yongning Qin, Tingxian Xu, and Mingxia Xu. Study on Oxygen-Sensing Properties of $LaNiO_3$ Thin Films. *J. Electroceramics*, pages 243–247, 2002.

[63] Bi-Xia Wang, S. Rosenkranz, X. Rui, Junjie Zhang, F. Ye, H. Zheng, R. F. Klie, J. F. Mitchell, and D. Phelan. Antiferromagnetic defect structure in $LaNiO_{3-\delta}$ single crystals. *Phys. Rev. Mater.*, 2(6):064404, 2018.

[64] Shuai Dong and Elbio Dagotto. Quantum confinement induced magnetism in $LaNiO_3$-$LaMnO_3$ superlattices. *Phys. Rev. B - Condens. Matter Mater. Phys.*, 87(19):1–7, 2013.

[65] J. Hoffman, I. C. Tung, B. B. Nelson-Cheeseman, M. Liu, J. W. Freeland, and A. Bhattacharya. Charge transfer and interfacial magnetism in $(LaNiO_3)_n/(LaMnO_3)_2$ superlattices. *Phys. Rev. B*, 88(14):144411, 2013.

[66] Jason D. Hoffman, Brian J. Kirby, Jihwan Kwon, Gilberto Fabbris, D. Meyers, John W. Freeland, Ivar Martin, Olle G. Heinonen, Paul Steadman, Hua Zhou, Christian M. Schlepütz, Mark P.M. Dean, Suzanne G.E. te Velthuis, Jian Min Zuo, and Anand Bhattacharya. Oscillatory noncollinear magnetism induced by interfacial charge transfer in superlattices composed of metallic oxides. *Phys. Rev. X*, 6(4):1–9, 2016.

[67] A V Boris, Y Matiks, E Benckiser, A Frano, P Popovich, V Hinkov, P Wochner, E Detemple, V K Malik, C Bernhard, T Prokscha, A Suter, Z Salman, E Morenzoni, G Cristiani, H Habermeier, and B Keimer. Dimensionality Control of Electronic Phase Transitions in Nickel-Oxide Superlattices. *Science (80-.).*, 332(May):937–941, 2011.

[68] A. Frano, E. Schierle, M. W. Haverkort, Y. Lu, M. Wu, S. Blanco-Canosa, U. Nwankwo, A. V. Boris, P. Wochner, G. Cristiani, H. U. Habermeier, G. Logvenov, V. Hinkov, E. Benckiser, E. Weschke, and B. Keimer. Orbital control of noncollinear magnetic order in nickel oxide heterostructures. *Phys. Rev. Lett.*, 111(10):3–7, 2013.

[69] M Gibert, M Viret, P Zubko, N Jaouen, J M Tonnerre, A Torres-Pardo, S Catalano, A Gloter, O Stephan, and J M Triscone. Interlayer coupling through a dimensionality-induced magnetic state. *Nat. Commun.*, 7:11227, 2016.

[70] J. G. Bednorz and K. A. Müller. Possible High T c Superconductivity in the Ba — La — Cu — O System. *Zeitschrift für Phys. B Condens. Matter*, 193:267–271, 1986.

[71] P. Hansmann, Xiaoping Yang, A. Toschi, G. Khaliullin, O. K. Andersen, and K. Held. Turning a Nickelate Fermi Surface into a Cupratelike One through Heterostructuring. *Phys. Rev. Lett.*, 103(1):1–4, 2009.

[72] P. Hansmann, A. Toschi, Xiaoping Yang, O. K. Andersen, and K. Held. Electronic structure of nickelates: From two-dimensional heterostructures to three-dimensional bulk materials. *Phys. Rev. B - Condens. Matter Mater. Phys.*, 82(23):10–17, 2010.

[73] Eva Benckiser, Maurits W. Haverkort, Sebastian Brück, Eberhard Goering, Sebastian MacKe, Alex Frañ, Xiaoping Yang, Ole K. Andersen, Georg Cristiani, Hanns Ulrich Habermeier, Alexander V. Boris, Ioannis Zegkinoglou, Peter Wochner, Heon Jung Kim, Vladimir Hinkov, and Bernhard Keimer. Orbital reflectometry of oxide heterostructures. *Nat. Mater.*, 10(3):189–193, 2011.

[74] M. Wu, E. Benckiser, M. W. Haverkort, A. Frano, Y. Lu, U. Nwankwo, S. Brück, P. Audehm, E. Goering, S. Macke, V. Hinkov, P. Wochner, G. Christiani, S. Heinze, G. Logvenov, H. U. Habermeier, and B. Keimer. Strain and composition dependence of orbital polarization in nickel oxide superlattices. *Phys. Rev. B - Condens. Matter Mater. Phys.*, 88(12):1–9, 2013.

[75] Ankit S. Disa, Divine P. Kumah, Andrei Malashevich, Hanghui Chen, Dario A. Arena, Eliot D. Specht, Sohrab Ismail-Beigi, F. J. Walker, and Charles H. Ahn. Orbital engineering in symmetry-breaking polar heterostructures. *Phys. Rev. Lett.*, 114(2):1–6, 2015.

[76] S. J. May, J. W. Kim, J. M. Rondinelli, E. Karapetrova, N. A. Spaldin, A. Bhattacharya, and P. J. Ryan. Quantifying octahedral rotations in strained perovskite oxide films. *Phys. Rev. B - Condens. Matter Mater. Phys.*, 82(1):1–7, 2010.

[77] Hanghui Chen, Andrew J. Millis, and Chris a. Marianetti. Engineering Correlation Effects via Artificially Designed Oxide Superlattices. *Phys. Rev. Lett.*, 111(11):116403, 2013.

[78] Hanghui Chen, Divine P. Kumah, Ankit S. Disa, Frederick J. Walker, Charles H. Ahn, and Sohrab Ismail-Beigi. Modifying the Electronic Orbitals of Nickelate Heterostructures via Structural Distortions. *Phys. Rev. Lett.*, 110(18):186402, 2013.

[79] M. J. Han, Xin Wang, C. A. Marianetti, and A. J. Millis. Dynamical mean-field theory of nickelate superlattices. *Phys. Rev. Lett.*, 107(20):1–5, 2011.

[80] Oleg E. Peil, Michel Ferrero, and Antoine Georges. Orbital polarization in strained $LaNiO_3$: Structural distortions and correlation effects. *Phys. Rev. B - Condens. Matter Mater. Phys.*, 90(4):1–12, 2014.

[81] G. Fabbris, D. Meyers, J. Okamoto, J. Pelliciari, A. S. Disa, Y. Huang, Z. Y. Chen, W. B. Wu, C. T. Chen, S. Ismail-Beigi, C. H. Ahn, F. J. Walker, D. J. Huang, T. Schmitt, and M. P.M. Dean. Orbital Engineering in Nickelate Heterostructures Driven by Anisotropic Oxygen Hybridization rather than Orbital Energy Levels. *Phys. Rev. Lett.*, 117(14):1–6, 2016.

[82] S. Middey, J. Chakhalian, P. Mahadevan, J. W. Freeland, A. J. Millis, and D. D. Sarma. Physics of ultrathin films and heterostructures of rare earth nickelates. *Annu. Rev. Mater. Res.*, 46:305–334, 2016.

[83] Donald Smith. *Thin Film Deposition: Principles and Practice*. McGraw-Hill, 1995.

[84] C.B. Eom, J.Z. Sun, B.M. Lairson, S.K. Streiffer, A.F. Marshall, K. Yamamoto, S.M. Anlage, J.C. Bravman, T.H. Geballe, S.S. Laderman, R.C. Taber, and R.D. Jacowitz. Synthesis and properties of $YBa_2Cu_3O_7$ thin films grown in situ by 90 degree off-axis single magnetron sputtering. *Phys. C Supercond.*, 171(3-4):354–383, 1990.

[85] Karin Rabe, Charles H. Ahn, and J.M. Triscone. *Physics of Ferroelectrics, A Modern Perspective*. Springer, 2007.

[86] L. Fàbrega, E. Koller, J. M. Triscone, and Ø. Fischer. Epitaxial growth of "infinite layer" thin films and multilayers by rf magnetron sputtering. *J. Mater. Res.*, 13(08):2195–2201, 1998.

[87] John A. Thornton. Magnetron sputtering: basic physics and application to cylindrical magnetrons. *J. Vac. Sci. Technol.*, 15(2):171–177, 1978.

[88] J. P. Podkaminer, J. J. Patzner, B. A. Davidson, and C. B. Eom. Real-time and in situ monitoring of sputter deposition with RHEED for atomic layer controlled growth. *APL Mater.*, 4(8), 2016.

[89] Nader Jalili and Karthik Laxminarayana. A review of atomic force microscopy imaging systems: Application to molecular metrology and biological sciences. *Mechatronics*, 14(8):907–945, 2004.

[90] Jens Als-Nielsen and Des McMorrow. *Elements of Modern X-ray Physics*. Wiley, 2nd edition, 2011.

[91] Vitalij Pecharsky and Peter Zavalij. *Fundamentals of Powder Diffraction and Structural Characterization of Materials*. Springer, 2nd edition, 2009.

[92] Philip Willmott. *An Introduction to Synchrotron Radiation: Techniques and Applications*. Wiley, 2011.

[93] J. P. Hill and D. F. McMorrow. X-ray Resonant Exchange Scattering: Polarization Dependence and Correlation Function. *Acta Crystallogr. Sect. A Found. Crystallogr.*, 52(2):236–244, 1996.

[94] J. L. Olsen. *Electron Transport in Metals*. Interscience, Wiley, 1962.

[95] N.W. Ashcroft and N.D. Mermin. *Solid State Physics*. Rinehart and Winston, 1976.

[96] L van der Pauw. A Method of Measuring the Resistivity and Hall Coefficient on Lamellae of Arbitrary Shape. *Phillips Tech. Rev.*, 20:220, 1958.

[97] C V Raman and K S Krishnan. A New Type of Secondary Radiation. *Nature*, 121:501, 1928.

[98] Rajinder Singh. C. V. Raman and the Discovery of the Raman Effect. *Phys. Perspect.*, 4(4):399–420, 2002.

[99] C H Perry, Jeanne H Fertel, and T F McNelly. Temperature Dependence of the Raman Spectrum of $SrTiO_3$ and $KTaO_3$. *J. Chem. Phys.*, 47(5):1619–1625, 1967.

[100] J F Scott. Soft-mode spectroscopy: Experimental studies of structural phase transitions. *Rev. Mod. Phys.*, 1974.

[101] D A Tenne, A Bruchhausen, N D Lanzillotti-Kimura, A Fainstein, R S Katiyar, A Cantarero, A Soukiassian, V Vaithyanathan, J H Haeni, W Tian, D G Schlom, K J Choi, D M Kim, C B Eom, H P Sun, X Q Pan, Y L Li, L Q Chen, Q X Jia, S M Nakhmanson, K M Rabe, and X X Xi. Probing Nanoscale Ferroelectricity by Ultraviolet Raman Spectroscopy. *Science (80-.).*, 313(5793):1614–1616, 2006.

[102] Olinde Rodrigues. Des lois géometriques qui regissent les déplacements d' un systéme solide dans l' espace, et de la variation des coordonnées provenant de ces déplacement considérées indépendant des causes qui peuvent les produire. *J. Math. Pures. Appl.*, 5:380 – 440, 1840.

[103] P. R. Willmott, D. Meister, S. J. Leake, M. Lange, A. Bergamaschi, M. Böge, M. Calvi, C. Cancellieri, N. Casati, A. Cervellino, Q. Chen, C. David, U. Flechsig, F. Gozzo, B. Henrich, S. Jäggi-Spielmann, B. Jakob, I. Kalichava, P. Karvinen, J. Krempasky, A. Lüdeke, R. Lüscher, S. Maag, C. Quitmann, M. L. Reinle-Schmitt, T. Schmidt, B. Schmitt, A. Streun, I. Vartiainen, M. Vitins, X. Wang, and R. Wullschleger. The Materials Science beamline upgrade at the Swiss Light Source. *J. Synchrotron Radiat.*, 20(5):667–682, 2013.

[104] H. Rotella, U. Lüders, P.-E. Janolin, V. H. Dao, D. Chateigner, R. Feyerherm, E. Dudzik, and W. Prellier. Octahedral tilting in strained $LaVO_3$ thin films. *Phys. Rev. B*, 85(18):184101, 2012.

[105] R. L. Johnson-Wilke, D. Marincel, S. Zhu, M. P. Warusawithana, A. Hatt, J. Sayre, K. T. Delaney, R. Engel-Herbert, C. M. Schlepütz, J.-W. Kim, V. Gopalan, N. a. Spaldin, D. G. Schlom, P. J. Ryan, and S. Trolier-McKinstry. Quantification of octahedral rotations in strained $LaAlO_3$ films via synchrotron x-ray diffraction. *Phys. Rev. B*, 88(17):174101, 2013.

[106] Daisuke Kan, Yusuke Wakabayashi, Hiroo Tajiri, and Yuichi Shimakawa. Interfacially engineered oxygen octahedral rotations and their impact on strain relief in coherently grown $SrRuO_3$ films. *Phys. Rev. B*, 94(2):1–6, 2016.

[107] S. J. May, C. R. Smith, J. W. Kim, E. Karapetrova, A. Bhattacharya, and P. J. Ryan. Control of octahedral rotations in $(LaNiO_3)_n/$ $(SrMnO_3)_m$ superlattices. *Phys. Rev. B - Condens. Matter Mater. Phys.*, 83(15):2–5, 2011.

[108] M. Brahlek, A. K. Choquette, C. R. Smith, R. Engel-Herbert, and S. J. May. Structural refinement of Pbnm -type perovskite films from analysis of half-order diffraction peaks. *J. Appl. Phys.*, 121(4), 2017.

[109] Yizhak Yacoby, Mukhles Sowwan, Edward Stern, Julie O Cross, Dale Brewe, Ron Pindak, John Pitney, Eric M Dufresne, and Roy Clarke. Direct determination of epitaxial interface structure in Gd_2O_3 passivation of GaAs. *Nat. Mater.*, 1:99–101, 2002.

[110] P. R. Willmott, S. A. Pauli, R. Herger, C. M. Schlepütz, D. Martoccia, B. D. Patterson, B. Delley, R. Clarke, D. Kumah, C. Cionca, and Y. Yacoby. Structural basis for the conducting interface between $LaAlO_3$ and $SrTiO_3$. *Phys. Rev. Lett.*, 99(15):1–4, 2007.

[111] D. P. Kumah, Y. Yacoby, S. A. Pauli, P. R. Willmott, and R. Clarke. La-doped $BaTiO_3$ heterostructures: Compensating the polarization discontinuity. *APL Mater.*, 1(6):062107, 2013.

[112] Divine P. Kumah, Andrei Malashevich, Ankit S. Disa, Dario A. Arena, Frederick J. Walker, Sohrab Ismail-Beigi, and Charles H. Ahn. Effect of surface termination on the electronic properties of $LaNiO_3$ films. *Phys. Rev. Appl.*, 2(5):1–7, 2014.

[113] T. T. Fister, H. Zhou, Z. Luo, S. S. A. Seo, S. O. Hruszkewycz, D. L. Proffit, J. A. Eastman, P. H. Fuoss, P. M. Baldo, H. N. Lee, and D. D. Fong. Octahedral rotations in strained $LaAlO_3/SrTiO_3$ (001) heterostructures. *APL Mater.*, 2(2):021102, 2014.

[114] S. Koohfar, A. S. Disa, M. S.J. Marshall, F. J. Walker, C. H. Ahn, and D. P. Kumah. Structural distortions at polar manganite interfaces. *Phys. Rev. B*, 96(2):6–11, 2017.

[115] M. K. Kinyanjui, Y. Lu, N. Gauquelin, M. Wu, A. Frano, P. Wochner, M. Reehuis, G. Christiani, G. Logvenov, H. U. Habermeier, G. A. Botton, U. Kaiser, B. Keimer, and E. Benckiser. Lattice distortions and octahedral rotations in epitaxially strained $LaNiO_3/LaAlO_3$ superlattices. *Appl. Phys. Lett.*, 104(22):3–7, 2014.

[116] Christopher J. Howard and Harold T. Stokes. Structures and phase transitions in perovskites–a group-theoretical approach. *Acta Crystallogr. A.*, 61(Pt 1):93–111, 2005.

[117] James M. Rondinelli and Nicola A. Spaldin. Substrate coherency driven octahedral rotations in perovskite oxide films. *Phys. Rev. B - Condens. Matter Mater. Phys.*, 82, 2010.

[118] James M. Rondinelli, Steven J. May, and John W. Freeland. Control of octahedral connectivity in perovskite oxide heterostructures: An emerging route to multifunctional materials discovery. *MRS Bull.*, 37(03):261–270, 2012.

[119] Mohammad A Islam, James M Rondinelli, and Jonathan E Spanier. Normal mode determination of perovskite crystal structures with octahedral rotations: theory and applications. *J. Phys. Condens. Matter*, 25(17):175902, 2013.

[120] Prasanna V. Balachandran and James M. Rondinelli. Interplay of octahedral rotations and breathing distortions in charge-ordering perovskite oxides. *Phys. Rev. B - Condens. Matter Mater. Phys.*, 88, 2013.

[121] A. Y. Borisevich, H. J. Chang, M. Huijben, M. P. Oxley, S. Okamoto, M. K. Niranjan, J. D. Burton, E. Y. Tsymbal, Y. H. Chu, P. Yu, R. Ramesh, S. V. Kalinin, and S. J. Pennycook. Suppression of octahedral tilts and associated changes in electronic properties at epitaxial oxide heterostructure interfaces. *Phys. Rev. Lett.*, 105(8):1–4, 2010.

[122] J. Gazquez, M. Stengel, R. Mishra, M. Scigaj, M. Varela, M. A. Roldan, J. Fontcuberta, F. Sánchez, and G. Herranz. Competition between Polar and Nonpolar Lattice Distortions in Oxide Quantum Wells: New Critical Thickness at Polar Interfaces. *Phys. Rev. Lett.*, 119(10):1–6, 2017.

[123] J. L. García-Muñoz, J. Rodríguez-Carvajal, P. Lacorre, and J. B. Torrance. Neutron-diffraction study of R <math display="inline"> <mrow> <msub> <mrow> <mi mathvariant="normal">NiO</mi> </mrow> <mrow> <mn>3</mn> </mrow> </msub> </mrow> </math> (R =La,Pr,Nd,Sm): Electronically induced structural changes across the m. *Phys. Rev. B*, 46(8):4414–4425, 1992.

[124] K. A. Müller, W. Berlinger, and F. Waldner. Characteristic structural phase transition in perovskite-type compounds. *Phys. Rev. Lett.*, 21(12):814–817, 1968.

[125] Alison J. Hatt and Nicola A. Spaldin. Structural phases of strained $LaAlO_3$ driven by octahedral tilt instabilities. *Phys. Rev. B - Condens. Matter Mater. Phys.*, 82(19):1–5, 2010.

[126] R. Scherwitzl, P. Zubko, C. Lichtensteiger, and J. M. Triscone. Electric-field tuning of the metal-insulator transition in ultrathin films of $LaNiO_3$. *Appl. Phys. Lett.*, 95(22):1–4, 2009.

[127] Junwoo Son, Pouya Moetakef, James M. Lebeau, Daniel Ouellette, Leon Balents, S. James Allen, and Susanne Stemmer. Low-dimensional Mott material: Transport in ultrathin epitaxial $LaNiO_3$ films. *Appl. Phys. Lett.*, 96(6):1–4, 2010.

[128] R. Scherwitzl, S. Gariglio, M. Gabay, P. Zubko, M. Gibert, and J. M. Triscone. Metal-insulator transition in ultrathin $LaNiO_3$ films. *Phys. Rev. Lett.*, 106(24):3–6, 2011.

[129] P. D.C. King, H. I. Wei, Y. F. Nie, M. Uchida, C. Adamo, S. Zhu, X. He, I. Božović, D. G. Schlom, and K. M. Shen. Atomic-scale control of competing electronic phases in ultrathin $LaNiO_3$. *Nat. Nanotechnol.*, 9(6):443–447, 2014.

[130] Hyang Keun Yoo, Seung Ill Hyun, Young Jun Chang, Luca Moreschini, Chang Hee Sohn, Hyeong Do Kim, Aaron Bostwick, Eli Rotenberg, Ji Hoon Shim, and Tae Won Noh. Thickness-dependent electronic structure in ultrathin $LaNiO_3$ films under tensile strain. *Phys. Rev. B*, 93(3):1–7, 2016.

[131] Jennifer Fowlie, Marta Gibert, Giulio Tieri, Alexandre Gloter, Jorge Íñiguez, Alessio Filippetti, Sara Catalano, Stefano Gariglio, Alexander Schober, Mael Guennou, Jens Kreisel, Odile Stéphan, and Jean Marc Triscone. Conductivity and Local Structure of $LaNiO_3$ Thin Films. *Adv. Mater.*, 29(18):1–5, 2017.

[132] Piers Coleman. *Introduction to Many-Body Physics*. Cambridge University Press, 2016.

[133] Divine P. Kumah, Ankit S. Disa, Joseph H. Ngai, Hanghui Chen, Andrei Malashevich, James W. Reiner, Sohrab Ismail-Beigi, Frederick J. Walker, and Charles H. Ahn. Tuning the structure of nickelates to achieve two-dimensional electron conduction. *Adv. Mater.*, 26(12):1935–1940, 2014.

[134] M. Hepting, D. Kukuruznyak, E. Benckiser, M. Le Tacon, and B. Keimer. Raman light scattering on ultra-thin films of $LaNiO_3$ under compressive strain. *Phys. B Condens. Matter*, 460:196–198, 2015.

[135] Alexander Schober, Mael Guennou, Mads C. Weber, Hongjian Zhao, Jorge Íñiguez, Jennifer Fowlie, Marta Gibert, Sara Catalano, Jean-Marc Triscone, and Jens Kreisel. Octahedra soft modes in ultrathin perovskite films. *Unpublished*, 2018.

[136] Gaoyang Gou, Ilya Grinberg, Andrew M. Rappe, and James M. Rondinelli. Lattice normal modes and electronic properties of the correlated metal $LaNiO_3$. *Phys. Rev. B - Condens. Matter Mater. Phys.*, 84(14):1–13, 2011.

[137] G. Kresse and J. Furthmüller. Efficient iterative schemes for ab initio total-energy calculations using a plane-wave basis set. *Phys. Rev. B - Condens. Matter Mater. Phys.*, 54(16):11169–11186, 1996.

[138] Georg K.H. Madsen and David J. Singh. BoltzTraP. A code for calculating band-structure dependent quantities. *Comput. Phys. Commun.*, 175(1):67–71, 2006.

[139] E. J. Moon, P. V. Balachandran, B. J. Kirby, D. J. Keavney, R. J. Sichel-Tissot, C. M. Schlepütz, E. Karapetrova, X. M. Cheng, J. M. Rondinelli, and S. J. May. Effect of interfacial octahedral behavior in ultrathin manganite films. *Nano Lett.*, 14(5), 2014.

[140] S. R. Barman, A. Chainani, and D. D. Sarma. Covalency-driven unusual metal-insulator transition in nickelates. *Phys. Rev. B*, 49(12):8475–8478, 1994.

[141] A.W. Sleight, J.L. Gillson, and P.E. Bierstedt. High-temperature superconductivity in the $BaPb_{1-x}Bi_xO_3$ systems. *Solid State Commun.*, 17(1):27–28, 1975.

[142] D.E. Cox and A.W. Sleight. Crystal structure of $Ba_2Bi^{3+}Bi^{5+}O_6$. *Solid State Commun.*, 19(10):969–973, 1976.

[143] C. M. Varma. Missing valence states, diamagnetic insulators, and superconductors. *Phys. Rev. Lett.*, 61(23):2713–2716, 1988.

[144] P. W. Anderson. Model for the Electronic Structure of Amorphous Semiconductors. *Phys. Rev. Lett.*, 34(15):953–955, 1975.

[145] Mark R. De Guire, Norattam P. Bansal, David E. Farrell, Valerie Finan, Cheol J. Kim, Bethanie J. Hills, and Christopher J. Allen. The series $Bi_2Sr_2Ca_{n-1}Cu_nO_{2n+4}$ ($1 \leq n \leq 5$): Phase stability and superconducting properties. *Phys. C Supercond.*, 179(4-6):333–346, 1991.

[146] S. Nakajima, M. Kikuchi, Y. Syono, T. Oku, D. Shindo, K. Hiraga, N. Kobayashi, H. Iwasaki, and Y. Muto. Synthesis of bulk high Tc superconductors of $TlBa_2Ca_{n-1}Cu_nO_{2n+3}$ (n = 2 - 5). *Phys. C Supercond.*, 158(3):471–476, 1989.

[147] J. E. Hirsch and D. J. Scalapino. Double-valence-fluctuating molecules and superconductivity. *Phys. Rev. B*, 32(9):5639–5643, 1985.

[148] A. Taraphder and P. Coleman. Heavy-fermion behavior in a negative-U Anderson model. *Phys. Rev. Lett.*, 66(21):2814–2817, 1991.

[149] Y. Matsushita, H. Bluhm, T. H. Geballe, and I. R. Fisher. Evidence for charge Kondo effect in superconducting Tl-doped PbTe. *Phys. Rev. Lett.*, 94(15):1–4, 2005.

[150] P. Giraldo-Gallo, Hanoh Lee, Y. Zhang, M. J. Kramer, M. R. Beasley, T. H. Geballe, and I. R. Fisher. Field-tuned superconductor-insulator transition in $BaPb_{1-x}Bi_xO_3$. *Phys. Rev. B - Condens. Matter Mater. Phys.*, 85(17):1–7, 2012.

[151] Maxim Dzero and Jörg Schmalian. Superconductivity in charge Kondo systems. *Phys. Rev. Lett.*, 94(15):1–4, 2005.

[152] M. Matusiak, E. M. Tunnicliffe, J. R. Cooper, Y. Matsushita, and I. R. Fisher. Evidence for a charge Kondo effect in $Pb_{1-x}Tl_xTe$ from measurements of thermoelectric power. *Phys. Rev. B*, 80(22):220403, 2009.

[153] T. H. Geballe and S. A. Kivelson. Paired Insulators and High Temperature Superconductors. *ArXiv*, 2014.

[154] J. Blasco and J. Garcia. Structure, magnetic and electrical properties in $Nd_{1-x}La_xNiO_3$ system. *Solid State Ionics*, 63 - 65:593 – 598, 1993.

[155] J Blasco and J Garcia. A comparative study of the crystallographic, magnetic and electrical properties of the Nd_{1-x} $La_xNiO_{3-\delta}$ system. *J. Phys. Condens. Matter*, 6(49):10759–10772, 1994.

[156] Ashutosh Tiwari, K. P. Rajeev, and J. Narayan. Low temperature electrical transport in $La_{1-x}Nd_xNiO_{3-d}$. *Solid State Commun.*, 121:357–361, 2002.

[157] A. S. Disa, D. P. Kumah, J. H. Ngai, E. D. Specht, D. A. Arena, F. J. Walker, and C. H. Ahn. Phase diagram of compressively strained nickelate thin films. *APL Mater.*, 1(3), 2013.

[158] J. García, J. Blasco, M. G. Proietti, and M. Benfatto. Analysis of the x-ray-absorption near-edge-structure spectra of $La_{1-x}Nd_xNiO_3$ and $LaNi_{1-x}Fe_xO_3$ perovskites at the nickel K edge. *Phys. Rev. B*, 52(22):15823–15828, 1995.

[159] Daniele Preziosi, Anke Sander, Agnès Barthélémy, and Manuel Bibes. Reproducibility and off-stoichiometry issues in nickelate thin films grown by pulsed laser deposition. *AIP Adv.*, 7(1), 2017.

[160] M. A. Novojilov, O. Yu Gorbenko, I. E. Graboy, A. R. Kaul, H. W. Zandbergen, N. A. Babushkina, and L. M. Belova. Perovskite rare-earth nickelates in the thin-film epitaxial state. *Appl. Phys. Lett.*, 76(15):2041–2043, 2000.

[161] Jack Y. Zhang, Honggyu Kim, Evgeny Mikheev, Adam J. Hauser, and Susanne Stemmer. Key role of lattice symmetry in the metal-insulator transition of $NdNiO_3$ films. *Sci. Rep.*, 6(April):1–7, 2016.

[162] Bruno Berini, Niels Keller, Yves Dumont, Elena Popova, Wafaa Noun, Marcel Guyot, Jacky Vigneron, Arnaud Etcheberry, Nuno Franco, and Rui M. C. da Silva. Reversible phase transformation of $LaNiO_3$ thin films studied in situ by spectroscopic ellipsometry. *Phys. Rev. B*, 76(20):205417, 2007.

[163] Mahesh Chandra, Sarmistha Das, Fozia Aziz, Manoj Prajapat, and K. R. Mavani. Induced metal-insulator transition and temperature independent charge transport in $NdNiO_{3-\delta}$ thin films. *J. Alloys Compd.*, 696:423–427, 2017.

[164] A. R. Denton and N. W. Ashcroft. Vegard's law. *Phys. Rev. A*, 43(6):3161–3164, 1991.

[165] M. Zaghrioui, A. Bulou, P. Lacorre, and P. Laffez. Electron diffraction and Raman scattering evidence of a symmetry breaking at the metal-insulator transition of $NdNiO_3$. *Phys. Rev. B*, 64(8):081102, 2001.

[166] C. Girardot, J. Kreisel, S. Pignard, N. Caillault, and F. Weiss. Raman scattering investigation across the magnetic and metal-insulator transition in rare earth nickelate $RNiO_3$. *Phys. Rev. B*, 78(10):104101, 2008.

[167] H. J. Zhao and Jorge Íñiguez. To be published. *Priv. Commun.*, page 1, 2018.

[168] B. Noheda, D. E. Cox, G. Shirane, J. A. Gonzalo, L. E. Cross, S-E. Park, and . A monoclinic ferroelectric phase in the $Pb(Zr_{1-x}Ti_x)O_3$ solid solution. *Appl. Phys. Lett.*, 74(2059):72–75, 1999.

[169] Raoul Scherwitzl. *Metal-insulator transitions in nickelate heterostructures*. PhD thesis, University of Geneva, 2012.

[170] C H Ahn, J Triscone, and J Mannhart. Electric field effect in correlated oxide systems. *Nature*, 424:1015–1018, 2003.

[171] K. Ueno, S. Nakamura, H. Shimotani, A. Ohtomo, N. Kimura, T. Nojima, H. Aoki, Y. Iwasa, and M. Kawasaki. Electric-field-induced superconductivity in an insulator. *Nat. Mater.*, 7(11):855–858, 2008.